Loma Linda University

TheScholarsRepository@LLU: Digital Archive of Research, Scholarship & Creative Works

Loma Linda University Electronic Theses, Dissertations & Projects

9-1-2010

Quantification of Localized Brain Iron Sources Using Magnetic Resonance Phase

Grant Alexander McAuley
Loma Linda University

Follow this and additional works at: http://scholarsrepository.llu.edu/etd

Part of the Medical Physiology Commons

LOMA LINDA UNIVERSITY
School of Medicine
in conjunction with the
Faculty of Graduate Studies

———————————

Quantification of Localized Brain Iron Sources Using Magnetic Resonance Phase
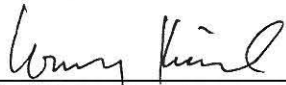
by

Grant Alexander McAuley

———————————

A Dissertation submitted in partial satisfaction of
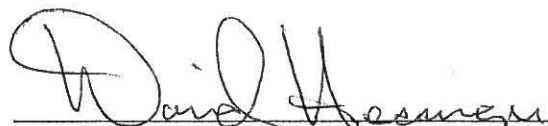the requirements for the degree of
Doctor of Philosophy in Physiology

———————————

September 2010

Each person whose signature appears below certifies that this dissertation in his/her opinion is adequate, in scope and quality, as a dissertation for the degree Doctor of Philosophy.

_____, Co-chairperson
Wolff Kirsch, Director of Center for Neurosurgery Research, Training and Education, Professor of Neurosurgery, and of Biochemistry
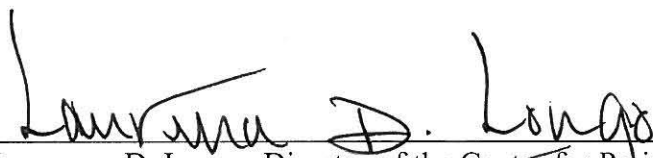
_____, Co-chairperson
David Hessinger, Professor of Physiology and Pharmacology

_____
Barbara Holshouser, Professor of Radiology

_____
Daniel Kido, Professor and Chair of Biophysics and Bioengineering, Professor and Head of Division of Neuroradiology

_____
Lawrence D. Longo, Director of the Center for Perinatal Biology, Distinguished Professor of Physiology, and of Gynecology & Obstetrics

_____
Gordon Power, Professor of Physiology, and Research Professor of Internal Medicine

_____
Pal Sipos, Associate Professor of Inorganic and Analytical Chemistry, University of Szeged

iii

ACKNOWLEDGEMENTS

I would like to thank and acknowledge:

… My Creator and Savior, to whom I am indebted for all things. In particular, for His grace to perform and complete the research presented here, and in general, for the privilege of existence in His wonderful universe and the hope of eternal life in the coming age through Jesus Christ. *Soli Deo Honor et Gloria.*

… Dr. Wolff Kirsch, for his mentorship, encouragement, and providing a supportive, stimulating and collaborative environment to learn and grow.

… Each committee member, Drs. Hessinger, Holshouser, Kido, Longo, Power and Sipos, for their unique contribution toward the completion of this Dissertation and my growth as a scientist.

… Dr. Andre Obenaus, for providing resources, support and advice.

… Matthew Schrag, for his help, enthusiasm, encouragement, advice, and friendship over the course of this research project.

… Sam Barnes for technical input in the areas of MRI, imaging processing, mathematics and data analysis.

… Cindy Dickson, Jackie Knecht, and April Dickson for their help, support, and encouragement throughout my association with the Neurosurgery Center for Research.

… Finally, my wonderful copilot and wife, Virginia, for her sacrifice, patience, prayers, encouragement, advice and good cooking over the course of this long journey.

Please Note: The text of Chapter 2 has been published in *Magnetic Resonance in Medicine* 2010 63(1) 106-115.

CONTENTS

vii

TABLES

FIGURES

ABBREVIATIONS

$A\beta$	Amyloid β peptide
AAS	Atomic absorption spectrometer
AD	Alzheimer's disease
ApoE e4	Apolipoprotein E4 allele
B_0	Main magnet magnetic field
ΔB	Change in local magnetic field
ΔB_z	Z-component of local magnetic field change
BMB	Brain microbleed(s)
BOMBS	Brain Observer MicroBleed Scale
CAA	Cerebral amyloid angiopathy
$CHCl_3$	Chloroform
Ch-Fe	Chitosan-iron composite material
Ch-Fe-Agr	Ch-Fe agarose mixture
CP	Caudate/Putamen
DWI	Diffusion weight imaging
FeOOH	Ferric-oxy-hydroxide
FLAIR	Fluid attenuated inversion recovery
FOV	Field of view
GRE	Gradient recalled echo
H_2O_2	Hydrogen peroxide
HD	Huntington's disease
HNO_3	Nitric acid

HP	High-pass filtered, or high-pass filtered images
HS	Hallervorden-Spatz disease
ICH	Intracerebral hemorrhage
MAT	Matrix
MCI	Mild cognitive impairment
MARS	Microbleed Anatomical Rating Scale
MR	Magnetic resonance
MS	Multiple Sclerosis
NEX	Number of excitations
PFA	Paraformaldehyde
PD	Parkinson's disease
POD	Post operative day
ROI	Region of interest
SEM	Standard error of the mean
SNR	Signal to noise ratio
SNR_{Mag}	Signal to noise ratio of magnitude image
SWI	Susceptibility weighted imaging
T_1	Spin-lattice relaxation constant
T_2	Spin-spin relaxation constant
T_2^*	Total transverse relaxation constant ($1/T_2^* = 1/T_2 + 1/T_2'$)
T_2'	Relaxation constant associated with static field inhomogeneity
TR	Repetition time
TE or T_E	Echo time

| U | Collagenase activity units |
| w/w | Weight by weight |

MATHEMATICAL SYMBOLS

$(m_{Fe})_{BMB}$	BMB iron mass
$(m_{Tissue})_{BMB}$	Mass of tissue block containing a BMB
$(\delta m_{Fe})_t$	Mass sensitivity due to finite slice thickness phase averaging
$(\delta m_{Fe})_\varphi$	Mass sensitivity due to white noise
$[Fe]_{BMB}$	Iron concentration of a tissue block containing a BMB
$[Fe]_{CONTROL}$	Iron concentration of a control tissue block
A	Ampere
a	Radius of sample
a	Semi-major axis of ellipsoid (Chapter 3)
a_0	Semi-axis of ellipsoidal iron sample
a_π	Point where the phase reaches the value of π along the direction of the major axis (the 'a' direction) of ellipsoid
a'_π	Point where the phase reaches the value of π along the 'a' minor axis of ellipsoid that coincides with the main magnetic field axis
a^*_π	Elliptical radius given by equation 20 of Chapter 3
$\hat{a}$	Direction vector of major axis of ellipsoid
b	Semi-minor axis of ellipsoid
b_0	Semi-axis of ellipsoidal iron sample
B_0	Main magnet magnetic field
b_π	Point where the phase reaches the value of π along the 'b' minor axis of ellipsoid
b^*_π	Point where the phase reaches the value of π along the 'b' minor axis of ellipsoid that coincides with the main magnetic field axis
c	Semi-minor axis of ellipsoid
c_0	Semi-axis of ellipsoidal iron sample
c_π	Point where the phase reaches the value of π along the 'c' minor axis of ellipsoid
d	Diameter of sample
d^*	Best estimate of sample diameter
d_{min}	Minimum diameter
e_x	Unit vector in the x direction

$f_{(Fe)I}$	w/w Fe concentration of ipsilateral tissue block
$f_{(Fe)C}$	w/w Fe concentration of contralateral tissue block
h	Focal length of ellipsoid in the x-y plane
h_π	Alias for c_π
i	Square root of -1
$I_{1,1}(x{:}\infty)$	Integral of equation 7 of Chapter 3 evaluated at x
$I_{1,2}(x{:}\infty)$	Integral of equation 8 of Chapter 3 evaluated at x
I	$I_{1,1}$ or $I_{1,2}$ depending on the context
k	Focal length of ellipsoid in the x-z plane
m	Mass
m^2	Meter squared
m_{Fe}	Mass of iron
$m_{(Fe)L}$	Mass of iron in lesion
m_I	Mass of ipsilateral tissue block
m_n	Mass of current sample
m_{n+1}	Mass of next sample
r	Distance from sample center
r_π	Point where the phase reaches the value of π
r'_π	Point where the phase reaches the value of π along vertical dipole axis
$r_{3\pi}$	Point where the phase reaches the value of 3π along horizontal dipole axis
$r_{5\pi}$	Point where the phase reaches the value of 5π along horizontal dipole axis
$r_{7\pi}$	Point where the phase reaches the value of 7π along horizontal dipole axis
$r_{n\pi}$	Point where the phase reaches the value of $n\pi$ along horizontal dipole axis
SNR_{Mag}	Signal to noise ratio of magnitude image
s	Pixel width
t	Slice thickness
T_E	Echo time
V	Volume of sample
v_π	a_π or b_π, depending on the context

α	Integration angle
α'	a'_π or $b*_\pi$, depending on the context
γ	Gyromagnetic ratio
ΔB	Change in local magnetic field
ΔB_z	z-component of local magnetic field change
Δm	Mass difference between successive samples
δm_{Fe}	Iron mass sensitivity
δr_π	Uncertainty in r_π
$\delta r'_\pi$	Uncertainty in r'_π
$\Delta\varphi$	Change in phase
$\delta\varphi$	Uncertainty in φ
$\Delta\varphi_D$	Phase change due to dipole
$\Delta\chi$	Change in susceptibility (ie, χ_i - χ_e)
$\zeta(x)$	Function of x given by equation 14 of Chapter 3
θ	Angle between main field and position vector
ρ	Density
$\bar{\varphi}$	Average phase
φ_0	Time independent phase constant
φ_L	Phase due Lorentz correction
φ_s	Background phase due to magnet or bulk geometry inhomogeneities
φ_T	Total phase of the voxel
χ_e	Magnetic susceptibility of medium surrounding sample (external susceptibility)
χ_i	Magnetic susceptibility of sample (internal susceptibility)

DISSERTATION ABSTRACT

Quantification of Localized Brain Iron Sources Using Magnetic Resonance Phase

by

Grant Alexander McAuley

Doctor of Philosophy, Graduate Program in Physiology
Loma Linda University, September 2010
Drs. Wolff Kirsch and David Hessinger, Co-chairpersons

Brain microbleeds (BMB), often present in cerebrovascular and

neurodegenerative diseases and neurotrauma, are associated with both chronic and acute

illness of significant social and economic impact. Because BMB present a source of

potentially cyctotoxic iron to the brain proportional to the amount of extravasated blood,

non-invasive quantification of this iron pool is potentially valuable both to assess tissue

risk and as a biomarker to monitor disease progression, treatment efficacy, and inform

treatment.

Past efforts to quantify brain iron have focused on distributed (e.g., anatomical)

brain regions. However, BMB represent localized sources of iron deposition. In

addition, conventional "magnitude" MR images have significant limitations, especially

for localized iron quantification. Moreover, due to susceptibility effects, the localized

hypointensities in gradient recalled T_2^* magnitude images associated with BMB typically

appear larger than the actual tissue lesion (the blooming effect) and obscure the true

dimensions of an iron susceptibility source. In the present research, we proposed a

family of techniques that use magnetic resonance phase images (instead of magnitude

images) to quantify the iron content and dimensions of localized iron sources such as

BMB.

The techniques were tested in four systems: 1) magnetic resonance agarose phantom and 2) postmortem rat brain, using a ferric iron oxy-hydroxide mimic for hemosiderin, 3) the living rat brain, using collagenase-induced bleeds, and 4) with actual BMB in postmortem cerebral amyloid angiopathy brain. Measurements of geometric features in phase images were related to source iron content and diameter using mathematical models. Iron samples and BMB lesions were assayed for iron content using atomic absorption spectrometry.

Results from experiments 1 and 3 in particular showed very good agreement with predictions of the theory underlying the techniques, providing validation for the methods and demonstrating that prominent phase image features can potentially be used to measure localized iron content including iron in real BMB. Our methods potentially allow the calculation of brain iron load indices based on BMB iron content as well as classification of BMB by size unobscured by the blooming effect. These results represent significant steps toward the use of similar localized iron quantification methods in experimental and clinical settings.

CHAPTER 1

INTRODUCTION

Brain Microbleeds

Brain microbleeds (BMB) are often present in cerebrovascular and

neurodegenerative diseases as well as neurotrauma and are increasing in clinical

importance (Cordonnier et al., 2007, Greenburg et al., 2009, Tong et al., 2003, Tong et

al., 2004). BMB are detected as focal signal losses in gradient recalled echo (GRE) T_2^*

magnetic resonance (MR) imaging and have been histopathologically related mainly to

hemosiderin (Fazekas et al., 1999, Tanaka et al., 1999, Schrag et al., 2010).

Hemosiderin, the iron-protein complex associated with pathologic iron storage following

hemorrhage (Bizzi et al., 1990) and ferritin breakdown (Schenk et al., 2004), is visible in

MR images due to it paramagnetic iron content and serves as a marker for BMB (Atlas et

al., 1988, Viswanathan and Chabriat 2006).

BMB in Cerebrovascular Disease

BMB have mostly been studied in the context of stroke medicine. Using data

extracted from a systematic review of 54 studies involving a total of 9,073 participants

(Cordonnier et al., 2007), BMB were reported present in 34% of study subjects with

ischemic stroke and 60% with non-traumatic intracerebral hemorrhage (ICH)

(Cordonnier et al., 2007). Based on two studies, the prevalence in stroke sub-types was

reported to be 54% among lacunar strokes, 36% among atherothrombotic strokes, and 19% among cardioembolic strokes. The association of microbleeding pathology (ie, BMB) with ischemic pathology was recently augmented by the following four studies: A serial case study found new silent lacunes in FLAIR (fluid attenuated inversion recovery) and DWI (diffusion weighted imaging) MR imaging two and 30 days following ICH in a subject with a classic neuroimaging picture of CAA (cerebral amyloid angiopathy) (Menon et al., 2009). Kimberly et al., reported 12/78 (15%) of CAA subjects had diffusion weighted imaging (DWI) hyperintense lesions consistent with subacute cerebral infarctions, significantly more than 0/55 subjects with Alzheimer's disease/mild cognitive impairment (Kimberly et al., 2009). The CAA subjects with DWI lesions had a higher median of number of BMB and total (micro plus macro) hemorrhages. The authors suggest that advanced CAA predisposes to ischemic infarction in addition to ICH (Kimberly et al., 2009). Igase et al., found BMB in 21.1% subjects with silent lacunar infarcts compared with BMB in 3.8% of subjects without silent lacunar infarcts (considered a predictor of stroke) (Igase et al., 2009). Jeon et al., reported new BMB seen after ischemic stroke in 13% of subjects (median 1, range: 1 – 5), and baseline BMB and small vessel disease predicted future BMB (Jeon et al., 2009). The Cordonnier review reports recurrent stroke patients had more BMB than those with first time stroke (Cordonnier et al., 2007), and in memory clinic subjects the presence of BMB was associated with the presence of lacunar infarcts in addition to large infarct and hemorrhages. These studies highlight that there is "cross talk" between "red and white" cerebrovascular disease (Kidwell and Greenburg 2009).

Alzheimer's Disease and Cerebral Amyloid Angiopathy

Late onset Alzheimer's disease (AD) is the most common form of dementia. Over 35 million people are affected worldwide including 5.5 million in the United States. The risk of developing AD increases with age doubling every five years after 65 with the odds of AD after 85 greater than one in three (Querfurth and LaFerla, 2010). Because of the aging population, the prevalence is projected to increase dramatically reaching to 13.2 million in the US by 2050 (Hebert et al., 2003). However, one hundred years after it was first described, the cause of AD is still unknown and effective treatments are not available. Conventional thinking implicates the amyloid β peptide (Aβ) as central to the disease process (Hardy and Higgins, 1992). However, Aβ plaques are not specific to AD (Bennett et al., 2006), and a cerebral vascular component to the disease is increasingly being recognized (Zlokovic, 2005, Dickstein et al., 2010). Finally, redox-active iron has a toxic effect on brain cells, and oxidative damage, iron accumulation and changes in iron metabolism are suspect in AD (Smith et al., 1997, Smith et al., 2010).

CAA is a cerebrovascular disease where Aβ is deposited in the media and adventitia of small cerebral arteries. It is characterized by lobar hemorrhages including BMB, subcortical white matter lesions, and cognitive impairment. It is believed that this deposition weakens the vessel wall and/or reduces vessel reactivity leading to the predisposition for micro and macro hemorrhages (Zhang-Nunes et al., 2006, Smith and Greenberg, 2009). CAA is present in up to ~95% of AD cases (Jellinger et al., 2007). Thus, CAA presents a condition where Aβ, vascular compromise and pathologic iron deposition (e.g., following BMB) are juxtaposed in the context of late onset dementia including AD.

BMB and Cognitive Decline

Recently in our prospective study we have observed that a subset of subjects with progressing dementia show brain microbleeds in iron-sensitive susceptibility weighted magnetic resonance images (SWI) (Kirsch et al., 2010). The spatial pattern of the BMB is reminiscent of CAA (Rosand et al., 2005, Kirsch et al., 2010). This raises the question whether cytotoxic and inflammatory sequelae following cerebral amyloid vasculopathy, BMB, and extravasated iron contribute significantly to the dementia in AD and CAA, and whether iron can be used as a biomarker in this context (see below).

While many BMB studies have focused on CAA, which is associated with late onset dementia, several studies have looked at cognitive decline in particular. Prevalence in AD has been reported to be 26.8% (Cordonnier et al., 2007) based on two studies which showed 32% (Hanyu et al., 2003) and 18% (Nakata et al., 2002) respectively. In memory clinic subjects BMB were found in 10% of those with subjective complaints, 20% with mild cognitive impairment (MCI), 18% of AD, and 65% with vascular dementia. The number of BMB was an independent predictor of cognitive impairments in attention, verbal memory, visual memory, language (marginally significant: p=0.061), visuospatial function, and frontal executive function, and also of dementia severity assessed by Mini Mental State Examination and Clinical Dementia Rating (marginally significant: p=0.052), in subjects with subcortical vascular dementia (Seo et al., 2007). BMB presence and number is associated with poorer performance on standard tests of global cognitive function (Yakushihi 2008), and there is a significant risk of converting from MCI status to dementia with 2 or more BMB at baseline (Kirsch et al., 2010).

Risk Factors

BMB prevalence was shown in the Rotterdam Scan Study to increase with age (Vernooij et al., 2008) and though the Cordonnier systematic review could not report pooled results, the authors do mention that several individual studies showed an increased prevalence with age (Cordonnier et al., 2007). The presence of BMB predicts new BMB (Gregoire et al., 2009, Jeon et al., 2009). In healthy adults, BMB were associated with hypertension and diabetes; in adults with cerebrovascular disease, BMB are associated with hypertension (Cordonnier et al., 2007).

CAA and Hypertension

BMB are considered to appear in spatial distributions associated with distinct etiologies: deep brain BMB are associated with hypertensive vasculopathy, whereas lobar BMB are associated with CAA (Greenberg et al., 2009, Vernooij et al., 2008, Knudsen et al., 2001, Fazekas et al., 1999, Vinters & Gilbert 1983). Deep, but not lobar, BMB have been reported to be associated with ambulatory blood pressure in first-ever lacunar stroke patients (Stalls et al., 2009). ApoE e4 (which is related to CAA and a known risk factor for AD) was reported to be associated with lobar, but not deep BMB (Vernooij et al., 2008). In another study, BMB were most frequently lobar with a predominant posterior location mostly in the parietal lobe, and homozygous ApoE e4 was associated with BMB. This, together with a borderline significance for hypertension, suggests an underlying CAA pathology in the study participants (Sveinbjornsdottir et al., 2008).

BMB and Future Bleeding Risk

Studies have shown that BMB in ischemic stroke, ICH and CAA patients are associated with future hemorrhage (Soo et al., 2008, Jeon et al., 2007, Greenberg et al., 2004, Greenberg et al., 2009). Whether BMB presence and number is associated with increased risk in first ever stroke has not yet been determined (Cordonnier et al., 2007, Greenberg et al., 2009). There appears to be controversy about whether BMB represent a risk for bleeding follow thrombolytic agents administered after stroke (Greenberg et al., 2009). BMB risk in the context of anticoagulant agents also is an open question (Greenberg et al., 2009). A recent cross sectional study found BMB were more prevalent in subjects that were using or had used platelet aggregation inhibitors drugs. In addition, aspirin users had lobar bleeds more often then carbasalate calcium users (Vernooji et al., 2009). Soo et al., conclude that benefits outweigh anticoagulant agent risk except perhaps when patients have 5 or more BMB (Soo et al., 2008).

BMB in 'Healthy' Populations

BMB have been reported present in 5% of healthy adult study subjects based on a systematic review of four studies where 70 of 1,411 had one or more BMB (Cordonnier et al., 2007). However, in each of these studies there was a high prevalence of hypertension among participants: 24.9% (Tsushima et al., 2002), 28.8% (Jeerakathil et al., 2004), 31.8% (Roob et al., 1999b) and 46.4% (Horita et al., 2003), so prevalence in non-hypertensive subjects is likely lower. In community-dwelling elderly Vernooij et al., found prevalence increased strongly with age (60-69 yrs: 17.8%, 70-79 yrs: 31.3%, 80-97: 38.3%) as did those with multiple BMB (60-69 yrs: 5.4%, 70-79 yrs: 16.5%, 80-97:

23.3%) (Vernooij et al., 2008). The higher prevalence here compared to the four studies just mentioned could be explained by the high mean age of participants (69.6 yrs) (Vernooij et al., 2008), and perhaps slightly because of magnet strength (Cordonnier et al., 2007). However, in another community study a lower prevalence of 11.1% was found and prevalence increased with age even though participants were older (mean age 76 yrs) (Sveinbjornsdottir et al., 2008).

Iron Content in BMB: A Biomarker

In light of the above discussion, it is clear that BMB are associated with cerebrovascular disease and AD – "the most common age-related pathologies of the brain" (Schneider 2007) as well as some of the most costly. Pathological studies have indicated tissue damage is associated with BMB (Fazekas et al., 1999, Tanaka et al., 1999, Schrag el al 2010). Unregulated or dysregulated brain iron can be cytotoxic (eg, free radical production through the Fenton reaction), and oxidative damage, iron accumulation and/or iron dysregulation have been implicated in neurodegenerative and cerebrovascular diseases (Vymazal et al., 2007, Gaasch et al., 2007, Andersen, 2004, Neema et al., 2009, Smith et al., 1997, Smith et al., 2010). Therefore, extravasated iron following BMB is potentially important for two reasons: 1) the iron is an agent of tissue damage and resulting disease, and 2) the amount of iron is proportional to the amount of extravasated blood and iron is therefore an indicator of the extent of microvascular fragility and disease. Thus, the quantified iron content in BMB is potentially a valuable biomarker to monitor disease progression, treatment efficacy and risk factor control. Finally, it is noteworthy that all the studies in BMB literature only count BMB and the

notion of severity is simply related to the number of BMB. Knowledge of the total iron deposited in each BMB would allow a more precise measure of severity. For example, two BMB containing 5 μg each represents more bleeding than 10 BMB containing less than 1 μg each. Such information may be useful in decisions regarding the use of antithrombotic or thrombolytic agents.

Brain Iron Quantification Using Magnetic Resonance

Magnitude and Phase Contrast in MRI

Black and white images (of any kind) are possible because the elemental units of the picture (e.g., pixels) vary in intensity. It is this contrast that allows the viewer to distinguish between objects and features of the image. In MR imaging, nuclear spins in tissues and molecules exchange energy with nuclear and electron spins in neighboring molecules and their microenvironment. In conventional MR, it is the differential rates at which this energy exchange takes place that gives rise to image contrast. These rates are quantified by three relaxation time constants T_1, T_2 and T_2^* ($1/T_2^* = 1/T_2 + 1/T_2'$ where T_2' is related to interactions between nuclear spins and static local magnetic field inhomogeneities). It is spatial differences in these rates that ultimately lead to contrast in image intensity or *magnitude*. Phase contrast on the other hand arises from a different mechanism. Due to their intrinsic angular momentum, nuclear spins in a strong magnetic field precess about the field with an angular velocity proportional to the field strength. Thus, in a given time a population of spins will trace out an angle proportional to the magnetic field in their microenvironment. Differences in this angle or *phase* reflect differences in local tissue properties and provide image contrast (Roberts and Mikulis

8

2007, Haacke et al., 1999). Phase information can be used in two ways: 1) in conjunction with magnitude images to enhance (magnitude) contrast, or 2) as a stand-alone contrast agent (Reichenbach et al., 1997a, Haacke et al., 2004).

Iron Quantification in Phase vs. Magnitude Images

There continues to be an interest in brain iron quantification (Brittenham et al., 2003, Schenck et al., 2004, Haacke et al., 2005, Jara et al., 2006). Because of the association with iron accumulation in normal aging and AD, Parkinson's (PD), Huntington's (HD), Multiple Sclerosis (MS), and Hallervorden-Spatz (HS) disease states several authors have recently attempted to determination brain iron content using magnitude contrast (Haacke et al., 2005, Jara et al., 2006, Bartzokis et al., 2007, Péran et al., 2009, Gilissen et al., 1999, Bartzokis et al., 1993, , Schenck et al., 2006, House et al., 2007, Ordidge et al., 1994, Gelman et al., 1999, Vymazal et al., 2007, Neema et al., 2009, McNeill et al., 2008). In particular, because the presence of paramagnetic iron leads to local changes in magnetic susceptibility and spin dephasing, these studies used T_2 relaxation times (or increased relaxation rate $R_2 = 1/T_2$), GRE T_2*, T_1/T_2 ratio, or T_2' methods. However, a fundamental weakness of these conventional magnitude image methods is their dependence on complex relaxation mechanisms (eg, spin-spin coupling) that possibly vary across tissue types, disease states, and experimental parameters (Gossuin et al., 2007; Jensen et al., 2009). MR phase however, is directly proportional to the susceptibility variations (eg, due to paramagnetic brain iron) and does not depend on a particular coupling mechanism. Tissue phase differences are theoretically independent of T_1 and T_2 tissue parameters and RF phase (Haacke et al., 2005). Thus, phase images

are expected to be largely free from the influence of confounding tissue water and more consistent across tissue types and states than T_1, T_2, T_2^* and T_2' approaches. In addition, unlike magnitude images that suffer signal loss when diffusion effects are significant (ie, outside the static dephasing regime (Yablonskiy and Haacke, 1994), bulk phase shifts due to internal or external time independent field inhomogeneities are thought to be largely unchanged by water diffusion.

The Blooming Effect in GRE T_2^* Magnitude Images

Moreover, the spatial extent of signal hypointensities in GRE T_2^* magnitude images of a localized source of magnetic susceptibility is typically larger than its actual size. This so called *blooming effect* varies with scan parameters as well as source magnetization (Bos et al., 2003; Pintaske et al., 2006b). Because the true dimensions of the source cannot be reliably determined, GRE T_2^* magnitude image signal void volume is unreliable for iron content determination (Dixon et al., 2009). The blooming effect is useful for at least two reasons: 1) it allows the visualization of tissue features that would otherwise be too small to see in MR images (eg, small vessels, magnetically labeled cells) (Reichenbach et al., 1997a), and 2) it is recommended criterion in BMB identification (Greenberg et al., 2009). However, since the blooming effect obscures the true dimensions of e.g. a BMB, MR magnitude images are not reliable for BMB size determination or for localizing the source of a signal void (e.g., magnetically labeled cells). In a recent report BMB appeared an average of 1.57 times larger than the actual tissue lesion in postmortem AD/CAA brain (Schrag et al., 2010), and in magnetically labeled cells blooming magnification is reported to be as much as 50 times (Dodd et al.,

1999). In part because of the blooming effect, the use of BMB (apparent) size has been discouraged in BMB identification. However, introduction of a technique to accurately estimate true source diameter would allow size criteria in classification of BMB and more precise spatial location. In addition, size determination together with iron content information would allow the estimation of iron concentration for BMB or magnetically labeled cell clusters.

Susceptibility Weighted Imaging

Susceptibility weighted imaging (SWI) is a GRE sequence that uses magnetic susceptibility-dependent complex phase information to provide or enhance image contrast (Haacke et al., 2004; Reichenbach et al., 1997a). Recent studies have shown SWI to be 3 to 6 times more sensitive in BMB detection than conventional GRE T_2^* methods (Akter et al., 2007; Tong et al., 2003). Theoretical considerations estimate SWI phase to be roughly 8 times more sensitive to iron content than conventional T_2 methods (Haacke et al., 2007).

Phase Image Studies

Several recent studies used phase images to investigate iron levels in normal subjects and AD, PD, and MS disease states (Ogg et al., 1999, Haacke et al., 2007, Xu et al., 2008, Ding et al., 2009, Kirsch et al., 2010, Zhang et al., 2009, Grabner et al., 2010, Ge et al., 2007), and several studies used both phase and magnitude methods in normal, MS, HSS subjects (Pfefferbaum et al., 2009, Hammond et al., 2008, Haacke et al., 2009, Eissa et al., 2009, Szumowski et al., 2010). Outside of the brain, phase approaches were

used to quantify iron oxide mass in localized injections of rat leg muscle (three injections in two postmortem rat legs) (Dixon et al., 2009) and magnetic moment in cylindrical phantoms (Robson and Hall, 2005). Dipole phase fitting approaches (Dixon et al., 2009) and the r_π parameter (very important in the present study) (Robson and Hall, 2005) are important and useful contributions of these papers. However, these studies showed limited success, inconsistent results, as well as several important limitations including questionable adequacy of background phase removal, and/or not accounting for source geometry. Finally, Cheng et al., proposed a phase method using an infinite cylinder model (Cheng et al., 2007) that could potentially be adapted to more localized (eg, spherical) sources like BMB.

Limitations of Phase Images

While possessing several advantages over magnitude images for iron quantification (Haacke et al., 2005, McAuley et al., 2010a) phase image approaches also face limitations. Phase contrast depends on source geometry and orientation with respect to the main magnetic field. In addition, because field perturbations extend beyond the sources of susceptibility that cause the perturbations, the phase is also altered in areas surrounding the source (Shmueli et al., 2009, Schäfer et al., 2009). The effects ultimately arise from the fundamental physical nature of the magnetic field (e.g., solenoidality) and these effects of orientation-dependent contrast and non-locality cannot be fully eliminated in phase images. However, for localized iron sources these effects are less important and can even be exploited in localize iron content determination (discussed in Chapters 4 and 6).

Localized Versus Distributed Iron Sources

It is noteworthy that to date, efforts to determine brain iron content have primarily involved brain regions (eg, anatomic structures). However, BMB represent a localized source of iron where quantification is desirable. The studies of Robson and Hall (Robson and Hall, 2005), Dixon et al., (Dixon et al., 2009), and Cheng et al., (Cheng et al., 2007) mentioned above, are examples where localized sources of susceptibility were studied using a phase image approach.

Purpose of the Present Research

From the above discussion, it is clear that BMB are associated with diseases of aging that have enormous social and economic impact. BMB represent a source of pathologic iron to the brain that is potentially informative whether iron is found to be a significant agent of disease or a surrogate biomarker of cerebral vessel pathology. BMB iron quantification could provide diagnostic or prognostic information as well as guidelines for treatment. Knowledge of the amount of iron in individual bleeds would allow the definition of an *iron load index* for a group of bleeds. For example, one could sum up all the extravasated iron due to all lobar bleeds and define a *lobar iron load index*. Such constructs could provide more sensitive information than mere counts of eg lobar BMB. In experimental systems, localized bleeding lesions could similarly be characterized, compared and monitored. Localized quantification techniques also have potential applications beyond the BMB context - for example, in the non-invasive tracking, location and quantification of magnetically labeled cell clusters (eg, stem and immune system cells). Finally, an automated or semi-automated system to analyze

images containing localized iron sources would greatly increase the usefulness of a quantification technique.

The purpose of this research project was to investigate and develop techniques to quantify the iron content and size of localized brain iron sources using magnetic resonance phase images. Easily recognized phase image parameters[1] were mathematically related to source iron content and dimensions. Experimental results were compared with these theoretical predictions and thus provided validation for the proposed methods.

The techniques were developed and tested in four major experiments. The first two experiments introduce and validate the basic methods in idealized model systems. The last two experiments apply and test the methods to postmortem human and living animal tissue. Thus, the four experiments present a body of work that follows a logical progression of investigation and application of the techniques from the more idealized model toward localized iron content quantification in systems more relevant to clinical and experimental settings.

Experiment 1: Phantom System

Experiment one can be thought of as a 'proof of concept' experiment. Samples from a polysaccharide/ferric oxy-hydroxide composite material (Ch-Fe) (Sipos et al., 2003) were embedded in agarose and scanned with an SWI MR protocol at 11.7T. Localized samples were mathematically modeled as magnetic dipoles. The phase image analysis method that relates features in the images with the underlying theory depends on

---

[1] The phrase "phase image parameters" (or a similar phrase) in this document refers to measurements of characteristic features of patterns in phase images due to the presence of localized iron sources. This should not be confused with the "imaging parameters" that are chosen and used to acquire MR images.

measurement of the r_π parameter. This phase parameter was described in the literature by Robson and Hall in an attempt of limited success to measure the magnetic moment of cylindrical phantoms containing solutions of manganese chloride (Robson and Hall, 2005). In this present experiment we apply a very similar r_π method to our spherical iron samples. However, we employ high-pass filtering (Wang et al., 2000, Haacke et al., 2004) of higher resolution phase images, and report very good success. In addition, we discuss and test the prediction (suggested by Robson and Hall, 2005) that phase images and the r_π parameter can in principle be used to determine the true diameter (i.e., unobscured by the blooming effect) of a localized susceptibility source (a spherical source of iron in our case), and consider questions of iron measurement sensitivity. Chapter two is entitled "Quantification of Punctate Iron Sources Using Magnetic Resonance Phase" and presents experiment one in the form of a paper recently published in *Magnetic Resonance in Medicine* with the same title (McAuley et al., 2010a).

Experiment 2: Postmortem Rat Brain Chitosan/Iron Injection

While experiment one involved iron samples assumed and carefully prepared to be spherical, experiment two investigated quantification of non-spherical sources. In addition, quantification was investigated in the real tissue of the rat brain. Ch-Fe was injected in perfused postmortem rat brains that were then scanned with an SWI protocol at 11.7T. Ch-Fe samples were modeled as scalene (triaxial) ellipsoids using ellipsoidal coordinates. Generalizations and analogs of r_π are introduced and putatively related with the dipole-like phase images patterns associated with the Ch-Fe samples. Computer simulations were also performed as to check the validity of the method. Chapter three is

entitled "Quantification of Ellipsoidal Iron Sources in Postmortem Rat Brain Using Phase Images" and presents this experiment as a work in progress.

Experiment 3: BMB Quantification in Postmortem Human CAA Brain

In this experiment a modified spherical method was applied to real BMB in postmortem tissue of AD/CAA patients. Tissue slices containing BMB were imaged using an SWI protocol at 11.7T. BMB lesions were then assayed for iron content using atomic absorption spectrometry. We present a standardization curve where BMB iron content can tentatively be related to phase image parameters at least in tissue similar to our autopsy cases. In addition, we introduce a second method to estimate BMB source diameter based on image feature geometry alone (without explicit relation to the magnetic susceptibility of the source). Finally, we report iron mass estimates, as well as upper bound diameter and lower bound iron concentration estimates of the postmortem BMB. Chapter four is entitled "Iron Quantification of Microbleeds in Postmortem Brain" and presents this experiment in the form of a paper of the same title recently accepted for publication pending minor revisions in *Magnetic Resonance in Medicine* (revisions not included).

Experiment 4: Collagenase Induced BMB in Living Rat Brain

In experiment four we induce small hemorrhagic lesions in the living rat brain. In a simple but novel in vivo rodent BMB model, bleeds were induced by collagenase injection. Approximately a month after the surgical procedure, we scanned the animals before sacrifice at 4.7T using an SWI protocol, and assayed lesion iron content following

sacrifice using atomic absorption spectrometry. We used our modified spherical method to relate lesion iron content and phase image measurements, and tested the expected relationship using liner regression. While not as robust as in previous experiments, the results of this experiment demonstrate that a localized phase image model can potentially be used to estimate localized iron content in the living rodent brain. Chapter five is entitled "In Vivo Iron Quantification in Collagenase-Induced Microbleeds in Rat Brain" and presents this experiment as a manuscript in preparation to submit for publication.

Finally, chapter six discusses the results, implications, limitations, and areas for future work of the four experiments, individually and collectively.

CHAPTER TWO

QUANTIFICATION OF PUNCTATE IRON SOURCES USING

MAGNETIC RESONANCE PHASE

Grant McAuley[1], Matthew Schrag[1], Pál Sipos[2], Shu-Wei Sun[3], Andre Obenaus[3,4,5], Jaladhar Neelavalli[6,7], E. Mark Haacke[5,6,8], Barbara Holshouser[5], Ramóna Madácsi[2] and Wolff Kirsch[1,*]

Neurosurgery Center for Research, Training and Education[1], Biophysics and Bioengineering, School of Science and Technology[3], Non-Invasive Imaging Laboratory, Radiobiology Program[4], Loma Linda University, Loma Linda, CA, USA

Department of Inorganic and Analytical Chemisty[2], University of Szeged, Hungary

Radiology[5], Loma Linda University Medical Center, Loma Linda, CA, USA

The Magnetic Resonance Imaging Institute for Biomedical Research[6], Detroit, Michigan, USA

ONNRU, Nuffield Department of Surgery[7], University of Oxford, UK

Department of Radiology[8], Wayne State University, Detroit, MI, USA

*Send correspondence to:
Wolff M. Kirsch
Neurosurgery Center for Research, Training and Education
Loma Linda University,
11175 Campus Street, CPA11113
Loma Linda, CA, 92354
E-mail: wkirsch@llu.edu
Tel: 909-558-7070
Fax: 909-558-0472

Abstract

Iron-mediated tissue damage is present in cerebrovascular and neurodegenerative diseases and neurotrauma. Brain microbleeds (BMB) are often present in these maladies and are assuming increasing clinical importance. Because BMB present a source of pathologic iron to the brain, the non-invasive quantification of this iron pool is potentially valuable. Past efforts to quantify brain iron have focused on content estimation within distributed brain regions. In addition, conventional approaches using 'magnitude' images have met significant limitations. In this study, a technique is presented to quantify the iron content of punctate samples using phase images. Samples are modeled as magnetic dipoles and phase shifts due to local dipole field perturbations are mathematically related to sample iron content and radius using easily recognized geometric features in phase images. Phantoms containing samples of a chitosan-ferric oxyhydroxide composite (which serves as a mimic for hemosiderin) were scanned with a susceptibility weighted imaging sequence at 11.7T. Plots relating sample iron content and radius to phase image features were compared to theoretical predictions. The primary result is the validation of the technique by the excellent agreement between theory and the iron content plot. This research is a potential first step toward quantification of punctate brain iron sources such as BMB.

Keywords

Iron quantification, phase images, susceptibility weighted imaging, brain microbleeds

Introduction

Brain microbleeds (BMB), detected as focal signal losses in gradient recalled echo (GRE) T_2^* MRI, are assuming an increasing clinical importance (Greenberg et al., 2009; Cordonnier et al., 2007; Nighoghossian et al., 2002; Tong et al., 2003; Tong et al., 2004; Scheid et al., 2003; Yakushiji et al., 2008). Hemosiderin, the iron-protein complex associated with pathological iron storage following hemorrhage (Bizzi et al., 1990), is visible in MR images due to its paramagnetic iron content and serves as a marker for BMB (Atlas et al., 1988; Viswanathan and Chabriat, 2006). BMB represent a potentially significant and previously underestimated source of pathologic brain iron, and iron-mediated tissue damage is implicated in neurotrauma, cerebral vascular disease and a variety of neurodegenerative maladies (Andersen, 2004; Bush, 2003; Gaasch et al., 2007; Neema et al., 2009; Vymazal et al., 2007). Therefore, non-invasive MR quantification of iron is potentially valuable both as a marker of disease progression and for monitoring treatment efficacy (Haacke et al., 2005; Schenck and Zimmerman, 2004).

Susceptibility weighted imaging (SWI) is a GRE sequence that uses magnetic susceptibility-dependent complex phase information to provide or enhance image contrast (Haacke et al., 2004; Reichenbach et al., 1997a). Recent studies have shown SWI to be 3 to 6 times more sensitive in BMB detection than conventional GRE T_2^* methods (Akter et al., 2007; Tong et al., 2003). Theoretical considerations estimate SWI phase to be roughly 8 times more sensitive to iron content than conventional T_2 methods (Haacke et al., 2007). In addition, compared to conventional magnitude techniques, high-field (7.0T) high resolution GRE phase images have shown a nearly 10 fold increase in gray/white matter contrast to noise ratio and dramatic contrast heterogeneity attributed at

least in part to tissue iron stores (Duyn et al., 2007). Previous attempts to relate phase differences to brain iron content compared average phase values with published iron concentrations of brain regions (Ogg et al., 1999), or determined baseline phase values of iron-rich brain regions (Haacke et al., 2007).

It is noteworthy that to date, efforts to determine brain iron content have primarily involved brain *regions* (eg, anatomical structures) rather than punctate iron deposits (eg, BMB). In addition, the spatial extent of signal hypointensities in GRE images of a punctate susceptibility source is typically larger than its actual size and varies with scan parameters as well as source magnetization (Bos et al., 2003; Pintaske et al., 2006b). Because the true dimensions of the source cannot be reliably determined using signal size as a criterion in BMB quantification has been called in question (Greenberg et al., 2009), and as expected, GRE signal void volume is unreliable for iron content determination (Dixon et al., 2009).

The purpose of this study was to investigate iron quantification of punctate iron sources using a phase technique. Iron-containing samples were modeled as magnetic dipoles. The easily recognizable image parameter r_π (the distance from the dipole center associated with a phase value equal to π (see below)) (Robson and Hall, 2005) was hypothesized to be mathematically related to iron content and sample radius. The technique was validated using phantoms constructed with a chitosan-ferric oxyhydroxide composite (a mimic for hemosiderin) (Sipos et al., 2003). In this paper, phase images of the phantom samples were acquired using a SWI sequence at 11.7T. Plots relating sample iron content and actual diameter with the r_π parameter were compared to theoretical predictions using linear regression analysis to test the hypothesis.

Materials and Methods

Theoretical Background and Rationale

MR voxels containing and surrounding paramagnetic (or ferromagnetic) brain iron deposits have an altered local field ΔB, and thus an altered phase with respect to their neighbors. This phase difference is detectible in GRE pulse sequences and described by the simple formula (for a right handed system):

$$\Delta\phi = -\gamma\,\Delta B\,T_E$$

[1]

where $\Delta\varphi$ is the change in phase, γ is the proton gyromagnetic ratio, and T_E is the echo time (Haacke et al., 1999). Thus, the amount of iron in a voxel can potentially be related to the phase. If iron samples are treated as spherical magnetic dipoles under the assumptions that the magnetic susceptibility (χ_i) is constant throughout the sample, and the sample is immersed in a medium with a constant magnetic susceptibility (χ_e), the only non-negligible component of ΔB is parallel to the main field B_0 and for $r > a$ given by:

$$\Delta B_z = \left[\left(\frac{\Delta\chi}{3}\right)\left(\frac{a}{r}\right)^3 (3\cos^2\theta - 1) + \frac{\chi_e}{3}\right] B_o \qquad (r > a)$$

[2]

Here $\Delta\chi \equiv (\chi_i - \chi_e) \ll 1$, a is the radius of the sample, θ the angle with respect to the main field axis, r is the distance from the center of the sample to the point of interest P (Fig 2.1A), and $\chi_e/3$ is the Lorentz sphere correction (Haacke et al., 1999). Further, if constant density ρ is assumed, the mass m of the sample can be expressed as:

$$m = \left(\frac{4\pi\rho}{3}\right)a^3$$

[3]
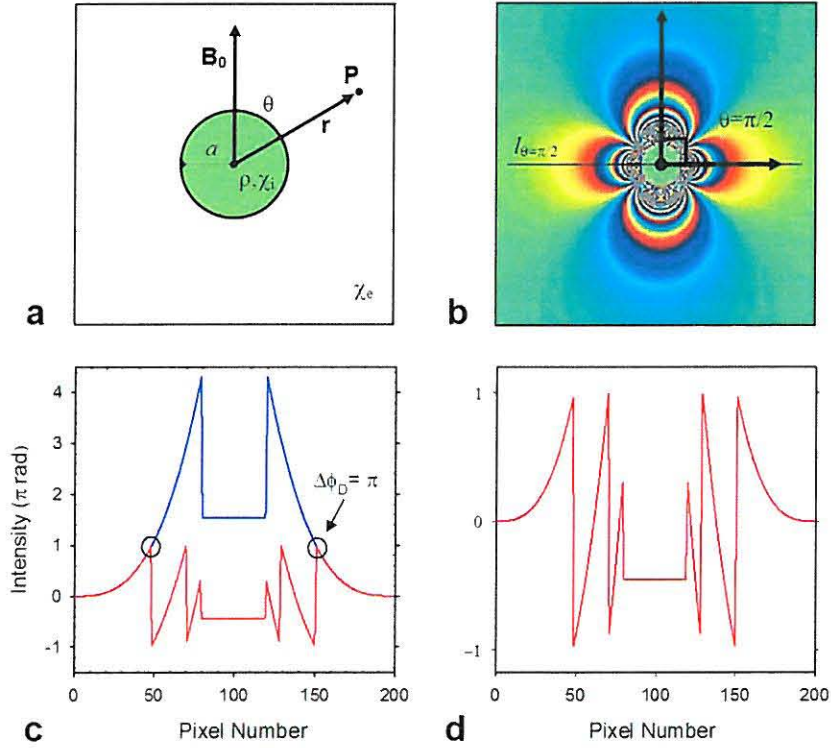
Figure 2.1: Iron-Containing Samples are Treated as Magnetic Dipoles. A) Cross-sectional schematic of a sample with radius a, density ρ, and magnetic susceptibility χ_i, embedded in a medium with susceptibility χ_e, and immersed in a magnetic field B_0. The azimuthally symmetric induced field (Eq. [2]) as well as the proportional phase (Eq. [1]) vary at point P with r and θ. B) A simulated modulo-2π wrapped phase map of a slice containing the main-field axis. Red and blue bands represent phase values of π (maximum) and $-\pi$ (minimum) respectively and thus the red-blue interfaces define 'phase wrappings'. A line through the center of the sample perpendicular to the main field axis (ie, $\theta = \pi/2$) is shown and labeled $l_{\theta = \pi/2}$. C) *Blue trace*: a simulated phase profile along $l_{\theta = \pi/2}$. *Red trace*: a modulo-2π phase wrapped profile. The circles highlight the coordinates where the traces intersect with a maximum phase value $\Delta\varphi_D = \pi$ (arrow). These points corresponds with the outermost red-blue interface along line $l_{\theta=\pi/2}$ of B and define r_π. D) Red trace of C is plotted alone. Lateral maximal peaks represent $\Delta\varphi_D = \pi$ for $r = r_\pi$, medial maximal peaks define $\Delta\varphi_D = 3\pi$ for $r = 3^{1/3} r_\pi$. B, C and D were generated from in-house MATLAB code (The MathWorks, Natick, MA).

Finally, for $\theta = \pi/2$ and assuming for the moment $\chi_e = 0$, Eqs. [1], [2] and [3] imply that at a distance $r > a$ from the dipole center along a line perpendicular ($l_{\theta=\pi/2}$) to its axis (Fig 2.1A & B), the phase change due to the dipole sample $\Delta\varphi_D$ can be related to the mass of the sample m_{Fe} by the following formula:

$$m_{F_e} = \left[\left(\frac{4\pi\rho}{\Delta\chi} \right) \left(\frac{\Delta\phi_D}{\gamma' B_o T_E} \right) \right] r^3 \qquad (r > a, \chi_e = 0)$$

[4]

A simulated phase profile along $l_{\theta=\pi/2}$ of a sample is shown in Fig 2.1C (blue line) for a paramagnetic source ($\Delta\chi > 0$). MR imaging systems typically display phase maps modulo 2π over the interval $(-\pi, \pi]$ as shown in Fig 2.1C (red line). A key observation (as seen in the figure) is that the maximum phase value where the two plots overlap is equal to π. If we let r_π (Robson and Hall, 2005) denote the value on the abscissa corresponding to $\Delta\varphi_D = \pi$, then Eq. [4] becomes:

$$m_{F_e} = \left(\frac{4\pi^2\rho}{\gamma' \Delta\chi B_o T_E} \right) r_\pi^3 \qquad (\Delta\chi > 0)$$

[5]

For given B_0 and T_E values, Eq. [5] reveals a strictly proportional relationship between the mass of iron and the cube of r_π. The r_π parameter is easily identified in modulo 2π phase maps and their intensity profiles. Thus, Eq. [5] implies that such phase maps could be used to quantify the iron content of punctate iron samples treated as magnetic dipoles.

Eq. [5] is however, an idealized case that involves changes in phase due only to the magnetic dipole source. A more complete description of the total phase of a voxel is given by:

$$\varphi_T = \varphi_0 + \varphi_s + \varphi_L + \Delta\varphi_D, \tag{6}$$

where φ_T is the total phase of the voxel, φ_0 is a time independent constant possibly due to the conductivity and permittivity of the voxel (Haacke et al., 1999) or scanner central frequency shift, φ_s is a background phase due to magnet or bulk geometry inhomogeneities, φ_L is the Lorentz correction necessary when $\chi_e \neq 0$ (Haacke et al., 1999) and $\Delta\varphi_D$ is the dipole phase change of interest. Therefore, in a real-world phase map, r_π is associated with $\varphi_T = \pi$ and Eq. [4] implies π must be replaced by $\pi - (\varphi_0 + \varphi_s + \varphi_L)$ in Eq. (5). Since $\varphi_0 + \varphi_s + \varphi_L$ is generally unknown (at least *a priori*) and varies with scanner, this substitution seems to spoil the promise of the quantification technique. However, phase contributions that are constant or vary over spatial scales that are long compared to local dipole field variations (e.g., magnet inhomogeneities) can potentially be removed from the phase map by homodyne high-pass filtering (Wang et al., 2000). Therefore, under the assumption of complete background removal (ie, $\varphi_T = \Delta\varphi_D$), Eq. [5] can be applied to high-pass filtered modulo 2π phase maps of dipole sources and without the restriction of a vanishing χ_e.

Phase images and r_π can also potentially be used to quantify the diameter of a spherical sample or the effective diameter of a point dipole. Substituting the expression $m_{Fe} = \rho V$ (where V is the volume of the sample) into Eq. [5] results in Eq. [7]:

$$a = \left(\frac{3\pi}{\gamma' \Delta\chi B_o T_E} \right)^{1/3} r_\pi \qquad (\Delta\chi > 0) \tag{7}$$

Eq. [7] can also potentially be used to estimate $\Delta\chi$, from measurements of a and r_π.

Eq. [8] follows from Eq. [7] and reveals, for a given $\Delta\chi$, an r_π value measured at one field strength and echo time is easily converted to a value corresponding to another field strength and echo time:

$$\frac{r_{\pi_2}}{r_{\pi_1}} = \left(\frac{B_{0_2} T_{E_2}}{B_{0_1} T_{E_1}}\right)^{\frac{1}{3}}$$

[8]

Therefore, under the assumption that $\Delta\chi$, or $\Delta\chi/\rho$ does not significantly vary, Eqs. [5], [7] and [8] imply the r_π values from different scanners and at different echo times can be consistently compared to determine iron content or source diameter.

Finally, the sensitivity of the method in m_{Fe} determination (δm_{Fe}) can be estimated by considering uncertainty due to white noise in the phase images, expressed by Eq. [9] as:

$$\delta m_{F_e} = \left(\frac{4\pi^2 \rho}{\gamma \Delta\chi B_o T_E}\right)\left(\frac{r_\pi^3}{\pi(SNR_{Mag})}\right)$$

[9]

where SNR_{Mag} is the SNR of the corresponding magnitude image, and a systematic error due to phase averaging over slices of finite thickness t, expressed by Eq. [10] as (see Appendix):

$$\delta m_{F_e} = \left(\frac{4\pi^2 \rho}{\gamma \Delta\chi B_o T_E}\right)\left(\frac{r_\pi^2 t}{12}\right)$$

[10]

Eqs. [5] and [7] amount to mathematical hypotheses that predict proportional relationships between the dipole phase pattern parameter r_π and sample iron mass and radius. Therefore, simple plots of these variables can be used to verify the predictions of the hypotheses and thus validate the method (see Discussion).

26

MR Phantoms

Hemosiderin, considered a breakdown product of the iron storage protein ferritin (Schenck and Zimmerman, 2004), is formed in lysosomes and is not commercially available. To mimic hemosiderin, we used a composite material consisting of ferric-oxy-hydroxide (FeOOH) nanospheres evenly distributed in chitosan (Ch-Fe) (Sipos et al., 2003). Chitosan (deacetylated chitin) is an exceptionally heat resistant polysaccharide. The 5-10 nm diameter nanospheres are sterically separated by the chitosan and very similar to the FeOOH core of ferritin, and the even distribution of iron is morphologically reminiscent of hemosiderin. Thus, the distribution of FeOOH in an amorphous organic matrix imitates the *in vivo* pathologic deposition of iron following BMB.

A Ch-Fe solution of known concentration was mixed with agarose powder (Sigma-Aldrich, St. Louis, MO) and the Ch-Fe-Agarose (Ch-Fe-Agr) combination (2% agarose) was heated in a water bath at 95° C for 20 min and then held at 95° C in a Thermomix (Eppendorf, Westbury, NY). Small volumes of the liquid Ch-Fe-Agr were pipetted into micro-centrifuge tubes (one sample per tube) containing a mixture of chloroform ($CHCl_3$) and soybean oil at room temperature and allowed to harden (Fig 2.2A). The hydrophobic oil/$CHCl_3$ mixture is both isodense and immiscible with the hydrophilic Ch-Fe-Agr. Both properties contribute to the (non-trivial) task of spherical sample formation (Fig 2.2A inset, B): the former, because neutral buoyancy prevents flattening of the drop on the tube bottom, and the latter, because of the tendency to form a configuration of minimal surface contact (ie, a spherical shape), due to the hydrophobic effect. The agarose component of the Ch-Fe-Agr sample prevents the Ch-Fe material from dispersion into the surrounding medium of the phantoms (Fig 2.2B).

27

Ch-Fe-Agr samples were finally embedded in a degassed 2% agarose gel. The embedding process consists of two stages: first agarose was poured and hardened into molds that leave narrow 'wells' in the agarose inside plastic tubes. Next, samples are placed in hot agarose (~85 C) added to the wells. The wells prevent the samples from drifting in the surrounding hardening agarose liquid and thus serve to position the samples. The temperature of the agarose was chosen to be as hot as possible to minimize air bubble formation on the surface of the Ch-Fe-Agr samples (and the resulting air bubble artifact) but still be below the agarose melting temperature to preserve the shape and prevent sample dispersion.

The iron concentration of the Ch-Fe-Agr mixture was determined by graphite furnace atomic absorption spectrometry (Varian, Inc., Palo Alto, CA) to be 1520µg/g, approximately 3 times that of whole blood (Helmer and Emerson, 1934) and 1.5 times that of red blood cells. Since iron is expected to concentrate following hemorrhage, this concentration is physiologically relevant.
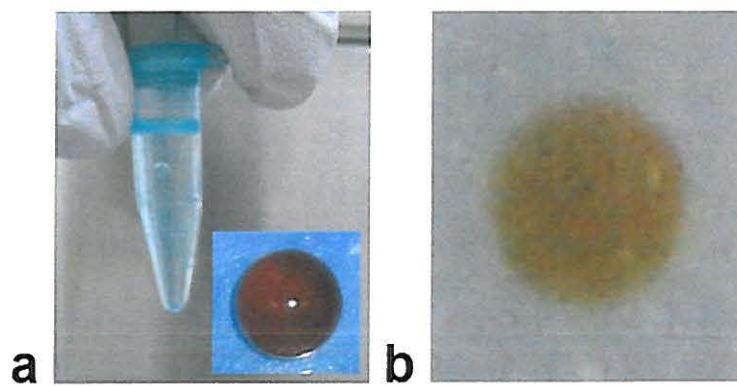
Figure 2.2: Ch-Fe-Agr Phantoms. A) Ch-Fe-Agr droplet suspended in a CHCl₃/soybean oil mixture. The hydrophobic mixture is isodense and immiscible with the hydrophilic droplet resulting in spherically shaped samples (inset). B) Embedded Ch-Fe-Agr samples retain their shapes and are discreetly confined in the phantom agarose gel medium.

Magnetic Resonance Imaging

Phantoms were scanned in an 11.7T small vertical-bore MR scanner (Bruker Biospin, Billerica MA). The SWI parameters used were: TR/TE: 60/5 ms, flip angle: 25°, matrix: 512 x 512 or 256 x 512, NEX: 1, FOV: 2.7 cm, in-plane resolution 0.0527 mm x 0.0527 mm or 0.106mm x 0.0527 mm, and 32 slices of thickness 0.084 mm. Images were taken in the coronal plane parallel to the main magnet axis.

Image and Data Processing

To remove non-dipole phase contributions, raw phase images were high-pass filtered using a 32x32 frequency domain filter (SPIN software, MRI Institute, Detroit, MI) (Fig 2.3A-C) (Wang et al., 2000). The filtering technique generally involves a tradeoff between removal of background components and preservation of the signal of interest. Therefore, the best practice is to choose the smallest possible filter size that adequately removes the background. Kernel sizes smaller than 32x32 (e.g., 8x8, 16x16) displayed significant background presence and effects in some of the phantoms images. Magnitude images were multiplied four times by a phase mask created from the high-pass filtered images (Haacke et al., 2004). Dipole symmetry in the resulting phase-enhanced magnitude images can help indicate that the filtering process has adequately removed the generally heterogenous background phase (Fig 2.3D).

Phase profiles were obtained along the minor axis of the Ch-Fe sample dipole patterns in the high-passed filtered phase images (Fig 2.3E, F) in the slice closest to the equatorial plane (see Appendix). The r_{π} values were calculated by dividing the number of pixels between and including the end-pixels corresponding to the maximum wrapped

phase (π), by 2, and multiplying this value by the horizontal resolution (Fig 2.3F).

Because the phase wrapping most likely occurs between the pixel prior to (where ($\Delta\varphi_D$ mod 2π) < π), and the pixel after wrapping (where ($\Delta\varphi_D$ mod 2π) > π), linear interpolation was used to obtain end-pixels of sub-voxel length.

Sample Diameter Measurements

After scanning, the Ch-Fe-Agr samples were removed from the phantoms and their diameters were measured using digital calipers (World Precession Instruments, Sarasota, FL) by an investigator blinded to sample mass and r_π values.

Statistical and Sensitivity Analysis

The predicted relationships between the mass of iron m_{Fe}, radius a, and r_π^3 of the phantom samples were tested by linear regression analysis using SigmaPlot version 11 (Systat Software, Inc., Chicago, IL). Plots of m_{Fe} vs. r_π^3 and a vs. r_π were constructed along with best-fit least squares regression lines. Statistical significance was considered at $p < 0.05$. Comparison of Eqs. [5], [9], and [10] reveals that δm_{Fe} can be determined by substitution of the m_{Fe} vs. r_π^3 regression line slope and scan parameters into Eqs. [9] and [10]. Accordingly, estimates of the sensitivity of the method (ie, estimated lower iron detection limit) were calculated.

Results

Two samples were removed from analysis because of 1) a damaged sample and 2) probable mass measurement error and twelve phantoms (containing one sample each)

31

were analyzed. All Ch-Fe-Agr samples showed typical dipole patterns in magnitude, raw phase, high pass-filtered and phase-enhanced magnitude images (Fig 2.3A-D). The magnitude images displayed hypointense regions in shapes and patterns consistent with reports of dipole artifacts in the literature: clover leaf shaped for medial, and tri-lobular for lateral slices parallel to the dipole axis (Bos et al., 2003; Kim et al., 1993; Pintaske et al., 2006b) (Fig 2.3A). Raw phase images displayed dipoles blended with background zebra stripe artifact (Haacke et al., 1999), however, when the images were high-pass filtered they typically exhibited dipole patterns with clearly visible phase wraps surrounded by a largely homogenous background (Fig 2.3C). Phase profiles in the filtered phase images generally had 'flat' left and right edges and were very similar in form to theoretical profiles (Figs 2.1B, 2.3F). In addition, average intensity values measured in ROI centered at approximately $\sim 3 r_\pi$ units along the minor axis from the dipole center were within one standard deviation of zero phase for ten separate phantoms.

Iron mass, radii, r_π, r_π^3 and δm_{Fe} values for 12 Ch-Fe-Agr samples are shown in Table 2.1. Sample iron mass vs. r_π^3 is plotted in Fig 2.4A, and exhibits a strong linear relationship ($R^2 = 0.972$, $p < 0.001$) between variables with a slope of 2810 $\mu g/cm^3$ ($p < 0.001$). The y-intercept of the plot is -0.084 μg, which is smaller than white noise levels for seven phantoms with the largest mass values (Samples 6 – 12, Table 2.1) and is not significantly different from zero (p = 0.874). Thus, the plot displays the proportional relationship between the variables predicted by Eq. [5].

A plot of sample radii vs. corresponding r_π values similarly demonstrates a strong linear relationship between these variables ($R^2 = 0.970$, $p < 0.001$) with a dimensionless slope of 0.837. The y-intercept is -0.0137 cm, which narrowly misses statistical

32

significance ($p = 0.06$) (Fig 2.4B). Thus, the proportional relationship predicted by Eq. [7] is confirmed by our experimental results. Using the slope from Fig 2.4B and Eq. [7], $\Delta\chi$ for the Ch-Fe-Agr samples (with respect to water) is found to be 1.03 ppm, roughly 20 times larger than the estimate of $\Delta\chi = 0.05$ppm (with respect to CSF) given in (Duyn et al., 2007) for gray matter susceptibility due to storage protein (ferritin/hemosiderin) iron. This order of magnitude difference suggests the Ch-Fe-Agr preparation reasonably mimics $\Delta\chi$ for pathological iron deposition.

Mass sensitivities due to white noise $(\delta m_{Fe})_\varphi$ and finite slice phase averaging $(\delta m_{Fe})_t$ corresponding to measured r_π values together with mass differences between successive phantom samples ($\Delta m = m_{n+1} - m_n$) are also shown in Table 2.1. A close comparison between Table 2.1 and the m_{Fe} vs. r_π plot of Fig 2.4A reveals that point pairs with Δm values as low as 0.3 μg (points 2 and 3), less than 1 μg (points 1 and 2, 5 and 6, 6 and 7, 11 and 12), and less than 2 μg (points 3 and 4, and 10 and 11) are clearly distinguished and appear correctly in the plot (i.e., lower iron content has the lower r_π^3 value). In each of these cases, Δm is above the white noise level $(\delta m_{Fe})_\varphi$ and averaging error $(\delta m_{Fe})_t$ for each point in the point pair. Points 4 and 5, and 8 and 9 with larger Δm values and $\Delta m >$ both δm values are also correctly displayed. In contrast, point numbers 9 and 10 have a Δm value comparable with the white noise levels and less than the averaging error for each point ($\Delta m = 0.2$ μg, $(\delta m_{Fe})_\varphi$(point 9) = $(\delta m_{Fe})_\varphi$(point 10) = 0.2 μg, $(\delta m_{Fe})_t$(point 9) = 0.6 μg, and $(\delta m_{Fe})_t$(point 10) = 0.5 μg) and are not correctly displayed. In addition, points 7 and 8 overlap even though Δm equals 0.9 μg and is above the noise level. This is possibly attributable to the larger pixel width of point 7, and thus a larger uncertainty in r_π than the neighboring point 8 (Table 2.1).
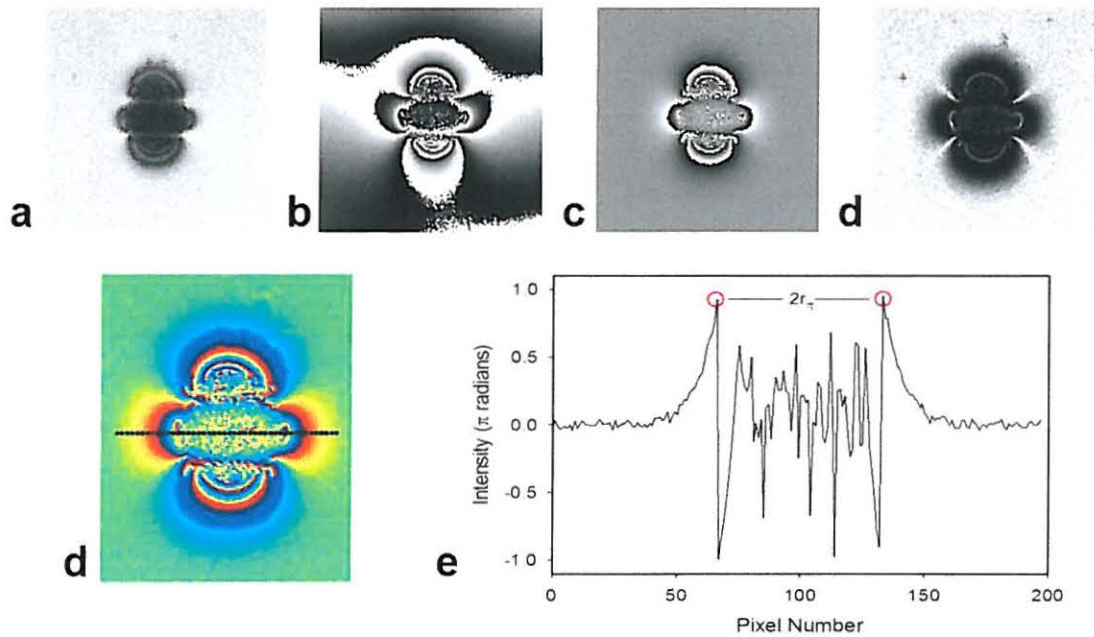
Figure 2.3: Ch-Fe-Agr Phantom Images. A) Magnitude, B) raw phase, C) high pass-filtered and D) phase-enhanced magnitude images of a phantom containing a Ch-Fe-Agr sample. The distinctive appearance of the samples is due to the well known dipole artifact where the sample behaves as magnetic dipole and perturbs the local field. E) Color mapped magnification of the dipole with a profile line drawn through it, and F) the wrapped phase profile of the dipole. r_π values were determined from the two 'end-pixels' that correspond to the maximum phase values (shown in red) in the wrapped phase profile. r_π is approximately ½(# of pixels between and including end-pixels)x(pixel resolution). However, because wrapping generally occurs between an end-pixel and the one medially adjacent, linear interpolation is used to obtain sub-voxel lengths for the end pixels. This correction is applied to give r_π. Note the similarities between the experimental dipole and phase profile in E and F, respectively compared with the theoretical dipole and profile in Fig 2.1B and C.

34

Table 2.1: Phantom Sample Data - The table contains iron mass (m_{Fe}), radii (a), r_π, and r_π^3 data (plotted in Fig 2.4A & B) as well as δm_{Fe} sensivity data for 12 Ch-Fe-Agr phantom samples. The sensitivity data for $(\delta m_{Fe})_\varphi$ and $(\delta m_{Fe})_t$ is calculated according to Eqs. [9] and [10] respectively. However, since $\Delta\chi$ is unknown, the first factor in the equations $(4\pi^2\rho/\gamma\Delta\chi B_0 T_E)$ is replaced by the slope of the graph in Fig 2.4A (compare Eq. [5] with Eqs. [9] and [10]). $m_{n+1}-m_n$ is the mass difference between successive sample data points.

Sample	m (µg)	a (mm)	r_π (mm)	r_π^3 (mm³)	[a] $m_{n+1}-m_n$ (µg)*	[b] $(\delta m_{Fe})_\varphi$ (µg)	[c] $(\delta m_{Fe})_t$ (µg)
*1	1.0±0.4	0.42±0.04	0.75±0.12	0.4±0.2	0.9±0.6	0.011	0.11
*2	1.9±0.4	0.72±0.04	0.92±0.10	0.8±0.3	0.3±0.6	0.02	0.2
3	2.2±0.4	0.69±0.04	1.01±0.08	1.0±0.3	1.6±0.6	0.04	0.2
4	3.8±0.5	0.84±0.04	1.07±0.08	1.2±0.3	2.3±0.8	0.05	0.2
5	6.1±0.7	0.85±0.04	1.20±0.07	1.7±0.3	0.9±1.0	0.08	0.3
6	7.0±0.7	0.97±0.04	1.37±0.06	2.6±0.4	0.9±1.1	0.11	0.4
*7	7.9±0.8	1.06±0.04	1.48±0.08	3.3±0.5	0.9±1.2	0.11	0.4
8	8.8±0.9	1.08±0.04	1.50±0.06	3.3±0.4	4.8±1.5	0.14	0.4
9	13.6±1.3	1.30±0.04	1.75±0.05	5.3±0.5	0.2±1.8	0.2	0.6
10	13.7±1.3	1.31±0.04	1.67±0.05	4.6±0.5	1.8±1.9	0.2	0.5
11	15.5±1.4	1.33±0.04	1.70±0.05	5.0±0.5	0.7±2.0	0.2	0.6
12	16.2±1.5	1.38±0.04	1.80±0.05	5.8±0.5	N/A	0.3	0.6

[a] $m_{n+1} - m_n$ refers to the mass difference between successive sample data points (eg, the mass difference between phantom sample 2 and 3 is 0.3 µg = (2.2 – 1.9) µg

[b] $(\delta m_{Fe})_\varphi$ refers to uncertainty in m_{Fe} due to white noise in phase measurements (Eq. (9))

[c] $(\delta m_{Fe})_t$ refer to uncertainty in m_{Fe} due to averaging in a phase image slice of finite thickness t (Eq. (10)).

*Phantom samples scanned using a 512x256 matrix (all other phantom were scanned at 512x512).

A) plot: m_{Fe} (µg) vs r_{π}^{3} (cm^3)

$m_{Fe} = 2810 r_{\pi}^{3} - 0.0854$
$R^2 = 0.972$

B) plot: a (cm) vs r_{π} (cm)

$a = 0.837 r_{\pi} - 0.0137$
$R^2 = 0.970$
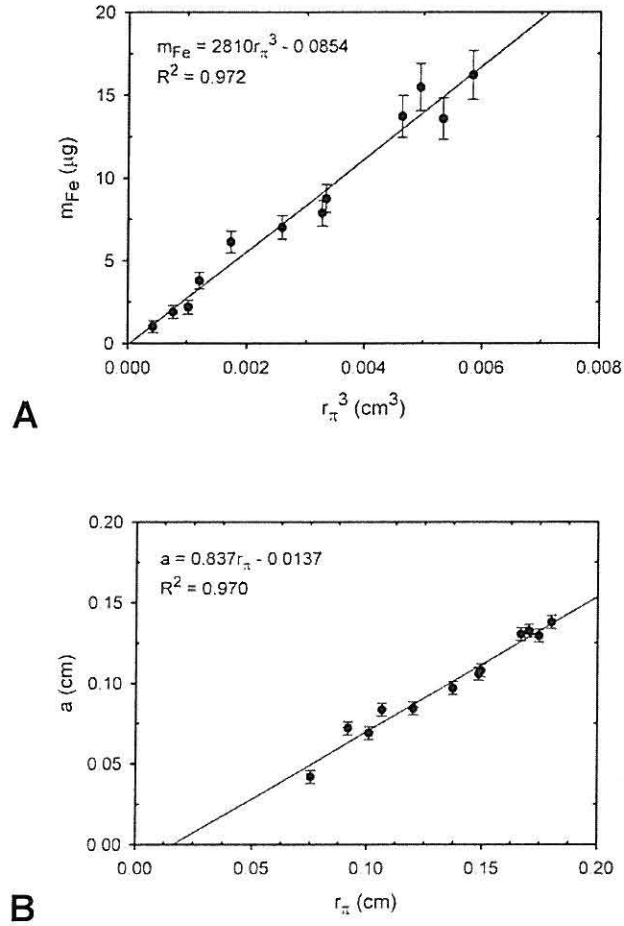
Figure 2.4: Ch-Fe-Agr Phantom Data. A) The iron mass (m_{Fe}) of Ch-Fe-Agr samples is plotted against r_{π}^{3}. The mathematical hypothesis behind the quantification method (Eq. [5]) predicts a proportional relationship between these variables. The strong linear relationship ($R^2 = 0.972$, $p < 0.001$) and vanishing y-intercept value (-0.084 µg, statistically indifferent from zero, $p = 0.874$) corroborates the hypothesis and validates our method for punctate iron quantification. The slope of the graph is 2810 µg/cm^3 ($p < 0.001$). **B)** Ch-Fe-Agr samples were removed from the agarose medium of the phantoms and their diameters were measured with digital calipers. Sample radii, a, were plotted against corresponding r_{π} values. The plot shows a strong linear relationship between variables ($R^2 = 0.970$, $p < 0.001$) and a y-intercept statistically indifferent from zero (-0.0137 cm, $p = 0.06$). A proportional relationship between variables is predicted by Eq. [7]. The dimensionless slope of the graph is 0.837, $p < 0.001$).

36

Discussion

The purpose of the present study was to investigate iron quantification of punctate iron sources using phase images. The key observation of this paper is that geometric properties of magnetic dipole field patterns obtained from filtered MR phase images can be used to quantify iron content, diameter and susceptibility of punctate sources (Eqs. [5] and [7]). While to date, MR iron quantification approaches have used magnitude images and/or focused on regionally distributed iron, we propose a method using phase images and focusing on punctate iron sources. Phantoms constructed with a unique biologically relevant mimic of hemosiderin were used to validate the method. Our primary finding is the expected linear relationship between m_{Fe} and the cube of r_π. This relationship is predicted by Eq. [5] and thus demonstrates the validity of the proposed method and the underlying theory. Similarly, the linear relationship between the sample radius a and r_π is predicted by Eq. [7] and this finding verifies that the r_π parameter can effectively determine the radius of punctate magnetic dipole source. In addition, sample iron masses were resolved consistent with the sensitivities predicted by Eqs. [9] and [10].

The validated Eqs. [5] and [7] together with r_π measurements, can be applied toward quantification in two ways: 1) as calibration curves obtained from samples of known mass (radii) that are then used to determine unknown masses (radii) of different samples of similar material, or 2) using known or measured ρ and/or $\Delta\chi$, mass and radii can be calculated directly from the equations. Moreover, approach 1) can also be used to calculate ρ, χ_i, χ_e, $\Delta\chi$, or $\Delta\chi/\rho$ with appropriate knowledge of the other equation parameters. Finally, under the assumption(s) of constant $\Delta\chi$ or $\Delta\chi/\rho$, the r_π parameter

37

theoretically can be consistently compared between scanners, field strengths and echo times (Eq. [8]).

Because the presence of paramagnetic iron leads to local changes in magnetic susceptibility and spin dephasing, several investigators have sought to quantify or correlate brain iron using decreased T_2 relaxation times (or increased relaxation rate $R_2 = 1/T_2$) (Bartzokis et al., 1993; Haacke et al., 2005; House et al., 2007), GRE T_2^* methods (Gilissen et al., 1999), T_1/T_2 ratio (Jara et al., 2006), T_2' (Gelman et al., 1999; Ordidge et al., 1994), and T_2 histogram methods (MacKay et al., 2006). However, a fundamental weakness of these conventional magnitude methods is their dependence on complex relaxation mechanisms (e.g., spin-spin coupling) that possibly vary across tissue types, disease states, and experimental parameters (Gossuin et al., 2007; Jensen et al., 2009). Phase however, is directly proportional to the susceptibility variations and does not depend on a particular coupling mechanism. Tissue phase differences are theoretically independent of T_1 and T_2 tissue parameters and RF phase (Haacke et al., 2005). Thus, phase images are expected to be largely free from the influence of confounding tissue water and more consistent across tissue types and states than T_1, T_2, T_2^* and T_2' approaches. In addition, unlike magnitude images that suffer signal loss when diffusion effects are significant (ie, outside the static dephasing regime), bulk phase shifts due to internal or external time independent field inhomogeneities are unchanged by water diffusion. The relationship between susceptibility and phase has been exploited in several studies. Oxygen dependent susceptibility differences were used to separate arteries and veins (Wang et al., 2000). Unwrapped phase maps have been used to obtain iron susceptibility measurements in gerbil cardiac tissue however, the calculation was

complicated by constant phase term (hyperfine contact shift) (Wang et al., 2005). The high pass filtering used in the present study beneficially removes constant phase terms and the resulting complications of data analysis. Cheng et al., used a more complicated summation of the complex MR signal (i.e., with respective real and imaginary magnitude and phase components) that uses most surrounding pixel information to quantify the susceptibility of cylindrical phantoms (Cheng et al., 2007).

Several other authors have studied MR dipole properties (Bos et al., 2003; Kim et al., 1993; Pintaske et al., 2006a, 2006b) including application to phase images (Dixon et al., 2009; Mills et al., 2008; Robson and Hall, 2005). The r_π parameter was used to measure magnetic dipole moments of cylindrical phantoms but such measurements were found to be inaccurate for larger moments when compared to theoretical calculations. This could possibly be explained by inadequate background phase removal by the empty scanner subtraction technique employed (Robson and Hall, 2005). In our study, we used high-pass homodyne filtering to remove background phase effects, significantly higher resolution images, and a modified r_π parameter with subpixel resolution and obtained consistent results. However, sample moments in our study are three orders of magnitude smaller than (Robson and Hall, 2005) so direct comparison may not be fully straight forward. Dixon et al. recently used the expected point dipole spatial phase distribution to estimate the known iron content of three injections of iron oxide particles into rat leg muscle. Better estimates from fitting phase difference images from dual echo GRE (where a significant portion of background phase is removed by the subtraction) were reported compared to single echo GRE phase images fits (without background phase removal and Lorentz correction) that yielded inaccurate estimates (Dixon et al., 2009).

Mills et al., found dipole pattern templates robust even in the presence of noise in identifying dipole impressions in phantoms and magnetic particle labeled rat heart (Mills et al., 2008). Similarly, because r_π is associated with the first phase wrap of the dipole pattern, it can be robustly distinguished in noisy phase profiles. The importance of modeling punctate sources as magnetic dipoles may increase with high field scanner adoption and resulting greater paramagnetic effects lead to enhanced dipole patterns. In addition, while dipole patterns have been considered (undesirable) artifacts, the quantification technique we describe can be facilitated by scan parameters that enhance rather than minimize dipole patterns. For example, longer echo times increase phase wrapping and thus aid in the determination of r_π values from low content iron deposits. However, loss of signal due to longer T_E may need to be compensated for to achieve satisfactory results.

The potential role of paramagnetic material as a biomarker or agent of disease makes its noninvasive quantification by MR potentially valuable. An important first question concerning the usefulness of the method is if the technique is sensitive enough to measure clinically or experimentally relevant iron levels and source sizes. A sphere of red blood cells of diameter 1mm to 4mm and iron concentration of 1100µg/g, contains approximately 0.6 to 37 µg of iron. As iron is expected to concentrate following heme breakdown and hemosiderin formation, these estimates can be considered lower limits of iron mass in BMB with these diameters. For our phantom samples the largest $(\delta m_{Fe})_\varphi$ and $(\delta m_{Fe})_t$ predicted by Eqs. (9) and (10) were 0.3 and 0.6 µg, respectively. The method was able to resolve fairly consistently at the level of $1 - 2$ µg. Seven of the 11 pairs of successive points were resolved with best estimate mass differences less than 2 µg, and 5

were resolved at less than 1 μg. Therefore, the quantification method is capable of iron mass resolution at levels relevant to BMB. The smallest phantom sample (Sample 1, Table 2.1) had an r_π value of 0.75mm, corresponding to 7.1 interpolated pixels. A five pixel distance is probably a reasonable lower limit estimate for r_π before the dipole pattern becomes indistinct due to pixilation. Writing $r_\pi = 5s$, where s is the pixel width and using Eq [7], the ratio of minimum sample diameter (d_{min}) to pixel width is given by equation 11:

$$\frac{d_{min}}{s} \approx \left(\frac{3000\pi}{\gamma \Delta X B_o T_E} \right)^{1/3}$$

[11]

Using the slope from Fig 2.4B and Eq. [7], Eq. [11] gives a ratio of 8.37 for the current experiment, corresponding to a d_{min} of 0.45mm. Using $\Delta\chi = 2.5$ppm, $B_0 = 7$T, $T_E = 30$ms, and s = 240μm gives a ratio of 4.1 and a d_{min} of 0.98mm. Therefore, the method is applicable to source sizes relevant to BMB. Interestingly, sub-voxel ($d_{min}/s < 1$) iron source quantification using current technology is theoretically achievable for tissue $\Delta\chi \sim$ 300ppm (eg, due to biogenic magnetite). Another possible application of the technique is to assess the location or viability of magnetically labeled cells clusters. Assuming 5 pg iron and magnetic moments of 4.9×10^{-13} A m^2 per cell (Smirnov et al., 2006), clusters of 10^5 to 10^6 SPIO labeled cells with volumes 1 to 10 μl (Pintaske et al., 2006b) contain 0.5 – 5 μg of iron and have susceptibilities slightly larger but of the same order of magnitude as our Ch-Fe-Agr samples. That the volumes, radii, and iron content of these clusters is comparable with at least the smallest of the samples and that r_π can be used to measure radii unobscured by the blooming effect, shows the potential of application of the method to magnetically labeled cells. Finally, brain calcium deposits also cause

hypointensities of GRE images confounding the identification of BMB. However, since calcium is diamagnetic, dipole patterns in phase images are distinct from paramagnetic iron dipole patterns. Thus, phase images of dipole patterns could potentially be used to distinguish between punctate calcium and iron brain deposits (Yamada et al., 1996) as well as quantify the content and effective radius of punctate calcium deposits.

There are several limitations in this study and to our quantification method. 1) Our approach assumes background phase has been reduced to negligible levels. Background phase removal is a fundamental problem in phase imaging and several approaches have been used including: estimating phase from modeled susceptibility sources (Neelavalli et al., 2009), numerical smooth and fit techniques (Duyn et al., 2007), simple subtraction (Cheng et al., 2007), and homodyne high pass filtering (Wang et al., 2000). Since phase dipole patterns are the result of aliasing, all but the latter method necessitate an additional phase unwrapping step before background removal. In our phantoms, background phase levels were adequately removed and dipole phase frequencies were assumed greater than the removed background frequencies. Despite the filtering, a linear relationship as expected from Eq. [5] was still seen. 2) We have assumed spherical symmetry for dipole samples and have produced high quality Ch-Fe-Agr spheres. This assumption allows iron content and sample radii to be determined from the three dimensional dipole pattern using only a one dimensional measurement along a single phase profile. The method is expected to breakdown for large deposits of irregular shape. However, for point dipoles in the far field the actual geometry of the susceptibility source in not important. For larger objects the suitability of the method could be assessed by the degree of dipole symmetry. 3) Because r_π is determined from

only four points in the phase profile the method might be expected to be prone to noise. However, the fact that $\Delta\varphi_D$ increases rapidly near r_π (as $1/r^3$) above a flat background tends to reduce the effect of noise on r_π measurements. 4) Eq. [11] reveals the smallest source object for which r_π can be determined is limited by s, and that the ratio d_{min}/s is determined by $\Delta\chi$, B_0, and T_E. At high field (eg, 3T, 7T or 11.7T) and with a paramagnetic iron concentration on the order of mg/g tissue, d_{min}/s ratios from 4 to 9 are expected, depending on field strength and T_E. However, with the availability of high resolution imaging (eg, pixel sizes ranging from 50 to 500um), minimum source diameters of 250um to 1.2mm are possible using typical parameters. 5) Finally, there are several important issues and challenges to be met when attempting to apply the method beyond phantom systems with idealized geometry and magnetic compartments. Application and validation of similar methods to real tissue will necessitate studies concerning the chemical, physical and magnetic properties and spatial features of relevant biomolecules and tissue types. In human tissues, it will be important to determine and characterize susceptibilities, densities, and related properties of brain iron deposits and surrounding tissue, including hemosiderin and ferritin iron core components. Here, we have used carefully prepared samples of ferric oxyhydroxide and have assumed constant density and susceptibility. In real tissues, especially under pathologic conditions, these parameters can be expected to vary. For example, the particular nature of the complicated and potentially disease-variable iron deposit crystal structure and spin state will affect susceptibility and could complicate quantification. Whether these densities and susceptibilities of deposits vary with a narrow distribution and allow the application

of the linear Eqs. [5] and [7] in useful tolerances, is an important specific question that must be addressed.

Our technique based on r_π is simple, does not require complex image sequences or processing techniques, and is shown here to be effective. Nevertheless, several improvements are possible and under investigation. Increases in method SNR could be achieved by fitting the phase profile instead of using only the wrapping points. This would require a phase unwrapping step that can be problematic because of typically noisy dipole centers. Rapid dephasing due to high susceptibility leads to substantial signal loss, especially if enhanced aliasing is required produce a dipole pattern (ie, low iron content sources). On the other hand, SNR gains are expected for higher phase values that increase as $1/r^3$ toward the dipole center before signal loss dominates. Alternately and similarly, the method can be extended to use data from the second phase wrap ($\varphi_D = 3\pi$, Fig 2.1D) (enhanced by longer echo times) provided there is sufficient SNR available and if an interpolation can still adequately be made between the phase in adjacent pixels.

Conclusion

We investigated iron quantification punctate iron sources modeled as magnetic dipoles using a phase technique. Geometric properties of dipole field patterns (r_π) in SWI phase images were hypothesized to be mathematically related to sample iron content and radius. For a given magnetic source, the limit of the sensitivity of the technique is the in-plane resolution and slice thickness of the image. The technique was explored using MR phantoms constructed with a unique ferric iron-containing composite material that serves as a biologically relevant mimic for hemosiderin. Our experimental results are in

excellent agreement with our theoretical predictions corroborating the hypotheses and validating the method. The present study is a first step toward the use of similar methods in experimental and clinical settings. The quantification and monitoring of iron content and source diameter of BMB and magnetically labeled cells are possible application areas of special interest.

Appendix

Eq. (5) implies the first order sensitivity of iron sample mass is related to measurement uncertainty in φ ($\delta\varphi$) and r_π (δr_π) and by the equations (A1) and (A2) respectively:

$$\delta m_{F_e} = \left(\frac{4\pi\rho}{\gamma' \Delta X B_o T_E} \right) r_\pi^3 \delta\phi$$

[A1]

$$\delta m_{F_e} = \left(\frac{12\pi^2\rho}{\gamma' \Delta X B_o T_E} \right) r_\pi^2 \delta r_\pi$$

[A2]

$\delta\varphi$ in phase images is related to the SNR of corresponding magnitude image (SNR_{Mag}) by the expression $\delta\varphi = 1/SNR_{Mag}$ (Haacke et al., 1999), which upon substitution into Eq. [A1] results in Eq. [9]. An estimate of δr_π due to phase averaging over a slice of thickness t can be calculated by integrating the complex phase over the slice according to Eq. [A3] (Fig 2.A1):

$$e^{i\bar{\phi}} = \frac{1}{2\alpha} \int_{-\alpha}^{\alpha} e^{i\pi\cos(\alpha)} d\alpha$$

[A3]

45
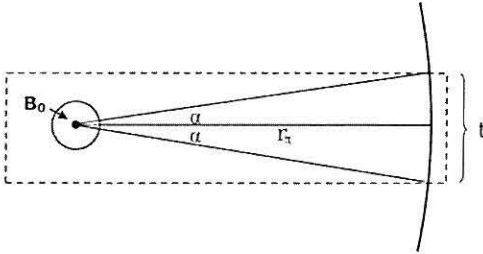
Figure 2.A1: Uncertainty in r_π (δr_π) Due to Averaging Over Finite Slice Thickness. The figure depicts the position of a phase image slice (dotted rectangle) with respect to the dipole source (circle) and field pattern (not drawn to scale). The arc is a portion of the contour line $\Delta\varphi_D = \pi$ of the field pattern within the plane perpendicular to the main field (B_0) axis and passing through the center of the source. Thus, the radius of curvature of the arc is r_π. Note that this plane is perpendicular to the coronal planes where the phase images were acquired. Thus the image slice contains the main field axis which projects perpendicularly outward from the page (vector tip of B_0, arrow). The phase shift over the slice can be estimated from Eq. [A3], and used to estimate the resulting δr_π (see text for details).

Under the assumption that $t/2$ is small compared to r_π, the fractional uncertainty $\delta\varphi/\varphi = \delta\varphi/\pi \approx t/(12r_\pi)$. Because $\varphi \sim 1/r^3$, $\delta\varphi/\varphi \approx 3\delta r/r$, and $\delta r_\pi \approx t/36$. Combining this result with Eq. [A2] yields Eq. [10].

References

Akter M, Hirai T, Hiai Y, Kitajima M, Komi M, Murakami R, Fukuoka H, Sasao A, Toya R, Haacke EM, Takahashi M, Hirano T, Kai Y, Morioka M, Hamasaki K, Kuratsu J-I, Yamashita Y. Detection of hemorrhagic hypointense foci in the brain on susceptibility-weighted imaging clinical and phantom studies. Academic Radiology 2007 14(9):1011-1019.

Andersen JK. Iron dysregulation and Parkinson's disease. Journal of Alzheimer's Disease: JAD 2004 6(6 Suppl):S47-52.

Atlas SW, Mark AS, Grossman RI, Gomori JM. Intracranial hemorrhage: gradient-echo MR imaging at 1.5 T. Comparison with spin-echo imaging and clinical applications. Radiology 1988 168(3):803-807.

Bartzokis G, Aravagiri M, Oldendorf WH, Mintz J, Marder SR. Field dependent transverse relaxation rate increase may be a specific measure of tissue iron stores. Magn Reson Med 1993 29(4):459—464.

Bizzi A, Brooks RA, Brunetti A, Hill JM, Alger JR, Miletich RS, Francavilla TL, Di Chiro G. Role of iron and ferritin in MR imaging of the brain: a study in primates at different field strengths. Radiology 1990 177(1):59-65.

Bos C, Viergever MA, Bakker CJG. On the artifact of a subvoxel susceptibility deviation in spoiled gradient-echo imaging. Magnetic Resonance in Medicine 2003 50(2):400-404.

Bush AI. The metallobiology of Alzheimer's disease. Trends Neurosci 2003 26(4):207-214.

Cheng Y-CN, Hsieh C-Y, Neelavalli J, Liu Q, Dawood MS, Haacke EM. A complex sum method of quantifying susceptibilities in cylindrical objects: the first step toward quantitative diagnosis of small objects in MRI. Magn Reson Imaging 2007 25(8):1171—1180.

Cordonnier C, Salman RA-S, Wardlaw J. Spontaneous brain microbleeds: systematic review, subgroup analyses and standards for study design and reporting. Brain 2007 130(Pt 8):1988—2003.

Dixon WT, Blezek DJ, Lowery LA, Meyer DE, Kulkarni AM, Bales BC, Petko DL, Foo TK. Estimating amounts of iron oxide from gradient echo images. Magnetic Resonance in Medicine: Official Journal of the Society of Magnetic Resonance in Medicine / Society of Magnetic Resonance in Medicine 2009 61(5):1132-1136.

Duyn JH, Gelderen Pv, Li T-Q, Zwart JAd, Koretsky AP, Fukunaga M. High-field MRI of brain cortical substructure based on signal phase. Proc Natl Acad Sci U S A 2007 104(28):11796—11801.

Gaasch JA, Lockman PR, Geldenhuys WJ, Allen DD, Van der Schyf CJ. Brain iron toxicity: differential responses of astrocytes, neurons, and endothelial cells. Neurochemical Research 2007 32(7):1196-1208.

Gelman N, Gorell JM, Barker PB, Savage RM, Spickler EM, Windham JP, Knight RA. MR Imaging of Human Brain at 3.0 T: Preliminary Report on Transverse Relaxation Rates and Relation to Estimated Iron Content. Radiology 1999 210(3):759-767.

Gilissen EP, Jacobs RE, Allman JM. Magnetic resonance microscopy of iron in the basal forebrain cholinergic structures of the aged mouse lemur. Journal of the Neurological Sciences 1999 168(1):21-27.

Gossuin Y, Gillis P, Muller RN, Hocq A. Relaxation by clustered ferritin: a model for ferritin-induced relaxation in vivo. NMR in Biomedicine 2007 20(8):749-756.

Greenberg SM, Vernooij MW, Cordonnier C, Viswanathan A, Al-Shahi Salman R, Warach S, Launer LJ, Van Buchem MA, Breteler MMB. Cerebral microbleeds: a guide to detection and interpretation. The Lancet Neurology 2009 8(2):165-174.

Haacke EM, Ayaz M, Khan A, Manova ES, Krishnamurthy B, Gollapalli L, Ciulla C, Kim I, Petersen F, Kirsch W. Establishing a baseline phase behavior in magnetic resonance imaging to determine normal vs. abnormal iron content in the brain. J Magn Reson Imaging 2007 26(2):256—264.

Haacke EM, Brown RW, Thompson MR, Venkatesan R. Magnetic Resonance Imaging, Physical Principles and Sequence Design: Wiley-Liss; 1999.

Haacke EM, Cheng NYC, House MJ, Liu Q, Neelavalli J, Ogg RJ, Khan A, Ayaz M, Kirsch W, Obenaus A. Imaging iron stores in the brain using magnetic resonance imaging. Magn Reson Imaging 2005 23(1):1—25.

Haacke EM, Xu Y, Cheng Y-CN, Reichenbach JrR. Susceptibility weighted imaging (SWI). Magn Reson Med 2004 52(3):612—618.

Helmer O, Emerson C. The iron content of whole blood in normal individuals. J Biol Chem 1934 104:157-161.

House MJ, Pierre TGS, Kowdley KV, Montine T, Connor J, Beard J, Berger J, Siddaiah N, Shankland E, Jin L-W. Correlation of proton transverse relaxation rates (R2) with iron concentrations in postmortem brain tissue from alzheimer's disease patients. Magn Reson Med 2007 57(1):172—180.

Jara H, Sakai O, Mankal P, Irving RP, Norbash AM. Multispectral quantitative magnetic resonance imaging of brain iron stores: a theoretical perspective. Top Magn Reson Imaging 2006 17(1):19—30.

Jensen JH, Szulc K, Hu C, Ramani A, Lu H, Xuan L, Falangola MF, Chandra R, Knopp EA, Schenck J, Zimmerman EA, Helpern JA. Magnetic field correlation as a measure of iron-generated magnetic field inhomogeneities in the brain. Magnetic Resonance in Medicine: Official Journal of the Society of Magnetic Resonance in Medicine / Society of Magnetic Resonance in Medicine 2009 61(2):481-485.

Kim JK, Kucharczyk W, Henkelman RM. Cavernous hemangiomas: dipolar susceptibility artifacts at MR imaging. Radiology 1993 187(3):735-741.

MacKay A, null n, Vavasour I, Bjarnason T, Kolind S, Mädler B. Insights into brain microstructure from the T2 distribution. Magn Reson Imaging 2006 24(4):515—525.

Mills PH, Wu Y-JL, Ho C, Ahrens ET. Sensitive and automated detection of iron-oxide-labeled cells using phase image cross-correlation analysis. Magnetic Resonance Imaging 2008 26(5):618-628.

Neelavalli J, Cheng Y-CN, Jiang J, Haacke EM. Removing background phase variations in susceptibility-weighted imaging using a fast, forward-field calculation. Journal of Magnetic Resonance Imaging: JMRI 2009 29(4):937-948.

Neema M, Arora A, Healy BC, Guss ZD, Brass SD, Duan Y, Buckle GJ, Glanz BI, Stazzone L, Khoury SJ, Weiner HL, Guttmann CRG, Bakshi R. Deep gray matter involvement on brain MRI scans is associated with clinical progression in multiple sclerosis. Journal of Neuroimaging: Official Journal of the American Society of Neuroimaging 2009 19(1):3-8.

Nighoghossian N, Hermier M, Adeleine P, Blanc-Lasserre K, Derex L, Honnorat J, Philippeau F, Dugor JF, Froment JC, Trouillas P. Old microbleeds are a potential risk factor for cerebral bleeding after ischemic stroke: a gradient-echo T2*-weighted brain MRI study. Stroke; a Journal of Cerebral Circulation 2002 33(3):735-742.

Ogg RJ, Langston JW, Haacke EM, Steen RG, Taylor JS. The correlation between phase shifts in gradient-echo MR images and regional brain iron concentration. Magn Reson Imaging 1999 17(8):1141—1148.

Ordidge RJ, Gorell JM, Deniau JC, Knight RA, Helpern JA. Assessment of relative brain iron concentrations using T2-weighted and T2*-weighted MRI at 3 Tesla. Magn Reson Med 1994 32(3):335—341.

Pintaske J, Müller-Bierl B, Schick F. Effect of spatial distribution of magnetic dipoles on Lamor frequency distribution and MR Signal decay—a numerical approach under static dephasing conditions. MAGMA 2006a 19(1):46—53.

Pintaske J, Müller-Bierl B, Schick F. Geometry and extension of signal voids in MR images induced by aggregations of magnetically labelled cells. Phys Med Biol 2006b 51(18):4707—4718.

Reichenbach JR, Venkatesan R, Schillinger DJ, Kido DK, Haacke EM. Small vessels in the human brain: MR venography with deoxyhemoglobin as an intrinsic contrast agent. Radiology 1997a 204(1):272-277.

Robson P, Hall L. Identifying particles in industrial systems using MRI susceptibility artefacts. AIChE Journal 2005 51(6):1633-1640.

Scheid R, Preul C, Gruber O, Wiggins C, von Cramon DY. Diffuse axonal injury associated with chronic traumatic brain injury: evidence from T2*-weighted gradient-echo imaging at 3 T. AJNR American Journal of Neuroradiology 2003 24(6):1049-1056.

Schenck JF, Zimmerman EA. High-field magnetic resonance imaging of brain iron: birth of a biomarker? NMR in biomedicine 2004 17(7):433-445.

Sipos P, Berkesi O, Tombácz E, Pierre TGS, Webb J. Formation of spherical iron(III) oxyhydroxide nanoparticles sterically stabilized by chitosan in aqueous solutions. J Inorg Biochem 2003 95(1):55—63.

Smirnov P, Gazeau F, Beloeil JC, Doan BT, Wilhelm C, Gillet B. Single-cell detection by gradient echo 9.4 T MRI: a parametric study. Contrast Media & Molecular Imaging 2006 1(4):165-174.

Tong KA, Ashwal S, Holshouser BA, Nickerson JP, Wall CJ, Shutter LA, Osterdock RJ, Haacke EM, Kido D. Diffuse axonal injury in children: clinical correlation with hemorrhagic lesions. Ann Neurol 2004 56(1):36—50.

Tong KA, Ashwal S, Holshouser BA, Shutter LA, Herigault G, Haacke EM, Kido DK. Hemorrhagic shearing lesions in children and adolescents with posttraumatic diffuse axonal injury: improved detection and initial results. Radiology 2003 227(2):332—339.

Viswanathan A, Chabriat H. Cerebral microhemorrhage. Stroke; a Journal of Cerebral Circulation 2006 37(2):550-555.

Vymazal J, Klempír J, Jech R, Zidovská J, Syka M, Růzicka E, Roth J. MR relaxometry in Huntington's disease: correlation between imaging, genetic and clinical parameters. Journal of the Neurological Sciences 2007 263(1-2):20-25.

Wang Y, Yu Y, Li D, Bae KT, Brown JJ, Lin W, Haacke EM. Artery and vein separation using susceptibility-dependent phase in contrast-enhanced MRA. J Magn Reson Imaging 2000 12(5):661—670.

Wang ZJ, Lian L, Chen Q, Zhao H, Asakura T, Cohen AR. 1/T2 and Magnetic Susceptibility Measurements in a Gerbil Cardiac Iron Overload Model. Radiology 2005 234(3):749-755.

Yakushiji Y, Nishiyama M, Yakushiji S, Hirotsu T, Uchino A, Nakajima J, Eriguchi M, Nanri Y, Hara M, Horikawa E, Kuroda Y. Brain microbleeds and global cognitive function in adults without neurological disorder. Stroke; a Journal of Cerebral Circulation 2008 39(12):3323-3328.

Yamada N, Imakita S, Sakuma T, Takamiya M. Intracranial calcification on gradient-echo phase image: depiction of diamagnetic susceptibility. Radiology 1996 198(1):171-178.

CHAPTER THREE

QUANTIFICATION OF ELLIPSOIDAL IRON SOURCES IN

POSTMORTEM RAT BRAIN USING PHASE IMAGES

Introduction

Iron-mediated tissue damage is implicated in neurotrauma, cerebral vascular

disease and a variety of neurodegenerative maladies (Anderson 2004; Gaasch et al., 2007;

Neema et al., 2009; Vymazal et al., 2007; Smith et al., 1997; Smith et al., 2010). Brain

microbleeds (BMB) are often present in these conditions and are assuming an increasing

clinical importance (Cordonnier et al., 2007; Greenberg et al., 2009; Igase et al., 2009;

Fazekas et al., 1999; Tong et al., 2003; Cordonnier et al., 2006; Kirsch et al., 2009;

Yakushiji et al., 2008; Sveinbjornsdottir et al., 2008). Pathologically, BMB have been

shown to be associated with hemosiderin (Fazekas et al., 1999, Tanaka et al., 1999,

Schrag et al., 2010) the iron-protein complex associated with hemorrhage (Bizzi et al.,

1990). Hemosiderin is visible in MR images due to its paramagnetic iron content and

thus serves as a marker for BMB (Atlas et al., 1988, Viswanathan and Chabriat, 2006).

Because BMB present a source of pathologic iron to the brain, the non-invasive magnetic

resonance quantification of this iron pool is potentially valuable to monitor both disease

progression and treatment efficacy (Haacke et al., 2005; Schenck and Zimmerman,

2004). Past efforts to quantify brain iron have focused on content estimation within

distributed brain regions (Haacke et al., 2005, Jara et al., 2006, Bartzokis et al., 2007,

Péran et al., 2009, Gilissen et al., 1999, Bartzokis et al., 1993, Schenck et al., 2006, House et al., 2007, Ordidge et al., 1994, Gelman et al., 1999, Vymazal et al., 2007, Neema et al., 2009, McNeill et al., 2008, Ogg et al., 1999, Haacke et al., 2007, Xu et al., 2008, Ding et al., 2009, Kirsch et al., 2010, Zhang et al., 2009, Grabner et al., 2010, Ge et al., 2007, Pfefferbaum et al., 2009, Hammond et al., 2008, Haacke et al., 2009, Eissa et al., 2009, Szumowski et al., 2010). BMB however represent a localized source of iron deposition. In addition, the use of "magnitude" images of localized iron sources is not reliable both for iron content (Dixon et al., 2009) or source size determination (Pintaske et al., 2006b, Bos et al., 2003, Schrag et al., 2010).

We recently proposed a simple method to quantify localized iron sources using phase images. The method was validated using agarose gel phantoms containing carefully prepared spherical iron samples modeled as magnetic dipoles (McAuley et al., 2010a). For small deposits in the far field, the actual geometry of the susceptibility source in not significant. However, for measurements near larger deposits the shape of the source becomes more important. In the present study, we present a putative generalization of our localized quantification technique to account for non-spherical samples and assume scalene (i.e., triaxial) ellipsoidal geometry. In addition, beyond the idealized phantom systems of the previous study, here the localized iron samples are prepared in real animal tissue. Therefore, the purpose of this study is to investigate iron quantification of localized iron sources with ellipsoidal geometry using phase images of the postmortem rat brain.

Materials and Methods

Theoretical Background and Rationale

MR voxels containing and surrounding paramagnetic (or ferromagnetic) brain iron deposits have an altered local field ΔB, and thus an altered phase with respect to their neighbors. This phase difference is detectible in GRE pulse sequences and described by the simple formula (for a right handed system):

$$\Delta\phi = -\gamma \Delta B T_E$$

[1]

where $\Delta\varphi$ is the change in phase, γ is the proton gyromagnetic ratio, and T_E is the echo time (Haacke et al., 1999). In our previous paper we proposed a method that uses phase images to determine the iron content of localized samples treated as spherical magnetic dipoles. Here we generalize to ellipsoidal source geometry and formulate expressions for ΔB and Δφ using confocal ellipsoidal coordinates. Similar to our previous report we assume the magnetic susceptibility is constant both internal (χ_i) and external (χ_e) to the iron sample and define $\Delta\chi \equiv (\chi_i - \chi_e)$. Projections of schematic triaxial ellipsoidal sources and simulated modulo-2π dipole phase patterns (projected onto the main field axis) into various coordinate planes are shown in Fig 3.1A, C, E, G, I, K, and 3.1B, D, F, H, J, L, respectively. In our previous work, phase patterns were characterized by the single r_π parameter (McAuley et al., 2010a, Robson and Hall, 2005). Here the ellipsoidal dipole phase pattern characterization is generalized to three analogous parameters: a_π, b_π, and c_π. As with r_π, these parameters are associated with π-phase wraps and thus are easily identified or derived from modulo 2π phase maps.
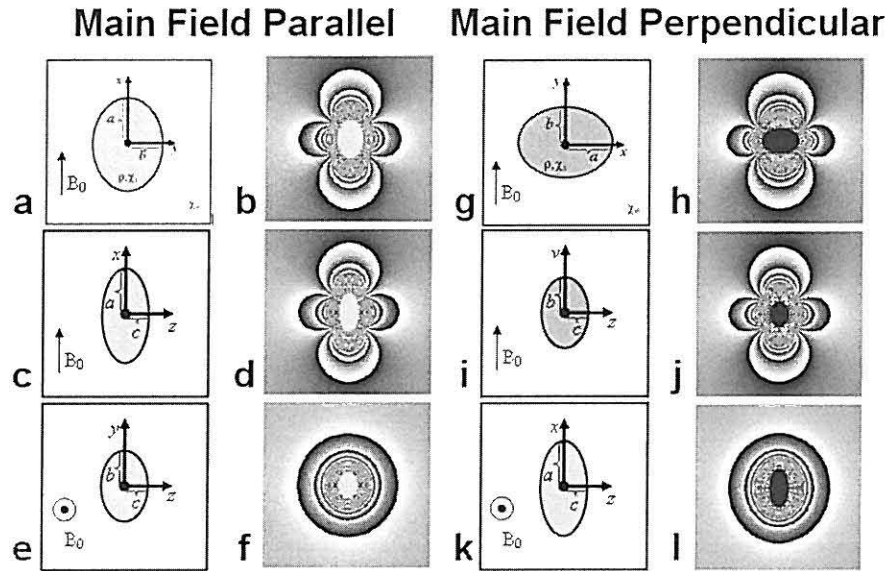
Figure 3.1: Simulated Triaxial Ellipsoidal Sources and Dipole Patterns - A, C, E, G, I, and K) Cross-sectional schematics of triaxial ellipsoidal samples with semi-axes $a > b > c$ immersed in a magnetic field B_0 that is either parallel (A, C, E) or perpendicular (G, I, K) to the major axis of the ellipsoid. Plane of projection is indicated by the axes in each panel. Samples have constant density ρ and magnetic susceptibility χ_i, and are embedded in a medium of constant susceptibility χ_c. B, D, F, H, J, L) Plane projections of simulated modulo-2π wrapped phase maps corresponding to the schematic samples in adjacent columns. Note the dipole patterns have triaxial asymmetry. Dipoles in panels B, D, H and J are oriented parallel to (and contain) the main field, whereas those in F and L are oriented perpendicular to the main field, and represent the induced field projected along the main field axis.

Ellipsoidal Coordinates

Eq. 2 is the generating equation for the ellipsoidal coordinates, where $\lambda = \xi$ = constant, $\lambda = \mu$ = constant, and $\lambda = \nu$ = constant respectively represent families of ellipsoids, hyperboloids of one sheet, and hyperboloids of two sheets, provided $0 \leq \nu^2 \leq h^2 \leq \mu^2 \leq k^2 \leq \xi^2 < \infty$ and $\xi \geq a_0$. Here, h and k are defined as $k^2 = a_0^2 - c_0^2$ and $h^2 = a_0^2 - b_0^2$ where $a_0 > b_0 > c_0$ are the semi-axes of a reference ellipsoid respectively oriented along the x, y and z axes. Thus, h and k are the focal lengths of the ellipses formed when the reference ellipsoid is projected onto the x-z and x-y planes respectively. These families of quadratic surfaces are orthogonal to each other and confocal with a reference ellipsoid.

$$\frac{x^2}{\lambda^2} + \frac{y^2}{\lambda^2 - h^2} + \frac{z^2}{\lambda^2 - k^2} = 1$$

[2]

The value of the variable $\xi = \xi_0$ completely characterizes the ellipsoid with semi-major axis ξ_0, and can be thought of as the "ellipsoidal radius". It is seen from Eq. 2 that $\xi = a_0$ specifies the reference ellipsoid, and in the limit as $\xi \rightarrow \infty$, ξ describes a sphere with radius $\xi \rightarrow r$. The relations between the Cartesian and ellipsoidal coordinates implicit in Eq. 2 are expressed in Eqs. 3 (Sten, 2006):

$$x^2 = \frac{\xi^2 \mu^2 \nu^2}{k^2 h^2}$$

$$y^2 = \frac{(\xi^2 - h^2)(\mu^2 - h^2)(h^2 - \nu^2)}{h^2(k^2 - h^2)}$$

$$z^2 = \frac{(\xi^2 - k^2)(k^2 - \mu^2)(k^2 - \nu^2)}{k^2(k^2 - h^2)}$$

[3]

Note that because each coordinate is squared in the relations of Eq. 3, there is an eight fold degeneracy when mapping (ξ, μ, ν) to (x,y,z).

The scale factors for the ellipsoidal coordinates are given in Eqs. 4 (Sten, 2006):

$$h_\xi = \sqrt{\frac{(\xi^2 - \mu^2)(\xi^2 - \nu^2)}{(\xi^2 - h^2)(\xi^2 - k^2)}}$$

$$h_\mu = \sqrt{\frac{(\xi^2 - \mu^2)(\mu^2 - \nu^2)}{(k^2 - \mu^2)(\mu^2 - h^2)}}$$

$$h_\nu = \sqrt{\frac{(\xi^2 - \nu^2)(\mu^2 - \nu^2)}{(h^2 - \nu^2)(k^2 - \nu^2)}}$$

[4]

Magnetostatic Boundary Problem

Similar to our previous report, we assume that all background phase components (e.g., magnet inhomogeneities and constant phase shifts) are completely removed and the only signal present in the phase images are perturbations due solely to the dipole source. To calculate the magnetic field perturbation and proportional phase shift due to a paramagnetic source, application of Maxwell's equations leads to a boundary value problem involving Laplace's equation. The ellipsoidal harmonics are separable solutions to the Laplace equation in ellipsoidal coordinates (Sten, 2006). Our magnetostatic boundary problem is perfectly analogous to the problem of the dielectric ellipsoid in a uniform electrostatic field solved in ellipsoidal coordinates in section 3.2 of reference (Sten, 2006). Assuming an ellipsoidal source with isotropic magnetic susceptibility $\Delta\chi$ placed in a uniform main field $\mathbf{B_0}$, we consider two cases: 1) $\mathbf{B_0}$ is parallel, or 2)

58

perpendicular to the direction vector ($\hat{a}$) of the major diameter of the reference ellipsoid (Fig. 3.1). For definiteness, we take the axis of orientation for case 2 as the y-axis. (For completeness, a third case, formally similar to case 2, where $\hat{a}$ is directed along the z-axis should be considered. We do not treat this case here, and leave it for future work). In analogy with (Sten, 2006), the magnetostatic potential outside the source for cases 1) and 2) is given by Eqs. 5 and 6 respectively, where the integral expressions are defined by Eqs. 7 -10:

$$\psi_{out} = -\left(\frac{B_0 \xi \mu \nu}{k h}\right)\left[1 - \left(\frac{a_0 b_0 c_0 \Delta X I_1^1(\xi : \infty)}{1 + \Delta X L_1^1(\xi_0)}\right)\right]$$

[5]

$$\psi_{out} = -\left(\frac{B_0 \sqrt{(\xi^2 - h^2)(\mu^2 - h^2)(h^2 - \nu^2)}}{h \sqrt{(k^2 - h^2)}}\right)\left[1 - \left(\frac{a_0 b_0 c_0 \Delta X I_1^2(\xi : \infty)}{1 + \Delta X L_1^2(\xi_0)}\right)\right]$$

[6]

$$I_1^1(\xi : \infty) = \int_\xi^\infty \frac{d\upsilon}{\upsilon^2 \sqrt{(\upsilon^2 - h^2)(\upsilon^2 - k^2)}}$$

[7]

$$I_1^2(\xi : \infty) = \int_\xi^\infty \frac{d\upsilon}{(\upsilon^2 - h^2)^{3/2}(\upsilon^2 - k^2)^{1/2}}$$

[8]

$$L_1^1(\xi_0) = a_0 b_0 c_0 I_1^1(\xi_0 : \infty)$$

[9]

$$L_1^2(\xi_0) = a_0 b_0 c_0 I_1^2(\xi_0 : \infty)$$

[10]

59

Here $\Delta\chi$ is the difference between the magnetic susceptibility of the iron samples and background tissue, and a_0, b_0 and c_0 are the semi-axes of the ellipsoidal sample. Thus the product $a_0 b_0 c_0$ can be related to the iron mass of the sample Fe by equation 11:

$$m = \frac{4\pi\rho a_0 b_0 c_0}{3}$$

[11]

where ρ is the iron density of the sample, assumed constant. Taking the negative gradient of Eqs. 5 and 6, and using the scale factors of Eq. 4, the magnetic fields in the ellipsoidal system are given by Eqs. 12 and 13 for case i) and ii) respectively:

$$\vec{B}_0(\xi,\mu,\nu) =$$

$$\left\{\left(\frac{B_0\mu\nu}{khh_\xi}\right)\left(1 - \frac{a_0 b_0 c_0 \Delta\chi\left[I_1^1(\xi:\infty)-\zeta(\xi)\right]}{1+L_1^1\Delta\chi}\right)\right\}\hat{e}_\xi +$$

$$\left\{\left(\frac{B_0\xi\nu}{khh_\mu}\right)\left(1 - \frac{a_0 b_0 c_0 \Delta\chi\, I_1^1(\xi:\infty)}{1+L_1^1\Delta\chi}\right)\right\}\hat{e}_\mu +$$

$$\left\{\left(\frac{B_0\xi\mu}{khh_\nu}\right)\left(1 - \frac{a_0 b_0 c_0 \Delta\chi\, I_1^1(\xi:\infty)}{1+L_1^1\Delta\chi}\right)\right\}\hat{e}_\nu$$

[12]

$$\vec{B}_0(\xi,\mu,\nu) =$$

$$\left\{\left(\frac{B_0\xi}{h_\xi}\right)\left(\sqrt{\frac{(\mu^2-h^2)(h^2-\nu^2)}{h^2(k^2-h^2)(\xi^2-h^2)}}\right)\left(1 - \frac{a_0 b_0 c_0 \Delta\chi\left[I_1^2(\xi:\infty)-\zeta(\xi)\right]}{1+L_1^2\Delta\chi}\right)\right\}\hat{e}_\xi +$$

$$\left\{\left(\frac{B_0\mu}{h_\mu}\right)\left(\sqrt{\frac{(\xi^2-h^2)(h^2-\nu^2)}{h^2(k^2-h^2)(\mu^2-h^2)}}\right)\left(1 - \frac{a_0 b_0 c_0 \Delta\chi\, I_1^2(\xi:\infty)}{1+L_1^2\Delta\chi}\right)\right\}\hat{e}_\mu -$$

$$\left\{\left(\frac{B_0\nu}{h_\nu}\right)\left(\sqrt{\frac{(\xi^2-h^2)(\mu^2-h^2)}{h^2(k^2-h^2)(h^2-\nu^2)}}\right)\left(1 - \frac{a_0 b_0 c_0 \Delta\chi\, I_1^2(\xi:\infty)}{1+L_1^2\Delta\chi}\right)\right\}\hat{e}_\nu$$

[13]

where

$$\zeta(\xi) = \frac{1}{\xi\sqrt{(\xi^2 - h^2)(\xi^2 - k^2)}}$$

[14]

Phase Image Parameters

Simulated modulo-2π ellipsoidal dipole phase patterns are shown in Fig 3.1B, D, F, H, J, L (in house MATLAB code, The MathWorks, Natick, MA). The triaxial asymmetry evident in the figure underscore that at least three parameters from the dipole patterns are required to characterize the phase perturbations. Three easily identified and characterized points on two image orientations are shown for Case 1 in Fig 3.2A and B denoted A', B and C (note point C is common to both simulated images). The π-phase wrapping of the axial image of Fig 3.2B forms an ellipse due to the ellipsoidal symmetry of the source. However, the horizontal image of Fig 3.2A displays cylindrical symmetry due to the linear main field $\mathbf{B_0}$. Analogous points are depicted for Case 2 in Fig 3.2C and D denoted B*, A, and C.

Case 1 ($B_0 \parallel \hat{a}$):

Using Eqs. 1, 3, 11 and 12, the phase at points A' ($\phi_{A'}$) and B (ϕ_B) can be expressed as:

$$\phi_{A'} = \left(\frac{3m\gamma\chi B_0 T_E}{4\pi\rho}\right)\left(\frac{I_1^1(a'_\pi : \infty) - \zeta(a'_\pi)}{1 + L_1^1\Delta\chi}\right) = -\pi$$

[15]

$$\phi_B = \left(\frac{3m\gamma\chi B_0 T_E}{4\pi\rho}\right)\left(\frac{I_1^1(a_\pi : \infty)}{1 + L_1^1\Delta\chi}\right) = \pi$$

[16]
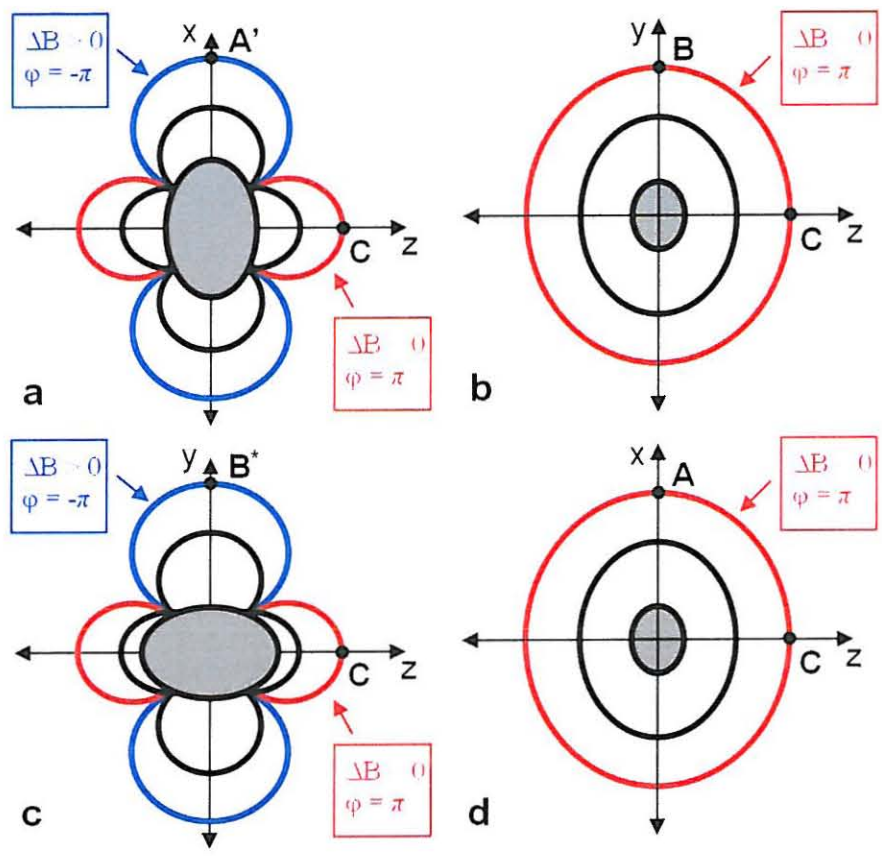
Figure 3.2: Phase Pattern Measurement Points - Schematic cross sections of triaxial dipole phase patterns from two Cases: 1) main field B_0 parallel (A and B), and 2) perpendicular (C and D) to the major axis of the ellipsoid. A) Cross section of a horizontally oriented image (Case 1). Point A' is the intersection of the main field axis with the first phase wrap. The distance from the origin to point A' is denoted a'_π. The field perturbation at this point $\Delta B > 0$, thus the phase is $\phi_{A'} = -\pi$ in the right-handed system. Point C is identical to point C in panel B and described below. B) Cross section of an axially oriented image (Case 1). The plane of this image is orthogonal to that of panel A. Points C and B occur at the intersections of the first phase wrap and the axes which respectively correspond to the smallest and second-to-smallest semi-axes of the reference ellipsoid. The distance from the origin to points B and C is denoted b_π and c_π respectively. The field perturbations at these points is equal and negative ($\Delta B < 0$), thus the phase is $\phi_B = \phi_C = \pi$. Panels C and D represent Case 2 and are analogous to panels A and B. C) Cross section of a horizontally oriented image (Case 2). Point B^* is the intersection of the main field axis and the first phase wrap located at a distance b_π from the origin. $\Delta B > 0$ and the phase at this point is $\phi_{B'} = -\pi$. Point C is identical to point C in panel D and described below. D) Cross section of axially oriented image (Case 2). Points A and C occur at the intersections of the first phase wrap and the axes which respectively correspond to the largest and smallest semi-axes of the reference ellipsoid. The distance from the origin to points A and C is denoted a_π and c_π respectively. ΔB is equal at these points and negative, thus the phase is $\phi_A = \phi_C = \pi$. Application of the triaxial quantification method requires the knowledge of a_π, b_π and c_π to evaluate the integrals of Eq. 7 and 8 (since h and k depend on these three parameters). The elliptical symmetry of the axial images allows direct measurement of two of these parameters: b_π and c_π for case 1 (panel B) and a_π and c_π (panel D). However, the elliptic cylindrical symmetry of the horizontal images does not allow a direct measurement of the third parameter. However, a_π for case 1 (b_π for case 2) can be calculated from Eq. 19 (Eqs. 20 and 24) using values of a'_π (b^*_π) measured from the image (see Fig 3.3).

Note that the points A' and B fall on the first phase-wrap and therefore have respective corresponding phases $\phi_{A'} = \pi$ and $\phi_B = -\pi$. There exist ellipsoids in the confocal system that contain these points and we denote their elliptical radii by a'_π and a_π respectively. Note that a'_π is the distance from the origin to point A' and is easily measured in the figure, whereas a_π is as yet undetermined. Using Eq. 16, we arrive at the following expression for sample iron mass:

$$m_{Fe} = \left(\frac{4\pi^2 \rho}{\gamma \Delta \chi B_0 T_E} \right) \left(\frac{1}{3 I_1^1(a_\pi : \infty)} \right)$$

[17]

(here we have safely used the approximation $1 + L\Delta\chi \approx 1$ since $0 \leq L \leq 1$ (Landau et al., 1984) and $\Delta\chi$ is on the order of several tens of parts per million for brain iron (Duyn et al., 2007)). Thus, Eq. 17 informs us that iron mass is proportional to the inverse of the integral of Eq. 7 where $\xi = a_\pi$ is the elliptical radius of the ellipsoid defined by the π-wrapping that occurs at points B and C. That is, the ellipsoid with semi-axes b_π and c_π whose cross section in the y-z plane corresponds to the π-wrapping (Fig 3.2B).

There are two apparent problems in determining the integral $I(a_\pi : \infty)$. First, in practice we do not know the actual dimensions of the iron source, therefore the reference ellipsoid with semi-axes a_0, b_0 and c_0 can not be used to determine h and k. Second, while b_π and c_π can be determined from the axial phase images (Fig 3.2B), a_π can not be directly determined from the horizontal images. To address the first problem we choose the ellipsoid defined by a_π, b_π, and c_π as the reference ellipsoid. We assume this ellipsoid is confocal to the ellipsoid defined by the source dimensions, and thus $h^2 = a_\pi^2 - b_\pi^2$ and $k^2 = a_\pi^2 - c_\pi^2$ (note that the validity of this assumption has not yet been verified (discussed

further below)). Because the polarization factors of Eq. 9 and 10 are neglected and the product $a_0b_0c_0$ is absorbed in the iron mass expression of Eq. 11, the analysis method is now independent of the source dimensions. As a solution to the second problem, we use the combined phase information at the points A' and B to determine a_π. Taking the ratio of Eqs. 15 and 16 we find:

$$I_1^1(a_\pi : x) - I_1^1(a'_\pi : x) = \zeta(a'_\pi)$$

[19]

A simple numerical technique can then be used to determine the a_π parameter implicitly defined by Eq. 19.

Case 2 ($B_0 \perp \hat{a}$):

Similar to Case 1, the points A, B* and C (with corresponding a_π, b^*_π, and c_π) in the schematic phase images of Fig 3.2C & D can be used to determined b_π. Eq. 3 can be used to define the ellipsoidal radius a^*_π for the ellipsoid corresponding to b^*_π that is confocal to the reference ellipsoid $\xi = a_\pi$:

$$a^*_\pi = \sqrt{\frac{b^{*2}_\pi k^2 + h^4}{h^2}}$$

[20]

Analogous definitions of Eqs. 15, 16, 17, and 19 for case 2 become:

$$\phi_{B'} = \left(\frac{3m\gamma X B_0 T_E}{4\pi\rho}\right)\left(\frac{I_1^2(a^*_\pi : x) - \zeta(a^*_\pi)}{1 + L_1^2 \Delta X}\right) = -\pi$$

[21]

$$\phi_C = \left(\frac{3m\gamma X B_0 T_E}{4\pi\rho}\right)\left(\frac{I_1^2(a_\pi : x)}{1 - L_1^2 \Delta X}\right) = \pi$$

[22]

65

$$m_{Fe} = \left(\frac{4 \pi^2 \rho}{\gamma \Delta \chi B_0 T_E} \right) \left(\frac{1}{3 I_1^2 (a_\pi : \infty)} \right)$$

[23]

$$I_1^2 (a_\pi : \infty) + I_1^2 (a_\pi^* : \infty) = \zeta(a_\pi^*)$$

[24a]

$$I_1^2 (a_\pi : \infty) - I_1^2 (a_\pi^* : \infty) = \zeta(a_\pi^*)$$

[24b]

While Eq. 24a is derived analogously to Eq. 19, contrary to Eq. 19, Eq. 24a is not consistent with simulation data and a_π values could not be determined. However, it was observed that a_π values could be calculated using a sign change according to Eq. 24b, and this data seemed to give reasonably accurate results compared to theoretical expectations (eg, linear curves). Additional simulations however showed unexpected results (discussed below). Therefore, explanations regarding the validity of Eq. 24b and/or other assumptions of our method, especially with regard to Case 2, are required before the triaxial technique can be validated. Possible sources of these discrepancies in under investigation and discussed below. In any case, for now, we assume that Eq. 24b is correct, use it in our analysis method below, and consider our results tentative.

A critical facet of Eqs. 17 and 23 is that they share the same proportionality constant. Therefore, in theory plots of m_{Fe} and *both* $1/I_{1,1}(a_\pi:\infty)$ and $1/I_{1,2}(a_\pi:\infty)$ can be displayed on the same axes to build a standard curve. We will use the notation $I(\xi:\infty)$ to refer to either integral as appropriate. In addition, we also adopt the following generalized notation for the image parameters: $\alpha'_\pi \equiv a'_\pi$ or b^*_π, for the parameters along the main field axis; $v_\pi \equiv a_\pi$ or b_π for parameters on the vertical axis of the axial images, and $h_\pi \equiv c_\pi$ the parameter on the horizontal axis of the axial images.

66

In summary, application of the proposed quantification method for scalene ellipsoidal sources consists of the following requirements and steps: 1) Eqs. 17 and 23 describe the inversely proportional relationship between sample iron mass and the integrals of Eqs. 7 and 8 for the parallel (Case 1) and transverse (Case 2) cases respectively. Therefore, evaluation of the integrals is required. 2) Integral evaluation requires the knowledge of the ellipsoidal radius a_π, as well as the ellipsoidal phase pattern semi-axes b_π and c_π. 3) For the parallel (transverse) case b_π and c_π (a_π and c_π) can be determined by the axial phase images (Fig 3.1F, L, Fig 3.2B, D, Fig 3.4, H, J). However, a_π (b_π) must be determined indirectly from a'_π (b^*_π) measured in the horizontal images (Fig 3.1D, J, Fig 3.2A, C, Fig 3.4D, I) using Eq. 19 (Eqs. 20 and 24b) for the parallel (transverse) case to numerically solve for a_π (b_π). It should be noted that to date, these steps are tentatively defined and await further theoretical and experimental verification.

In the special case of a sphere where $h = k = 0$ and $a_\pi = b_\pi = c_\pi = r_\pi$, the integral becomes $1/3\ r_\pi^3$ and Eqs. 17 and 23 both reduce to the same equation reported in our previous paper for spherical samples (Eq. 5 of (McAuley et al., 2010a)):

$$m_{Fe} = \left(\frac{4\pi^2 \rho}{\gamma' \Delta X B_0 T_E} \right) r_\pi^3$$

[25]

Similar analogies with the equations and their implications of the previous paper (McAuley et al., 2010a) can be deduced by substitution of r_π^3 with $[3I(a_\pi;\infty)]^{-1}$ and a^3 with $a_0 b_0 c_0$. In analogy to Eq. 7 of (McAuley et al., 2010a) the combination of Eqs. 11 and 17 lead to:

$$a_0 b_0 c_0 = \left(\frac{\pi}{\gamma' \Delta X B_o T_E} \right) \left(\frac{1}{I(a_\pi : \infty)} \right)$$

[26]

Eq. 26 reveals that the actual volume of an ellipsoidal source can potentially be determined from phase images unhindered by the familiar blooming effect of GRE magnitude images. Eq. 27 is analogous to Eq. 8 of (McAuley et al., 2010a) and for a given $\Delta\chi$, describes the conversion of $I(a_\pi : \infty)$ between field strengths and echo times:

$$\frac{I(a_\pi : \infty)_1}{I(a_\pi : \infty)_2} = \frac{B_{0_2} T_{E_2}}{B_{0_1} T_{E_1}}$$

[27]

Finally, for a spherical source, it follows from Eqs. 1, 2 and 5 of reference (McAuley et al., 2010a) that

$$\alpha'_\pi \equiv a'_\pi = b^*_\pi = 2^{1/3} r_\pi$$

[28]

Thus, replacement of $1/I$ with α'^3_π in Eq. 25 amounts to an assumption of spherical geometry and ignores triaxial effects. (The larger dynamic range of α'_π in a pixilated environment confers an advantage over r_π).

The rationale to validate the method of the present paper is similar to our previous work: Eqs. 17 and 23 amount to mathematical hypotheses that predict inversely proportional relationships between parallel or transverse integrals of the dipole phase pattern parameter a_π and sample iron mass. Therefore, simple plots of these variables can be used to verify the predictions of the hypotheses and thus validate the method. In addition, comparison with plots using α'_π allow appraisal of the differential effects of triaxial versus spherical geometry.

Computer Simulations

Dipole phase patterns due to triaxial iron sources were simulated using in house MATLAB code (The MathWorks, Natick, MA) using Eqs. 1, 3, 4, 7-10, 12-14. Source semi-axes such that $a_0 > b_0 > c_0$ were chosen with the aid of a peudo-random number generator. Simulations were performed for each of two cases: $B_0 \perp \hat{a}$ (Case 1) or $B_0 \parallel \hat{a}$ (Case 2) using the following parameters: $B_0 = 11.7T$, 384x384 matrix, 0.086x0.086mm in-plane resolution, T_E 20 ms, and $\Delta\chi = 20$ppm. The resulting simulated images were similar to Fig 3.1B, F, H and L. Bounding rectangles were drawn around simulated horizontal and axial dipole cross sections in the same way as shown (for real data) in Fig 3.4I and J (McAuley et al., 2010b). The parameters a_π, b_π, and c_π were determined as follows: Case 1: a'_π, b_π, and c_π were measured from bounding rectangles, and a_π was calculated using Eq. 19. Case 2: a_π, b^*_π, and c_π were measured from bounding rectangles, a^*_π was calculated using Eq. 20, and b_π was determined from Eq. 24b. Eq. 7 or 8 was then used to calculate $I_{1,1}(a_\pi;\infty)$ or $I_{1,2}(a_\pi;\infty)$ for Case 1 and Case 2, respectively. The source volume $(4\pi/3)a_0 b_0 c_0$ for all simulations was plotted against $[I(a_\pi;\infty)]^{-1}$. In addition, $(4\pi/3)a_0 b_0 c_0$ was also plotted versus α'_π to compare with spherical geometric assumptions. An additional set of similar simulations was carried out using manually chosen dimensions to test how the triaxial method performed when samples had the same volume but different geometry (i.e., different semi-axes lengths).

Iron Sample Preparation

As described in our previous study, we used a chitosan-ferric oxyhydroxide composite material (Ch-Fe) to create iron samples of known concentration (McAuley et al., 2010a, Sipos et al., 2003). The material serves as a mimic for hemosiderin (McAuley

et al., 2010a) which is formed in lysosomes and is not commercially available. Hemosiderin is the iron-protein complex associated with pathological iron storage following hemorrhage (Bizzi et al., 1990) and ferritin breakdown (Schenck and Zimmerman, 2004). It is visible in MR images due to its paramagnetic iron content and thus serves as a marker for BMB (Atlas et al., 1988; Viswanathan and Chabriat, 2006).

An aqueous solution of Ch-Fe was prepared and microliter volumes of the solution were injected into the rat brain as described below. The iron concentration of the Ch-Fe material was determined by graphite furnace atomic absorption spectrometry (Varian, Inc., Palo Alto, CA) therefore the injections contained a known amount of iron.

Rat Brain Ch-Fe Injections

Our animal protocol was approved by the Loma Linda University Institutional Animal Care and Use Committee. To remove the blood from cerebral vessels, 12 Sprague-Dawley rats (225-400 g) were sacrificed by transcardial perfusion with PBS. The rats were decapitated, the skull uncovered, and the heads were placed in a stereotatic frame (Kopf Instruments, Tujunga, CA). A small burr hole (~1mm) was drilled into the skull 0.5mm anterior and 3.1mm lateral from bregma. Microliter quantities (0.5, 1.0, 1.25, 1.5, 2.0, 2.5, 3.0, 3.5 and 4.0) of Ch-Fe solution of known iron concentration were injected 5.2mm below the skull surface using a Hamilton syringe (Reno, NV). Each sample was injected over 5 min controlled by a microsyringe pump (World Precision Instruments, Sarasota, FL). The chosen stereotactic coordinates target the caudate/putamen of the rat brain. To minimize, bleeding of Ch-Fe up the needle tract, following the injections, the needle was held in place for at least 10 minutes and then slowly withdrawn at approximately 0.5mm/min. Fourteen samples were injected into 12

rats (two rats received bilateral injections). Surrounding tissue was then removed and the skulls were fixed in 4% buffered paraformaldehyde for at least 24 hours. Following fixation, brains were removed from the skull and embedded in 2% degassed agarose gel within plastic scintillation tubes.

Magnetic Resonance Imaging

Susceptibility weighted imaging (SWI) is a GRE sequence that uses magnetic susceptibility-dependent complex phase information to provide or enhance image contrast (Haacke et al., 2004; Reichenbach et al., 1997a) and is very sensitive in BMB detection (Tong et al., 2003; Akter et al., 2007). We used two SWI sequences for this study: a 3D SWI horizontal sequence, and a 2D axial sequence. The 2D sequence was used because of 3D axial scans had significant background phase apparently due to inadequate magnetic shimming. The 2D sequences did not have this problem and therefore were chosen in place of a 3D axial scan.

The rat brains were scanned in an 11.7T small vertical-bore MR scanner (Bruker Biospin, Billerica MA) using the following parameters : 1): 3D horizontal sequence: TR/TE: 100/7 ms, flip angle: 20°, matrix: 256 x 256, NEX: 1, FOV: 2.2 cm, in-plane resolution: 85.9 μm x 85.9 μm, and 32 slices of thickness 688 μm. 2) a 2D SWI axial sequence: TR/TE: 154.4/7 ms, flip angle: 20°, matrix: 256 x 256, NEX: 4, FOV: 2.2 cm, in-plane resolution: 85.9 μm x 85.9 μm slices: 10-40 of thickness 688 μm.

Image and Data Processing

As in our previous report (McAuley et al., 2010a), raw phase images were high-pass filtered (HP) using a frequency domain filter (SPIN software, MRI Institute, Detroit,

MI) (Wang et al., 2000). 16x32 or 32x32 kernel sizes were empirically chosen for 3D horizontal and 2D axial image respectively. These filter sizes typically resulted in isolated dipoles with good symmetry and little distortion. Magnitude images were multiplied four times by the product of a positive and a negative phase masks created from the HP images (Haacke et al., 2004).

The image parameters a'_π, b_π, and c_π, (Case 1), or $b*_\pi$, a_π, and c_π (Case 2) were determined from the dimensions of rectangles bounding the π-phase wrap of dipole patterns in the filtered phase images using ImageJ software (ImageJ, NIH) (McAuley et al., 2010b). The width and height of the rectangle in pixels was divided by two and multiplied by the appropriate pixel dimension to give the lengths of the parameters (Fig 3.4I and J). In house code (MATLAB, The MathWorks, Natick, MA) was used to solve for a_π (b_π) that is implicitly defined by Eq. 19 (Eq. 24b). The method is depicted graphically in Fig 3.3. A necessary, but not sufficient condition for a parallel orientation (ie, Case 1) is: $a'_\pi / v_\pi \geq 2^{1/3} \approx 1.26$. Therefore, dipoles that do not meet this criterion are assumed to have a transverse geometry (Case 2) and analyzed based on Eq. 24b. However, for dipoles that do meet this criterion, a transverse solution is still possible; therefore such dipoles are processed for both orientations. The ambiguity associated with this case is discussed below.

Statistical and Sensitivity Analysis

The predicted relationships between the mass of iron m_{Fe} (injected Ch-Fe samples) and volume $V = (4\pi/3)a_0 b_0 c_0$ (simulations) versus $1/I$ were tested by linear regression analysis using SigmaPlot version 11 (Systat Software, Inc., Chicago, IL). Plots of m_{Fe} vs. $1/I$ and

V vs. $1/I$ were constructed along with best-fit least squares regression lines. Statistical significance was considered at $p < 0.05$. Plots of m_{Fe} and V vs. $a'_\pi{}^3$ and $b*_\pi{}^3$ alone were also constructed so that the effects of source geometry can be compared (i.e., the generalized triaxial ellipsoidal geometry versus the special case of spherical symmetry).

Sample 10: Case 1 (Assumed Parallel)

Sample 9: Case 1 (Assumed Parallel)

Sample 9: Case 2 (Assumed Perpendicular)
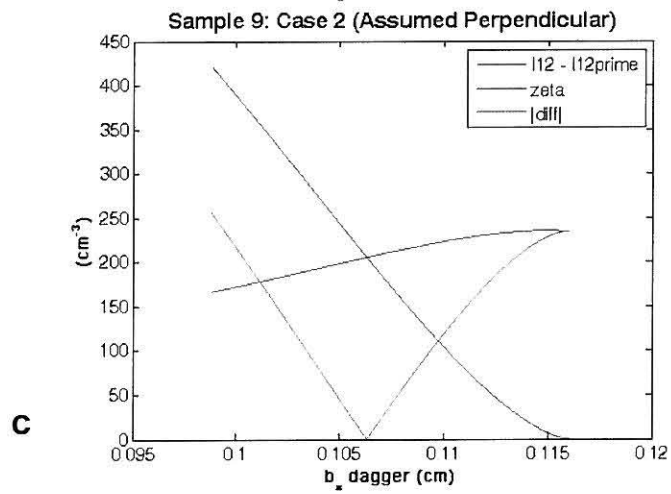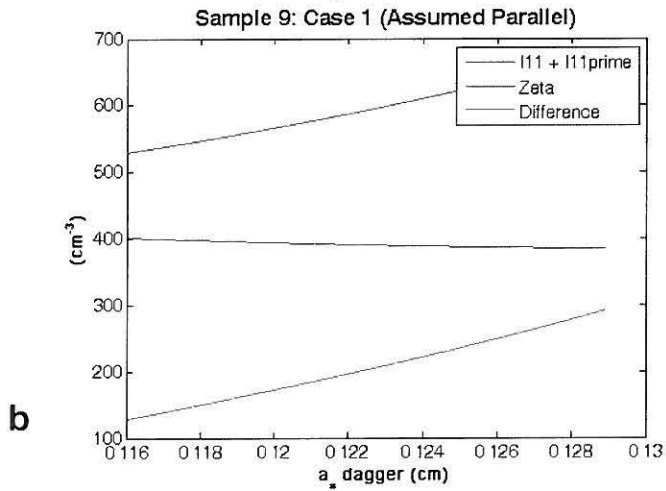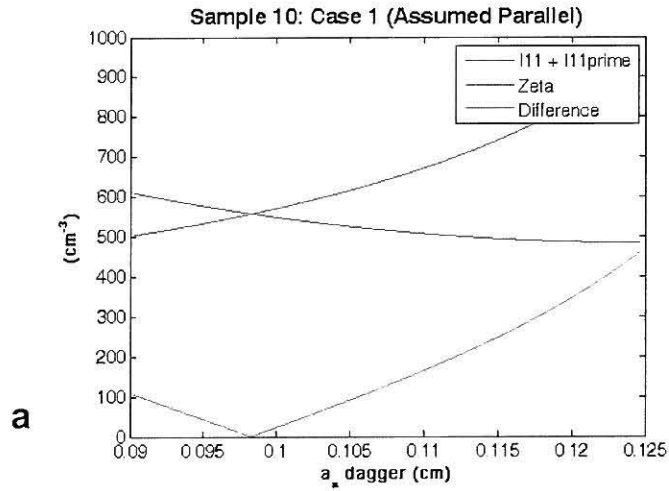
Fig 3.3: $I(a_\pi:\infty)\pm I(a'_\pi:\infty)$ **vs.** $\zeta(a_\pi)$ - A graphical illustration of the numerical method employed to find $a_\pi (b_\pi)$ from $a'_\pi (b*_\pi)$ measured in the horizontal images using Eq. 19 (Eqs. 20 and 24b). The method is applied to two Ch-Fe samples: sample 10 in (see Table 3.1) panel A, and sample 9 in panels B and C. A) Case 1 for sample 10: $I_{1,1}(a_\pi:\infty) + I_{1,1}(a'_\pi:\infty)$, $\zeta(a'_\pi)$, and $|I_{1,1}(a_\pi:\infty) + I_{1,1}(a'_\pi:\infty) - \zeta(a'_\pi)|$ are plotted against the putative $a^\dagger_\pi$ where $b_\pi \le a^\dagger_\pi \le a'_\pi$. The chosen a_π (0.98 cm) is the point on the abscissa corresponding to the intersection of $I_{1,1}(a_\pi:\infty) + I_{1,1}(a'_\pi:\infty)$ and $\zeta(a'_\pi)$ as well as the negligibly small value of $|I_{1,1}(a_\pi:\infty) + I_{1,1}(a'_\pi:\infty) - \zeta(a'_\pi)|$. B) Case 1 for sample 9: $I_{1,1}(a_\pi:\infty) + I_{1,1}(a'_\pi:\infty)$ and $\zeta(a'_\pi)$ do not cross in this plot. The apparent convergence (divergence) of these two curves as a_π approaches $b_\pi (a'_\pi)$ from the right (left) is consistent with an a_π value $< b_\pi$ implying that the assumed orientation of the source to the field is not correct. In other words, the field is not parallel to the major axis of the source but orthogonal to it. C) Case 2 for sample 9 assumes the transverse field orientation. The two curves $I_{1,2}(a_\pi:\infty) - I_{1,2}(a'_\pi:\infty)$ and $\zeta(a'_\pi)$ intersect, and $|I_{1,2}(a_\pi:\infty) - I_{1,1}(a'_\pi:\infty) - \zeta(a'_\pi)|$ takes on a negligibly small value at when $b_\pi = b^\dagger_\pi = 1.06$ mm where $c_\pi \le b^\dagger_\pi \le a_\pi$.

75
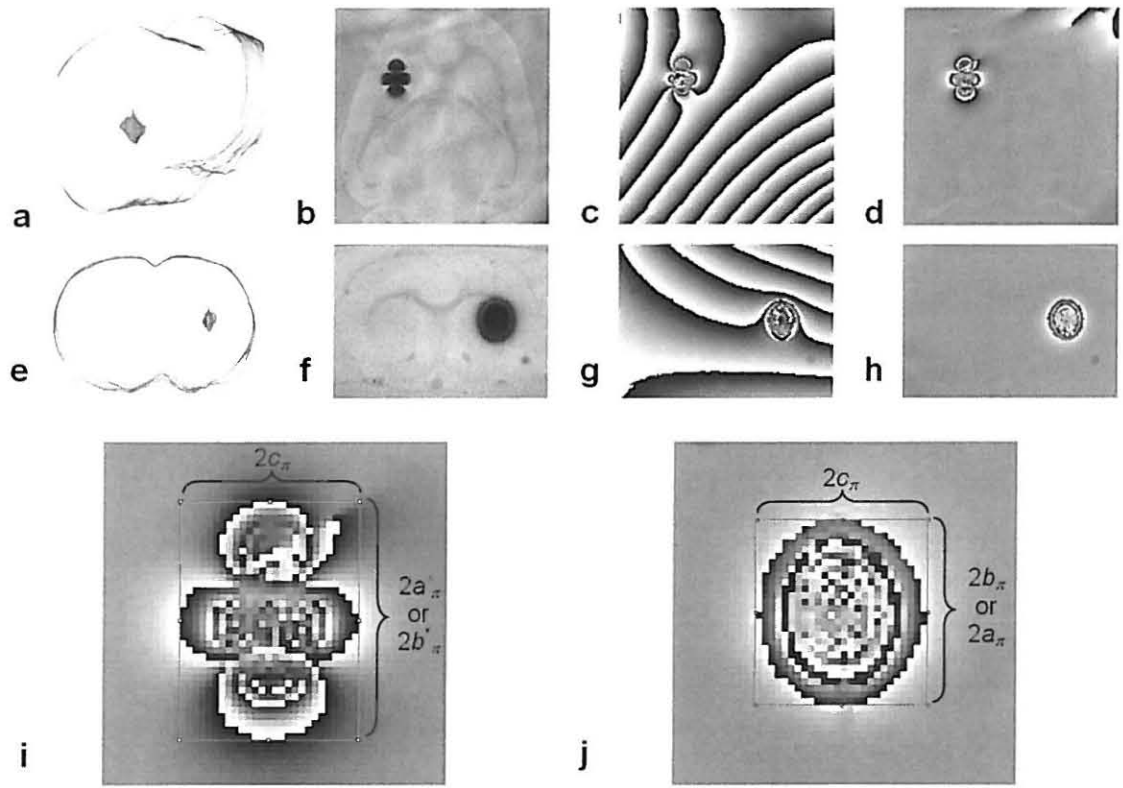
Fig 3.4: Postmortem Rat Brain Ch-Fe Injection Image Results A) Three dimensional (3D) reconstruction, B) magnitude, C) raw phase, and D) high pass-filtered SWI horizontal images of a Ch-Fe sample (sample 7 Table 3.1) in the caudate/putamen of postmortem rat brain. E) 3D reconstruction, F) magnitude, G) raw phase, and H) high pass-filtered axial SWI images for the same Ch-Fe sample and brain of panels A –D. The 3D reconstructions are based on T_2 image data (not shown). Note the asymmetric shape of the sample and the elliptic cross sections F-H. Magnifications of the dipole patterns from panels D and H are shown in I) and J) respectively. Note the similarity with the simulated dipoles of Fig 3.1. Also shown in panels I and J are the bounding rectangles used to measure the image parameters a_π, b_π, c_π, a'_π, b^*_π. The rectangle in panel I is used to measure a'_π for case 1 orientation, or b'_π for case 2 orientation. The rectangle in panel J is used to measure b_π and c_π for case 1 orientation, or a_π and c_π for case 2 orientation.

Results

Simulations

Fig 3.5A shows a plot of source volume $V = (4\pi/3)a_0b_0c_0$ vs. $[I(a_\pi: \infty)]^{-1}$ for the

simulation data. The graph displays a strong linear relationship ($R^2 = 0.997$, $p < 0.001$)

with a non-significant y-intercept ($-5.88e^{-05}$, $p = 0.825$). The observed proportional

relationship is predicted by Eqs. 17 and 23, and would seem to provide verification of the

ellipsoidal method and underlying theory at least in idealized (simulated) dipole phase

images. However, Fig 3.6 shows similar simulations of ellipsoidal sources of the same

volume but with differing semi-axis lengths. In Fig 3.6A, Case 1 points with volumes ~

0.015 µl tightly overlap suggesting that the method adequately accounts for the differing

geometry. However, in Case 2 (Fig 3.6B) points with this volume appear more spread

out. The discrepancy between the cases raises the question of the validity of the Case 2

application of the method in general and the role of the questionable Eq. 24b in specific

(discussed below). In any case, at this point, conclusions about the validity of the

ellipsoidal method based on Fig 3.6A remain tentative especially for Case 2 applications.

Fig 3.5B, C and D show plots of V vs. a'^3_π, v^3_π and h^3_π respectively. The use of

these single parameters can be interpreted as an assumption of spherical geometry. All

three plots show strong linear relationships ($R^2 = 0.995$, $p < 0.001$; $R^2 = 0.979$, $p < 0.001$;

$R^2 = 0.995$, $p < 0.001$; for V vs. a'^3_π, v^3_π, respectively) and two show non-significant

intercepts ($-1.78e^{-04}$, $p = 0.598$; $-1.50e^{-04}$, $p = 0.833$; for V vs. a'^3_π, and v^3_π, respectively)

as predicted by theory. The intercept of the V vs. h^3_π, although small is statistically

significant under linear regression analysis ($1.41e^{-03}$, $p < 0.001$). It is surprising that

although some data points appear to be appropriated corrected by taking the ellipsoidal

78

geometry into account, overall the linear relationship is essentially the same under the relaxed assumptions. It appears that the details of the geometry are not that important in the present context. If the slope of V vs. $[I(a_\pi: \infty)]^{-1}$ (Fig 3.5A) is taken as the 'true' slope, the unit-less slopes of V vs. α'_π, v_π and h_π are predicted by Eqs. 17, 23 and 25 to be 0.0161 (2.2 % error), 0.0321 (3.1 % error), and 0.0321 (0.94 % error), respectively. Because of the non zero intercept of the h_π^3 plot and the greater dynamic range of α'_π, it appears that a spherical assumption and the measurement of α'_π may be sufficient to quantify iron in real BMB data, without extra assumptions and complications associated with a triaxial assessment. This is a very significant result.

Rat Brain Injection Data

Four Ch-Fe samples were not analyzed because of significant dissection of Ch-Fe solution out the caudate/putamen and 10 samples in 10 rat brains were analyzed. Magnitude, phase, and high-pass filtered phase images for Ch-Fe sample 7 are shown in Fig 3.4. Samples showed robust dipole patterns in the horizontal magnitude, raw phase, and high pass-filtered images (Fig 3.4B-D, I) (Bos et al., 2003; Kim et al., 1993; Pintaske et al., 2006b). In addition, the expected equatorial dipole patterns in the axial images were also seen as concentric elliptical phase wraps in the filtered phase images (Fig 3.4F-H, J). High-pass filtered images of both orientations exhibited dipole patterns with clearly visible phase wraps surrounded by a largely homogenous background (Fig 3.4C, G, I, J). Three dimensional reconstructions based on T_2 image data (not shown) of the same sample are shown in Fig 3.4A and E. The sample clearly has a complicated
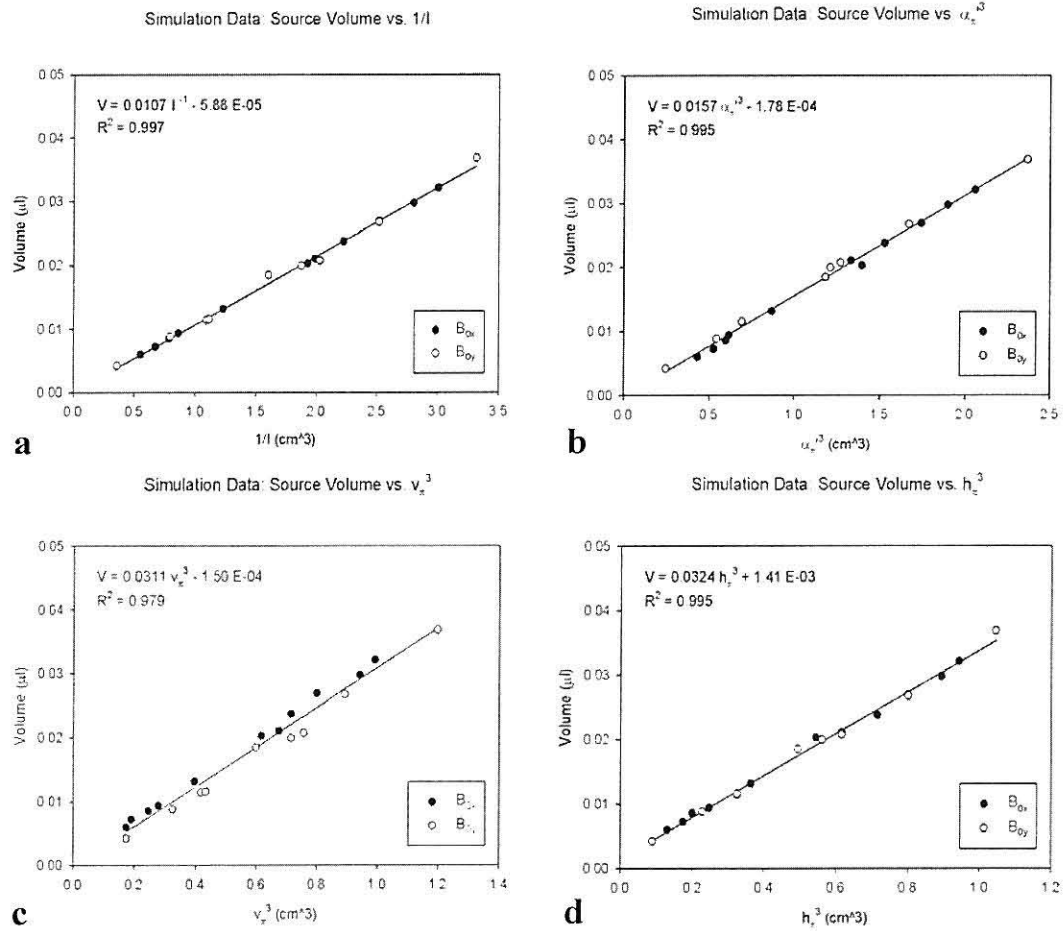
Fig 3.5: Simulated Triaxial Ellipsoid and Spherical Quantification Methods - The proposed triaxial ellipsoidal method, and for comparison, methods that assume spherical geometry were applied to simulated dipoles. Source volume (proportional to iron mass) is plotted against A) $I(a_\pi,\infty)^{-1}$, B) α'^3_π, C) v^3_π, and D) h^3_π. The inversely proportional relationship seen in panel A is predicted by the equations underlying the triaxial method (Eqs. 17 and 23). However, the plots in panels B –D also show strong proportional relationships and suggest that the additional assumptions and complexity associated with the triaxial method may not offer significant advantages over the simple spherical techniques at least in the present context.

80

Simulation Data: Case 1

$y = 0.0107x + 9E-05$
$R^2 = 0.9997$

Volume (ul) vs $1 / l_{11} (cm^3)$

Simulation Data: Case 2

$y = 0.0105x + 0.0005$
$R^2 = 0.9892$

Volume (ul) vs $1 / l_{12} (cm^3)$
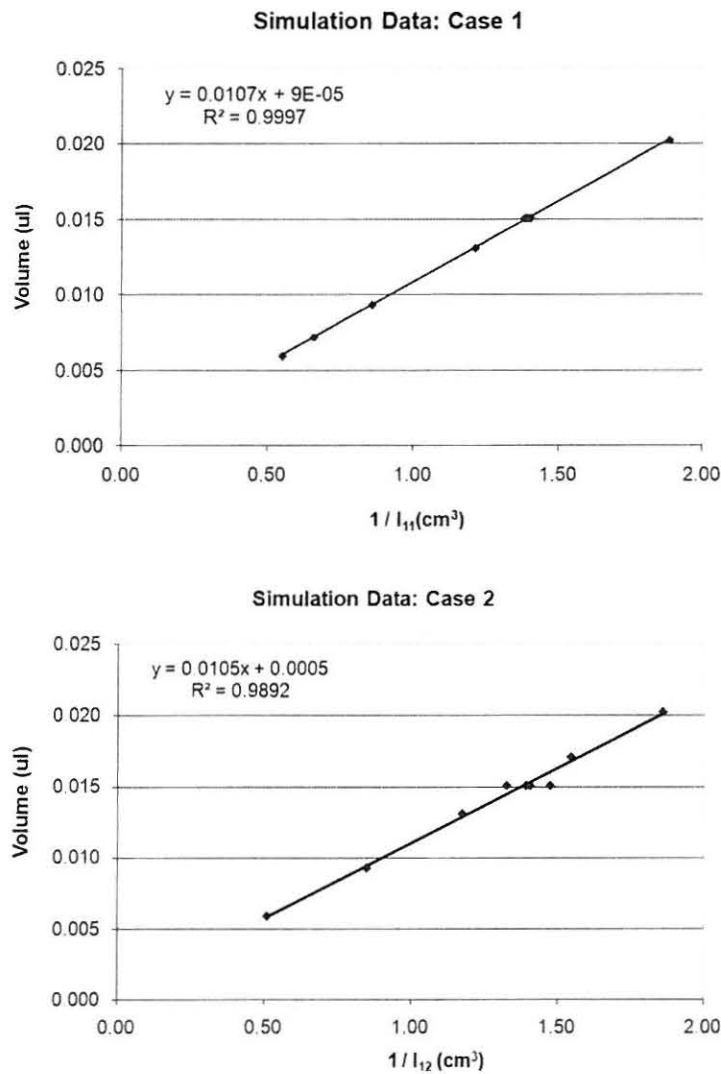
Figure 3.6: Simulation Data with Constant Volume/Differing Dimension Sources – As in Fig 3.5A the triaxial method was applied to simulated dipoles including samples that have the same volume but different dimensions (i.e., differing semi-axis lengths). A) Case 1, and B) Case 2 application of the method. Note that in Case 1, points with volumes ~ 0.015 µl tightly overlap suggesting that the method adequately accounts for the differing geometry. However, in Case 2, points with this volume appear more spread out suggesting an inferior separation of iron mass and geometry and raising questions about the soundness of Eq. 24b and the method in general, particularly when applied to Case 2.

81

asymmetrical shape. However, taken together horizontal and axial dipole patterns show a triaxial symmetry. In particular, the elliptic cross section seen in the axial image of Fig 3.4H and J, recommend an ellipsoidal analysis approach.

Iron mass, sample volume, α'_π, α_π, v_π, h_π, and δm_{Fe} values for the 10 Ch-Fe samples are shown in Table 3.1. Data for sample 7 is reported assuming both a parallel and transverse orientation. For this sample $\alpha'_\pi/v_\pi = 1.29$ implying that a case 1 (parallel) orientation was possible. However, this sample also had a case 2 (transverse) solution. T_2 data for this sample (not shown) revealed that the transverse orientation was correct and the corresponding data is used in all future analysis. Sample iron mass vs. $1/I$ is plotted in Fig 3.7A, and exhibits a strong linear relationship ($R^2 = 0.968$, $p < 0.001$) between variables with a slope of 699 μg/cm^3 ($p < 0.001$) and vanishing y-intercept value (-1.24 μg, statistically indifferent from zero, $p = 0.519$). Thus, the plot displays the inversely proportional relationship by Eqs. 17 and 23. However, similar to the simulation data, the additional plots of iron mass plotted against α'^3_π, v^3_π, and h^3_π (Fig 3.7B - D) are also strongly linear. In particular, the plot in panel B shows that α'^3_π predicts sample iron mass slightly better than does $I(a_\pi,\infty)^{-1}$ ($R^2 = 0.979$, $p < 0.001$) although the intercept of 0.454 μg is statistically different from zero (p = 0.006). The methods depicted in the latter three plots ignore the triaxial asymmetry of the dipole phase patterns and therefore in essence are spherical methods. Thus, as anticipated from the simulation data, satisfactory quantification of localized iron sources appears possible using the simpler α'_π standard curves at least in the present experimental context.

Table 3.1: Ch-Fe Injection Data: Iron mass and image parameter data for 10 Ch-Fe samples injected in the caudate/putamen of the postmortem rat brain. Eight of the ten samples are interpreted as ellipsoids with major semi-axes perpendicular to the main MRI field magnet (Case 2). Two samples (samples 7|| and10) assume an orientation with the major semi-axis parallel to the field (Case 1). Sample 7 is shown interpreted in both orientations.

Sample	m_{Fe} (µg)	α'_π (cm)	α_π (cm)	v_π (cm)	h_π (cm)	$1/l$ (cm^3)
1	0.798	0.0859	0.0848	0.0945	0.0688	0.0017
2	1.596	0.1031	0.0902	0.0902	0.0902	0.0022
3	4.788	0.1762	0.1272	0.1461	0.1203	0.0065
4	3.192	0.1504	0.1148	0.1289	0.1074	0.0047
5	0.798	0.0945	0.0773	0.0773	0.0773	0.0014
6	1.596	0.1074	0.0922	0.0945	0.0902	0.0024
7||[a,c]	3.192	0.1547	0.1224	0.1203	0.1160	0.0053
7⊥[b]	3.192	0.1547	0.1174	0.1203	0.1160	0.0049
8	3.990	0.1633	0.1264	0.1375	0.1203	0.0062
9	2.394	0.1289	0.1063	0.1160	0.0988	0.0036
10[c]	1.995	0.1246	0.0983	0.0902	0.0945	0.0026

[a]Sample 7 interpreted with the major ellipsoidal axis parallel to B_0
[b]Sample 7 interpreted with the major ellipsoidal axis perpendicular to B_0
[c]Samples 7|| and 10 are calculated assuming the major ellipsoidal axis is parallel to B_0
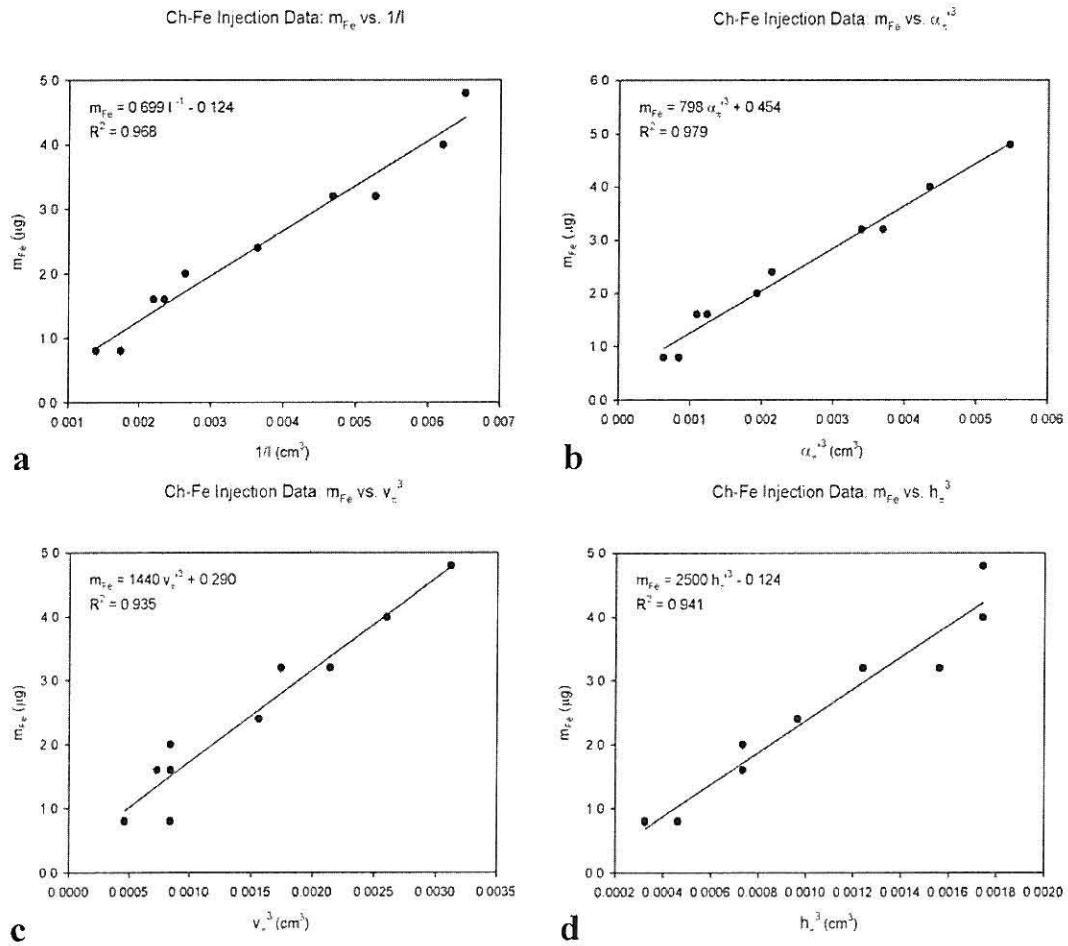
Fig 3.7: Triaxial Ellipsoidal and Spherical Methods – Postmortem Rat Ch-Fe Injection Data - The iron mass (m_{Fe}) of ten Ch-Fe samples injected into the postmortem rat brain is plotted against A) $I(a_\pi,\infty)^{-1}$, B) α'^3_π, C) v^3_π, and D) h^3_π. The strong linear relationship ($R^2 = 0.968$, $p < 0.001$) and vanishing y-intercept (-1.24 µg, statistically indifferent from zero, $p = 0.519$) in panel A is predicted by Eqs. 17 and 23. The slope of the graph is 699 µg/cm^3 ($p < 0.001$). However, similar to the simulation data (Fig 3.5) the methods that assume spherical symmetry are also stronger linear. In particular, the plot in panel B shows that α'^3_π predicts sample iron mass slightly better than does $I(a_\pi,\infty)^{-1}$ ($R^2 = 0.979$, $p < 0.001$) although the intercept of 0.454 µg is statistically different from zero (p = 0.006).

Discussion

The purpose of the present study was to investigate iron quantification of localized iron sources of ellipsoidal geometry in animal tissue using phase images. Plots of measurements from real and simulated phase images of non-spherical localized iron deposits display the expected linear relationships necessary for validation of our triaxial method. However, the Case 2 application of the method to simulated ellipsoidal sources of constant volume but differing dimensions (Fig 3.5B) suggest that these plots are not sufficient to validate the method as it stands. However, Case 1 results do not appear to show weaknesses suggesting that certain features of the method are likely robust. Two areas that may explain the questionable data of Case 2 include Eq. 24b, and the assumption that $h\,(k)$ is identical whether calculated from a_0 and b_0 (a_0 and c_0) or a_π and b_π (a_π and c_π), respectively.

A somewhat unexpected but highly significant finding was that in both the simulation and experimental data, strongly linear relationships were observed using the cube of a single dipole phase image parameter (Fig 3.5B – D, 3.7B – D). The single geometric parameter can be interpreted as an effective radius, therefore the single parameter methods are in essence spherical methods. The fact that a simple spherical method is effective in millimeter sized iron deposits has important implications for BMB quantification as discussed below.

This experiment seeks to extend the application of localized phase methods beyond spherical sample geometry to ellipsoidal geometries. In addition, the triaxial method here is a general method that handles spherical (h = k = 0), prolate spheroidal (h = k ≠ 0), and oblate spheroidal (h = 0, k ≠ 0) as special cases. That the triaxial method is

85

applicable even beyond smooth scalene source geometry can be seen from Fig 3.4. The irregular geometry of Fig 3.4A and E becomes smoothed out to the clover leaf pattern in the horizontal images (Fig 3.4D, I) and the "concentric" ellipses in the axial image (Fig 3.4H, J). While bulk non-spherical features may still be important at this level, much of the geometric details are apparently not.

a_π, b_π, and c_π represent a generalization from the r_π parameter of spherical or cylindrical sources (Robson and Hall, 2005, McAuley et al., 2010a) and like r_π are easily and robustly identified in phase wrapped images because of their association with the prominent π-phase wrap. The general applicability to the above geometries and robust identification in noisy images suggest the triaxial ellipsoidal could potentially be used in automated detection (count) and quantification schemes. Such methods could be designed as extensions to work similar to (Mills et al., 2008) who used the dipole template to identify dipole impressions in phantoms and magnetic particle labeled rat heart (Mills et al., 2008). Scaled dipole templates (ie, parameterize by a_π, etc.) could in principle be correlated in axial and horizontal images to provide information on source geometry and iron content (however, see below for challenging limitations).

BMB are associated with both chronic and emergency conditions of significant social and economic impact, especially in light of our aging population (discussed in McAuley et al., 2010b). Because BMB present a source of pathologic iron to the brain proportional to extravasated blood, the quantified iron content of BMB is potentially a valuable biomarker for disease progression, treatment efficacy and risk factor assessment (Schenck & Zimmerman 2004, Haacke et al., 2005, Greenberg et al., 2009). Associations between BMB and disease states and severity, as well as diagnostic guidelines have been

described by BMB count thresholds (Knudsen 2001, Soo et al., 2008, Sanneke 2009, Kirsch et al., 2010). Whether in single bleeds or in whole regions affected by microvascular disease, knowledge of lesion iron content as a continuous variable might enhance or hold advantage over interpretations based on discrete BMB number (McAuley et al., 2010b). However, technical hurdles must be addressed before such iron data can be acquired on clinical scanners (McAuley et al., 2010b) and further studies needed to assess the benefits of such information in diagnostic and prognostic criteria and recommendations regarding treatment. Such issues are discussed in Chapter 4, 6 and (McAuley et al., 2010b).

The advantages of a phase image approach for quantification of iron compared to magnitude image was discussed in our previous paper (McAuley et al., 2010a). In addition, most brain iron quantification efforts have involved brain regions (e.g., anatomic structures) whereas BMB are localized areas of iron deposition. In our previous work we introduced a phase image iron quantification method for localized iron sources in a phantom system (McAuley et al., 2010a). In the present work, we extend this beyond idealized spherical samples embedded in agarose gel, to asymmetric iron deposits in animal tissue (Fig 3.4). However, in addition we report here that an approach based on the single α'_{π} parameter appears to as effective as the more complex triaxial method in producing a standard curve of our simulation and experimental. Therefore, it appears that under our experimental conditions a far field effect renders the magnitude of susceptibility (iron in our case) more important than the geometric details. This observation has very important and practical implications for BMB iron quantification

because the assumption of a spherically symmetric source greatly simplifies the quantification and clinical practicality.

In many or even most BMB, the actual geometry can probably be ignored because of far field effects. Indeed, this may be reflected in the definition of BMB as "round" hypointense GRE T_2* (magnitude) image features by recently proposed BMB rating scale (Gregoire et al., 2009). However, other recommendations allow for "ovoid" hypointensities (Greenburg et al., 2009) and the spherical geometry assumption may not be globally applicable. In the present context, far field means that e.g. v_π is large enough that the iron source can be treated as a sphere. Because $\alpha'_\pi > v_\pi > h_\pi$ measurements at α'_π are further from the dipole center and less affected by non-spherical effects than measurements at v_π or h_π. In addition, the larger distances mean a greater dynamic range, advantageous in a pixilated environment. Consistent with these two facts, the plots of α'^3_π generally give slightly better results than v_π^3 and h_π^3 (Fig 3.5 B –D, Fig 3.7 B – D) even though use of α'_π, v_π, and h_π alone all essentially represent spherical methods. Thus, the α'_π parameter appears a promising alternative to the triaxial method for several reasons: no assumptions or knowledge of orientation is necessary, a single orientation and thus a only single MR acquisition in needed, issues of filter compatibility does not arise, and automated count and quantify schemes are much more feasible.

There are several limitations to our triaxial method and its applicability to real BMB quantification.

First of all, the validity of both Eq. 24 and the assumption that image measurement points (B and C in Case 1, and A and C in Case 2 (see Fig 3.2)) lie on the same confocal ellipse (the confocal assumption) remain to be validated. Eqs. 1, 3, 11,

88

and 13 when applied at the points B*, A and C of Fig 3.2C and D, lead to Eq. 24a and not 24b. However, Eq. 24a appears to be inconsistent with simulation data. In particular, the sum of the integrals on the left hand side is greater than the term on the right hand side of the equation. In contrast, Eq.24b, which contains an as of yet unexplained minus sign, seemed at first to give good results in our simulations (Fig 3.5A). However further simulations revealed that at least for Case 2, the sample volume (and thus iron mass) depends on the geometry of the source (Fig 3.6B). The discrepant results regarding the application of Eq. 24b suggest that i) Eq. 24b is after all incorrect, and/or ii) other aspects of the triaxial method (particularly Case 2) are somehow flawed. It is also possible that a similar mass dependence on source dimensions would be discovered for Case 1 if simulated sources had the "right" geometric properties (i.e., ratios of semi-axes). Therefore, what is most needed is further understanding of the mathematical theory underlying the method.

Determining the correctness of the sign in Eq. 24b would be an essential step in this understanding. One possible explanation for the necessity of its presence instead of the predicted opposite sign (i.e., Eq. 24a) is that the relationship between the orientations of the ellipsoids and $\mathbf{B_0}$ for Cases 1 and 2 is not accounted for in Eq. 24a. Unlike, say a spherical system, the ellipsoidal system is directionally dependent (George Dassios, personal communication) and our formulation assumed that the major axis of the ellipsoid was orientated along the x-axis. Therefore, for the parallel case of Case 1 $\mathbf{B_0}$ was also oriented along the x-axis. However, for Case 2, $\mathbf{B_0}$ was along the y-axis. Thus, while the ellipsoids are related by a 90^0 rotation, $\mathbf{B_0}$ is related by a rotation and a reflection, the implications of which merit further study.

Besides Eq. 24, an important candidate for a flaw in our method is the unconfirmed confocal assumption stated above. A stronger statement, of which the above statement is a corollary, is that in the dipole pattern equatorial planes (Fig 3.2B and D) the constant magnetic field contour lines are confocal with the source reference ellipsoid. From considerations of symmetry and the nature of the dipole field perturbations, the phase contour lines in the dipole equatorial plane are expected to appear as "concentric" ellipses that decrease in eccentricity (i.e., become more circular) further from the origin. Qualitatively, our images seem to meet this expectation, but a quantitative confirmation is needed. In addition, the dipole patterns actually represent the projection of the field perturbation onto the $\mathbf{B_0}$ direction, and the implications of this should be understood. Key to the usefulness of the method is the assumption that phase contour lines can be used to infer properties (i.e., h and k) of a susceptibility source of unknown volume. If the confocal assumption is not at least approximately correct, then the triaxial method is indeed flawed, and the usefulness of the method as it stands is uncertain. Therefore, a solid theoretical basis to answer these questions is of paramount importance.

Secondly, the method assumes either a parallel or transverse iron source/main field orientation but not oblique orientations. Generalization of the method at the expense of additional complexity can be done. However, in practice one could rarely, if at all, determine the exact orientation of a real BMB. Further, orthogonal projections of obliquely oriented dipoles may be hard to detect in an automated count and quantify scheme as proposed above, significantly challenging a non-ambiguous scheme. On the other hand, our method may find applications in other problem domains (i.e., outside of

BMB quantification). For small structures where geometric details are less important, assuming that only the principle component of the iron source is transversely or orthogonally oriented may give satisfactory results. An approximate principle direction may even be known ahead of time. In any case, under the non-oblique assumption, the parallel orientation can be excluded under the condition that $\alpha'_\pi / v_\pi < 2^{1/3}$. In our injection data, the parallel case was excluded for 8 of 10 samples.

Thirdly, because the negation of this condition is necessary but not sufficient for a parallel orientation, our method can give ambiguous results as the entries for sample 7‖ and 7⊥ in Table 3.1 indicate. In the current study we used the additional information of a T_2 scan (data not shown) to overcome the ill-posed problem of orientation. In practice such information will not generally be available and best practice may be to average the results from the different orientations and/or report the results as a range. This problem only increases if the second transverse case (i.e., ellipsoid directed along the z-axis) (not developed in the present study) is entered into the analysis.

Fourthly, since the method requires that a_π, b_π, and c_π be determined, two orientations and thus two scans are required, increasing imaging time. However, multiple scans are usually acquired in clinical situations, and the addition or substitution of a single scan may not be a significant limitation.

Finally, as in our previous study, our approach assumes background phase has been reduced to negligible levels and this is attempted using high-pass filtering (McAuley et al., 2010a, Wang et al., 2000). Background phase removal is a fundamental problem in phase imaging and several approaches have been attempted (Neelavalli et al., 2009, Duyn et al., 2007, Cheng et al., 2007, Wang et al., 2000). For homodyne filtering, the choice of

91

filter size is often chosen empirically (Szumowski et al., 2010, McAuley et al., 2010a). The 32x32 filtering we used in our previous study resulted in slightly blunting the phase dipole pattern in horizontal images resulting in smaller a'_π and $b*_\pi$ measurements. Therefore, we employed a 16x32 filter for the horizontal images. The 2D axial scans however, required a 32x32 filter to yield non-distorted dipoles. The significance of the differing filter sizes as well as the effects of filtering in localized dipole sources in general are areas where future research is needed. In any case, the linear relationships predicted by Eqs. 17, 23, 25 and 30 were observed in our experimental data.

Conclusion

In summary, we have proposed a method to quantify localized iron sources of triaxial ellipsoidal geometry using an ellipsoidal harmonic mathematical framework that attempts to relate easily identified image features with source iron mass. Experimental and simulated results show necessary agreement with some aspects of the underlying theory of the method (e.g., linear relationships). However, questions and discrepancies regarding simulations and other aspects of theory do not allow validation of the method as it stands. The method does not seem to display weakness in Case 1 but only Case 2 application however, and investigation into the source of the observed discrepancies is ongoing. However, in both the experimental and simulation data the use of the α'_π parameter with implicit spherical geometric assumptions provided quite adequate results. This is significant for application of a localized quantification method to BMB iron content where the complexity of the triaxial may be less practical. The use of α'_π seems to broaden the possibility of using iron content to provide diagnostic criteria and inform

critical treatment decisions such as bleeding risk of antithrombotic agents in the presence of BMB. Finally, the triaxial method might find application in other areas of medical MR research as well as in industrial applications (Robson and Hall, 2005), materials susceptibility, and MR compatible materials.

References

Akter M, Hirai T, Hiai Y, Kitajima M, Komi M, Murakami R, Fukuoka H, Sasao A, Toya R, Haacke EM, Takahashi M, Hirano T, Kai Y, Morioka M, Hamasaki K, Kuratsu J-I, Yamashita Y. Detection of hemorrhagic hypointense foci in the brain on susceptibility-weighted imaging clinical and phantom studies. Academic Radiology 2007 14(9):1011-1019.

Atlas SW, Mark AS, Grossman RI, Gomori JM. Intracranial hemorrhage: gradient-echo MR imaging at 1.5 T. Comparison with spin-echo imaging and clinical applications. Radiology 1988 168(3):803-807.

Bartzokis, G., Lu, P.H., Tishler, T.A., Fong, S.M., Oluwadara, B., Finn, J.P., Huang, D., Bordelon, Y., Mintz, J., 2007. Myelin breakdown and iron changes in Huntington's disease: pathogenesis and treatment implications. Neurochem Res 32, 1655—1664.

Bizzi A, Brooks RA, Brunetti A, Hill JM, Alger JR, Miletich RS, Francavilla TL, Di Chiro G. Role of iron and ferritin in MR imaging of the brain: a study in primates at different field strengths. Radiology 1990 177(1):59-65.

Bos, C., Viergever, M.A., Bakker, C.J.G., 2003. On the artifact of a subvoxel susceptibility deviation in spoiled gradient-echo imaging. Magnetic Resonance in Medicine: Official Journal of the Society of Magnetic Resonance in Medicine / Society of Magnetic Resonance in Medicine 50, 400-404.

Cheng Y-CN, Hsieh C-Y, Neelavalli J, Liu Q, Dawood MS, Haacke EM. A complex sum method of quantifying susceptibilities in cylindrical objects: the first step toward quantitative diagnosis of small objects in MRI. Magn Reson Imaging 2007 25(8):1171—1180.

Cordonnier, C., van der Flier, W.M., Sluimer, J.D., Leys, D., Barkhof, F., Scheltens, P., 2006. Prevalence and severity of microbleeds in a memory clinic setting. Neurology 66, 1356-1360.

Cordonnier C, Al-Shahi Salman R, Wardlaw J. Spontaneous brain microbleeds: systematic review, subgroup analyses and standards for study design and reporting. Brain: A Journal of Neurology 2007 130(Pt 8):1988-2003.

Cordonnier C, Potter GM, Jackson CA, Doubal F, Keir S, Sudlow CLM, Wardlaw JM, Al-Shahi Salman R. improving interrater agreement about brain microbleeds: development of the Brain Observer MicroBleed Scale (BOMBS). Stroke; a Journal of Cerebral Circulation 2009 40(1):94-99.

Cordonnier C, van der Flier WM, Sluimer JD, Leys D, Barkhof F, Scheltens P. Prevalence and severity of microbleeds in a memory clinic setting. Neurology 2006 66(9):1356-1360.

Dixon WT, Blezek DJ, Lowery LA, Meyer DE, Kulkarni AM, Bales BC, Petko DL, Foo TK. Estimating amounts of iron oxide from gradient echo images. Magnetic Resonance in Medicine 2009;61(5):1132-1136.

Duyn JH, Gelderen Pv, Li T-Q, Zwart JAd, Koretsky AP, Fukunaga M. High-field MRI of brain cortical substructure based on signal phase. Proc Natl Acad Sci U S A 2007 104(28):11796—11801.

Fazekas F, Roob G, Kleinert G, Kapeller P, Schmidt R, Hartung HP. Histopathologic analysis of foci of signal loss on gradient-echo T2*-weighted MR images in patients with spontaneous intracerebral hemorrhage: evidence of microangiopathy-related microbleeds. AJNR Am J Neuroradiol 1999 20(4):637—642.

Gaasch JA, Lockman PR, Geldenhuys WJ, Allen DD, Van der Schyf CJ. Brain iron toxicity: differential responses of astrocytes, neurons, and endothelial cells. Neurochemical Research 2007 32(7):1196-1208.

Gelman, N., Gorell, J.M., Barker, P.B., Savage, R.M., Spickler, E.M., Windham, J.P., Knight, R.A., 1999. MR Imaging of Human Brain at 3.0 T: Preliminary Report on Transverse Relaxation Rates and Relation to Estimated Iron Content. Radiology 210, 759-767.

Greenberg SM, Eng JA, Ning M, Smith EE, Rosand J. Hemorrhage burden predicts recurrent intracerebral hemorrhage after lobar hemorrhage. Stroke 2004 35(6):1415-1420.

Greenberg SM, Vernooij MW, Cordonnier C, Viswanathan A, Al-Shahi Salman R, Warach S, Launer LJ, Van Buchem MA, Breteler MM. Cerebral microbleeds: a guide to detection and interpretation. Lancet Neurology 2009 8(2):165-174.

Gregoire SM, Chaudhary UJ, Brown MM, Yousry TA, Kallis C, Jäger HR, Werring DJ. The Microbleed Anatomical Rating Scale (MARS): reliability of a tool to map brain microbleeds. Neurology 2009 73(21):1759-1766.

Gregoire SM, Werring DJ, Chaudhary UJ, Thornton JS, Brown MM, Yousry TA, Jäger HR. Choice of echo time on GRE T2*-weighted MRI influences the classification of brain microbleeds. Clinical Radiology 2010 65(5):391-394.

Haacke EM, Brown RW, Thompson MR, Venkatesan R. Magnetic Resonance Imaging, Physical Principles and Sequence Design: Wiley-Liss; 1999.

Haacke EM, Xu Y, Cheng Y-CN, Reichenbach JrR. Susceptibility weighted imaging (SWI). Magn Reson Med 2004 52(3):612—618.

Haacke EM, Cheng NYC, House MJ, Liu Q, Neelavalli J, Ogg RJ, Khan A, Ayaz M, Kirsch W, Obenaus A. Imaging iron stores in the brain using magnetic resonance imaging. Magn Reson Imaging 2005 23(1):1—25.

Haacke EM, Ayaz M, Khan A, Manova ES, Krishnamurthy B, Gollapalli L, Ciulla C, Kim I, Petersen F, Kirsch W. Establishing a baseline phase behavior in magnetic resonance imaging to determine normal vs. abnormal iron content in the brain. J Magn Reson Imaging 2007 26(2):256—264.

House, M.J., Pierre, T.G.S., Kowdley, K.V., Montine, T., Connor, J., Beard, J., Berger, J., Siddaiah, N., Shankland, E., Jin, L.-W., 2007. Correlation of proton transverse relaxation rates (R2) with iron concentrations in postmortem brain tissue from alzheimer's disease patients. Magn Reson Med 57, 172—180.

Igase M, Tabara Y, Igase K, Nagai T, Ochi N, Kido T, Nakura J, Sadamoto K, Kohara K, Miki T. Asymptomatic cerebral microbleeds seen in healthy subjects have a strong association with asymptomatic lacunar infarction. Circulation Journal 2009 73(3):530-533.

Jeon, S.-B., Kang, D.-W., Cho, A.H., Lee, E.-M., Choi, C.G., Kwon, S.U., Kim, J.S., 2007. Initial microbleeds at MR imaging can predict recurrent intracerebral hemorrhage. Journal of Neurology 254, 508-512.

Jeon, S.B., Kwon, S.U., Cho, A.H., Yun, S.C., Kim, J.S., Kang, D.W., 2009. Rapid appearance of new cerebral microbleeds after acute ischemic stroke. Neurology 73, 1638-1644.

Kim, J.K., Kucharczyk, W., Henkelman, R.M., 1993. Cavernous hemangiomas: dipolar susceptibility artifacts at MR imaging. Radiology 187, 735-741.

Kimberly W.T., Gilson A., Rost N.S., Rosand J., Viswanathan A., Smith E.E., Greenberg S.M., 2009. Silent ischemic infarcts are associated with hemorrhage burden in cerebral amyloid angiopathy. Neurology 72(14):1230-1235.

Kirsch W, McAuley G, Holshouser B, Petersen F, Ayaz M, Vinters HV, Dickson C, Haacke EM, Britt Iii W, Larsen J, Kim I, Mueller C, Schrag M, Kido D. Serial Susceptibility Weighted MRI Measures Brain Iron and Microbleeds in Dementia. Journal of Alzheimer's Disease 2009 17(3):599-609.

Knudsen KA, Rosand J, Karluk D, Greenberg SM. Clinical diagnosis of cerebral amyloid angiopathy: validation of the Boston criteria. Neurology 2001 56(4):537-539.

Landau LD, Pitaevskii LP, Lifshitz E. Electrodynamics of Continuous Media, Second Edition: Volume 8. 2nd ed. Butterworth-Heinemann; 1984.

Lee S-H, Ryu W-S, Roh J-K. Cerebral microbleeds are a risk factor for warfarin-related intracerebral hemorrhage. Neurology 2009 72(2):171-176.

Maynard CJ, Cappai R, Volitakis I, Cherny RA, White AR, Beyreuther K, Masters CL, Bush AI, Li Q-X. Overexpression of Alzheimer's disease amyloid-beta opposes the age-dependent elevations of brain copper and iron. The Journal of Biological Chemistry 2002 277(47):44670-44676.

McAuley G, Schrag M, Sipos P, Sun S-W, Obenaus A, Neelavalli J, Haacke EM, Holshouser B, Madácsi R, Kirsch W. Quantification of punctate iron sources using magnetic resonance phase. Magnetic Resonance in Medicine 2010a 63(1):106-115.

McAuley G, Schrag M, Barnes S, Obenaus A, Dickson A, Holshouser B, Kirsch W. Iron quantification of microbleeds in postmortem brain. Accepted pending minor revisions in Magnetic Resonance in Medicine 2010b.

Menon, R.S., Kidwell, C.S., 2009. Neuroimaging demonstration of evolving small vessel ischemic injury in cerebral amyloid angiopathy. Stroke; a Journal of Cerebral Circulation 40, e675-677.

Mills PH, Wu Y-JL, Ho C, Ahrens ET. Sensitive and automated detection of iron-oxide-labeled cells using phase image cross-correlation analysis. Magnetic Resonance Imaging 2008 26(5):618-628.

Neelavalli J, Cheng Y-CN, Jiang J, Haacke EM. Removing background phase variations in susceptibility-weighted imaging using a fast, forward-field calculation. Journal of Magnetic Resonance Imaging: JMRI 2009 29(4):937-948.

Neema M, Arora A, Healy BC, Guss ZD, Brass SD, Duan Y, Buckle GJ, Glanz BI, Stazzone L, Khoury SJ, Weiner HL, Guttmann CRG, Bakshi R. Deep gray matter involvement on brain MRI scans is associated with clinical progression in multiple sclerosis. Journal of Neuroimaging 2009 19(1):3-8.

Ogg, R.J., Langston, J.W., Haacke, E.M., Steen, R.G., Taylor, J.S., 1999. The correlation between phase shifts in gradient-echo MR images and regional brain iron concentration. Magn Reson Imaging 17, 1141—1148.

Ordidge, R.J., Gorell, J.M., Deniau, J.C., Knight, R.A., Helpern, J.A., 1994. Assessment of relative brain iron concentrations using T2-weighted and T2*-weighted MRI at 3 Tesla. Magn Reson Med 32, 335—341.

Pintaske J, Müller-Bierl B, Schick F. Geometry and extension of signal voids in MR images induced by aggregations of magnetically labelled cells. Phys Med Biol 2006b 51(18):4707—4718.

Reichenbach, J.R., Venkatesan, R., Schillinger, D.J., Kido, D.K., Haacke, E.M., 1997a. Small vessels in the human brain: MR venography with deoxyhemoglobin as an intrinsic contrast agent. Radiology 204, 272-277.

Reichenbach JR, Venkatesan R, Schillinger DJ, Kido DK, Haacke EM. Small vessels in the human brain: MR venography with deoxyhemoglobin as an intrinsic contrast agent. Radiology 1997b 204(1):272-277.

Robson P, Hall L. Identifying particles in industrial systems using MRI susceptibility artefacts. AIChE Journal 2005 51(6):1633-1640.

Schäfer A, Wharton S, Gowland P, Bowtell R. Using magnetic field simulation to study susceptibility-related phase contrast in gradient echo MRI. NeuroImage 2009 48(1):126-137.

Schenck, J.F., Zimmerman, E.A., 2004. High-field magnetic resonance imaging of brain iron: birth of a biomarker? NMR in Biomedicine 17, 433-445.

Schrag M, McAuley G, Pomakian J, Jiffry A, Tung S, Mueller C, Vinters H, Haacke E, Holshouser B, Kido D, Kirsch W. Correlation of hypointensities in susceptibility-weighted images to tissue histology in dementia patients with cerebral amyloid angiopathy: a postmortem MRI study. Acta Neuropathologica 2010 119(3):291-302.

Shmueli K, de Zwart JA, van Gelderen P, Li T-Q, Dodd SJ, Duyn JH. Magnetic susceptibility mapping of brain tissue in vivo using MRI phase data. Magnetic Resonance in Medicine 2009 62(6):1510-1522.

Smith M.A., Harris P.L., Sayre L.M., Perry G., 1997. Iron accumulation in Alzheimer disease is a source of redox-generated free radicals. Proc Natl Acad Sci USA. 94, 9866-8.

Smith MA, Zhu X, Tabaton M., Liu G., McKeel D.W., Cohen M.L., Wang X., Siedlak S.L., Hayashi T., Nakamura M., Nunomura A., Perry G., 2010. Increased Iron and Free Radical Generation in Preclinical Alzheimer Disease and Mild Cognitive Impairment. J Alzheimers Dis. 19, 363-372.

Soo YOY, Yang SR, Lam WWM, Wong A, Fan YH, Leung HHW, Chan AYY, Leung C, Leung TWH, Wong LKS. Risk vs benefit of anti-thrombotic therapy in ischaemic stroke patients with cerebral microbleeds. Journal of Neurology 2008 255(11):1679-1686.

Staals, J., van Oostenbrugge, R.J., Knottnerus, I.L.H., Rouhl, R.P.W., Henskens, L.H.G., Lodder, J., 2009. Brain microbleeds relate to higher ambulatory blood pressure levels in first-ever lacunar stroke patients. Stroke; a Journal of Cerebral Circulation 40, 3264-3268.

Sten JC-E, 2006. Ellipsoidal harmonics and their application in electrostatics. Journal of Electrostatics 64, 647-654.

Sveinbjornsdottir S, Sigurdsson S, Aspelund T, Kjartansson O, Eiriksdottir G, Valtysdottir B, Lopez OL, van Buchem MA, Jonsson PV, Gudnason V, Launer LJ. Cerebral microbleeds in the population based AGES-Reykjavik study: prevalence and location. Journal of Neurology, Neurosurgery, and Psychiatry 2008 79(9):1002-1006.

Szumowski J, Bas E, Gaarder K, Schwarz E, Erdogmus D, Hayflick S. Measurement of brain iron distribution in Hallevorden-Spatz syndrome. Journal of Magnetic Resonance Imaging: JMRI 2010 31(2):482-489.

Tanaka A., Ueno Y., Nakayama Y., Takano K., Takebayashi S., 1999. Small chronic hemorrhages and ischemic lesions in association with spontaneous intracerebral hematomas. Stroke. 30, 1637-1642.

Tong KA, Ashwal S, Holshouser BA, Shutter LA, Herigault G, Haacke EM, Kido DK. Hemorrhagic shearing lesions in children and adolescents with posttraumatic diffuse axonal injury: improved detection and initial results. Radiology 2003 227(2):332—339.

Tong, K.A., Ashwal, S., Holshouser, B.A., Nickerson, J.P., Wall, C.J., Shutter, L.A., Osterdock, R.J., Haacke, E.M., Kido, D., 2004. Diffuse axonal injury in children: clinical correlation with hemorrhagic lesions. Ann Neurol 56, 36—50.

van Rooden S, van der Grond J, van den Boom R, Haan J, Linn J, Greenberg SM, van Buchem MA. Descriptive analysis of the Boston criteria applied to a Dutch-type cerebral amyloid angiopathy population. Stroke 2009 40(9):3022-3027.

Vernooij, M.W., van der Lugt, A., Ikram, M.A., Wielopolski, P.A., Niessen, W.J., Hofman, A., Krestin, G.P., Breteler, M.M.B., 2008. Prevalence and risk factors of cerebral microbleeds: the Rotterdam Scan Study. Neurology 70, 1208-1214.

Vernooij MW, Haag MDM, van der Lugt A, Hofman A, Krestin GP, Stricker BH, Breteler MMB. Use of Antithrombotic Drugs and the Presence of Cerebral Microbleeds: The Rotterdam Scan Study. Arch Neurol 2009 66(6):714-720.

Zhu, W.-z., Zhong, W.-d., Wang, W., Zhan, C.-j., Wang, C.-y., Qi, J.-p., Wang, J.-z., Lei, T., 2009. Quantitative MR Phase-corrected Imaging to Investigate Increased Brain Iron Deposition of Patients with Alzheimer Disease1. Radiology 253, 497-504.

Viswanathan, A., Chabriat, H., 2006. Cerebral microhemorrhage. Stroke; a Journal of Cerebral Circulation 37, 550-555.

Vymazal J, Klempír J, Jech R, Zidovská J, Syka M, Ruzicka E, Roth J. MR relaxometry in Huntington's disease: Correlation between imaging, genetic and clinical parameters. Journal of the Neurological Sciences 2007 263(1-2):20-25.

Wang Y, Yu Y, Li D, Bae KT, Brown JJ, Lin W, Haacke EM. Artery and vein separation using susceptibility-dependent phase in contrast-enhanced MRA. J Magn Reson Imaging 2000 12(5):661—670.

Xu X, Wang Q, Zhang M. Age, gender, and hemispheric differences in iron deposition in the human brain: an in vivo MRI study. NeuroImage 2008 40(1):35-42.

Yakushiji Y, Nishiyama M, Yakushiji S, Hirotsu T, Uchino A, Nakajima J, Eriguchi M, Nanri Y, Hara M, Horikawa E, Kuroda Y. Brain microbleeds and global cognitive function in adults without neurological disorder. Stroke 2008 39(12):3323-3328.

Zhang W, Sun S-G, Jiang Y-H, Qiao X, Sun X, Wu Y. Determination of brain iron content in patients with Parkinson's disease using magnetic susceptibility imaging. Neuroscience Bulletin 2009 25(6):353-360.

CHAPTER FOUR

IRON QUANTIFICATION OF MICROBLEEDS IN POSTMORTEM

BRAIN

Grant McAuley[a], Matthew Schrag[a], Samuel Barnes[d], Andre Obenaus[b,c,e], April Dickson[a], Barbara Holshouser[e], and Wolff Kirsch[a,*]

Neurosurgery Center for Research, Training and Education[a], Biophysics and Bioengineering, School of Science and Technology[b], Non-Invasive Imaging Laboratory, Radiation Medicine[c], Loma Linda University, Loma Linda, CA, 92350, USA
Biomedical Engineering, Wayne State University[d], Detroit, Michigan, 48202, USA
Radiology[e], Loma Linda University Medical Center, Loma Linda, CA, 92350, USA

Manuscript body word count: 5,076

[*]Send correspondence to:
Wolff Kirsch
Neurosurgery Center for Research, Training and Education
Loma Linda University,
11175 Campus Street, CPA11113
Loma Linda, CA, 92354
E-mail: wkirsch@llu.edu
Tel: 909-558-7070
Fax: 909-558-0472

Abstract

Brain microbleeds (BMB) are associated with chronic and acute cerebrovascular disease and present a source of pathologic iron to the brain proportional to extravasated blood. Therefore, BMB iron content is potentially a valuable biomarker. We tested non-invasive phase image methods to quantify iron content and estimate true source diameter (i.e., unobscured by the blooming effect) of BMB in postmortem human tissue. Tissue slices containing BMB were imaged using a susceptibility weighted imaging protocol at 11.7T. BMB lesions were assayed for iron content using atomic absorption spectrometry. Measurements of geometric features in phase images were related to lesion iron content and source diameter using a mathematical model. BMB diameter was estimated by image feature geometry alone without explicit relation to the magnetic susceptibility. A strong linear relationship (R^2=0.984, p<0.001) predicted by theory was observed in the experimental data, presenting a tentative standardization curve where BMB iron content in similar tissues could be calculated. In addition, we report BMB iron mass measurements, as well as upper bound diameter and lower bound iron concentration estimates. Our methods potentially allows the calculation of brain iron load indices based on BMB iron content and classification of BMB by size unobscured by the blooming effect.

Introduction

Brain microbleeds (BMB) are associated with ischemic stroke, silent lacunar infarcts, non-traumatic intracerebral hemorrhage (ICH), cerebral amyloid angiopathy (CAA), neurotrauma, Alzheimer's disease (AD), vascular dementia, cognitive decline, hypertension and age (Cordonnier et al., 2007; Greenberg et al., 2009; Igase et al., 2009; Fazekas et al., 1999; Tong et al., 2003; Cordonnier et al., 2006; Kirsch et al., 2009; Yakushiji et al., 2008; Sveinbjornsdottir et al., 2008). The presence of BMB in ischemic stroke, ICH and CAA is associated with future hemorrhage, (Greenberg et al., 2009; Soo et al., 2008; Greenberg et al., 2004) but whether it confers risk for first ever stroke has not been determined (Greenberg et al., 2009; Cordonnier et al., 2007). Risk of bleeding associated with thrombolytic and thrombotic agents is a controversial open question of considerable importance (Greenberg et al., 2009; Greenberg et al., 2004; Vernooij et al., 2009; Lee et al., 2009). Thus, the presence of BMB is related to both chronic and acute illness of significant social and economic impact in our aging population.

BMB are detected as focal signal losses in gradient recalled echo (GRE) T_2* magnetic resonance (MR) imaging and have been histopathologically related mainly to hemosiderin (Fazekas et al., 1999; Schrag et al., 2010). Hemosiderin, the iron-protein complex associated with pathologic iron storage following hemorrhage (Bizzi et al., 1990), is visible in MR images due to it paramagnetic iron content and serves as a marker for BMB (Atlas et al., 1988). Iron-mediated tissue damage has been implicated in neurotrauma, cerebral vascular disease and a variety of neurodegenerative maladies (Vymazal et al., 2007; Gaasch et al., 2007; Neema et al., 2009). Because BMB present a source of pathologic iron to the brain proportional to extravasated blood, quantification of

103

iron content within a BMB is potentially a valuable biomarker for disease progression, treatment efficacy and risk factor assessment (Greenberg et al., 2009; Haacke et al., 2005).

Past efforts to quantify brain iron have focused on content estimation within distributed brain regions (Kirsch et al., 2009; Vymazal et al., 2007; Neema et al., 2009; Haacke et al., 2005; Szumowski et al., 2010; Haacke et al., 2007; Xu et al., 2008; Zhang et al., 2009). However, BMB represent a localized source of iron deposition. In addition, conventional "magnitude" MR images have significant limitations especially for localized iron quantification (Dixon et al., 2009; McAuley et al., 2010a). Moreover, due to susceptibility effects, the hypointensities in magnitude GRE T_2^* images associated with BMB typically appear larger than the actual tissue lesion. Thus, this well known "blooming effect" generally obscures the true dimensions of an iron susceptibility source (Schrag et al., 2010; Pintaske et al., 2006b). Finally, susceptibility-weighted imaging (SWI) is a GRE sequence that uses magnetic susceptibility-dependent phase information to provide or enhance image contrast (Reichenbach et al., 1997a; Haacke et al., 2004). SWI has been shown to be more sensitive in BMB detection compared to more conventional GRE sequences (Tong et al., 2003; Akter et al., 2007).

We recently proposed a method to noninvasively quantify localized iron sources using SWI phase images. This method was validated using a model phantom system containing samples of ferric oxy-hydroxide (McAuley et al., 2010a). The purpose of the present research was to test the use of a similar method to quantify iron content and estimate true source diameter (i.e., unobscured by the blooming effect) in actual BMB from postmortem human tissue. In addition, unlike our previous report, source diameter

was estimated by image feature geometry alone, without explicit relation to the magnetic susceptibility of the iron source. Finally, we report iron mass values (based on sensitive tissue measurements), as well as diameter and iron concentration estimates (based on phase image measurements) for real BMB in postmortem AD/CAA brain. Iron content and concentration of BMB have been heretofore absent in the literature.

Materials and Methods

Theoretical Background and Rationale

MR voxels containing and surrounding paramagnetic (or ferromagnetic) brain iron deposits have an altered local magnetic field ΔB, and thus an altered magnetization phase with respect to their neighbors. This phase difference is detectible in GRE pulse sequences and is described by the formula (for a right handed system):

$$\Delta \phi = -\gamma \Delta B T_E$$

[1]

where $\Delta \phi$ is the change in phase, γ is the proton gyromagnetic ratio, and T_E is the echo time (Haacke et al., 1999). Thus, the amount of iron in a voxel can potentially be related to the phase.

In a previous paper (McAuley et al., 2010a) we discussed how an easily identified parameter in modulo 2π phase-wrapped images can be mathematically related to iron mass in a localized spherical sample (Eq. 2). Briefly, Fig 4.1A shows a schematic cross section of an iron sample dipole phase pattern induced by the main MRI magnetic field (B_0), and Fig 4.1C shows a corresponding phase profile taken across the red dotted line in Fig 4.1A. The value on the abscissa corresponding to $\Delta\phi_D = \pi$ is denoted by r_π, (Robson and Hall, 2005) and r_π is easily measured from the wrapped profile (Fig 4.1D) or the

rectangle bounding the π-phase wrap of the dipole pattern (Fig 4.1A). Under the

assumptions that i) the magnetic susceptibility is constant both internal (χ_i) and external

(χ_e) to the iron sample, ii) $\Delta\chi$, the susceptibility difference, defined as $\Delta\chi \equiv (\chi_i - \chi_e)$, is

very small ($\sim 10^{-5}$), iii) the density of the samples ρ is constant, iv) the source is roughly

spherical, and v) all background phase has been removed, r_π is related to iron mass of the

sample by Eq. 2 (McAuley et al., 2010a):

$$m_{Fe} = \left(\frac{4\pi^2 \rho}{\gamma' \Delta\chi B_0 T_E} \right) r_\pi^3$$

[2]

The true radius a of the iron source (unobscured by the blooming effect) can also

be related to r_π by Eq. 3, and for a given $\Delta\chi$, r_π can in principle be converted between

magnet field strengths and echo times by Eq. 4 (McAuley et al., 2010a):

$$a = \left(\frac{3\pi}{\gamma' \Delta\chi B_o T_E} \right)^{1/3} r_\pi$$

[3]

$$\frac{r_{\pi_2}}{r_{\pi_1}} = \left(\frac{B_{0_2} T_{E_2}}{B_{0_1} T_{E_1}} \right)^{1/3}$$

[4]

In this present study, we denote by r'_π the value on the ordinate dipole axis

corresponding to $\Delta\phi_D = \pi$. Thus, r'_π is analogously related to the vertical π-wrap and

phase profile (taken along black dotted line in Fig 4.1A) as r_π is to the horizontal. It

follows from equations 2 and 5 of McAuley et al., (McAuley et al., 2010a) that the profile

intensities are proportional to each other (proportionality constant of -2), and that r_π and
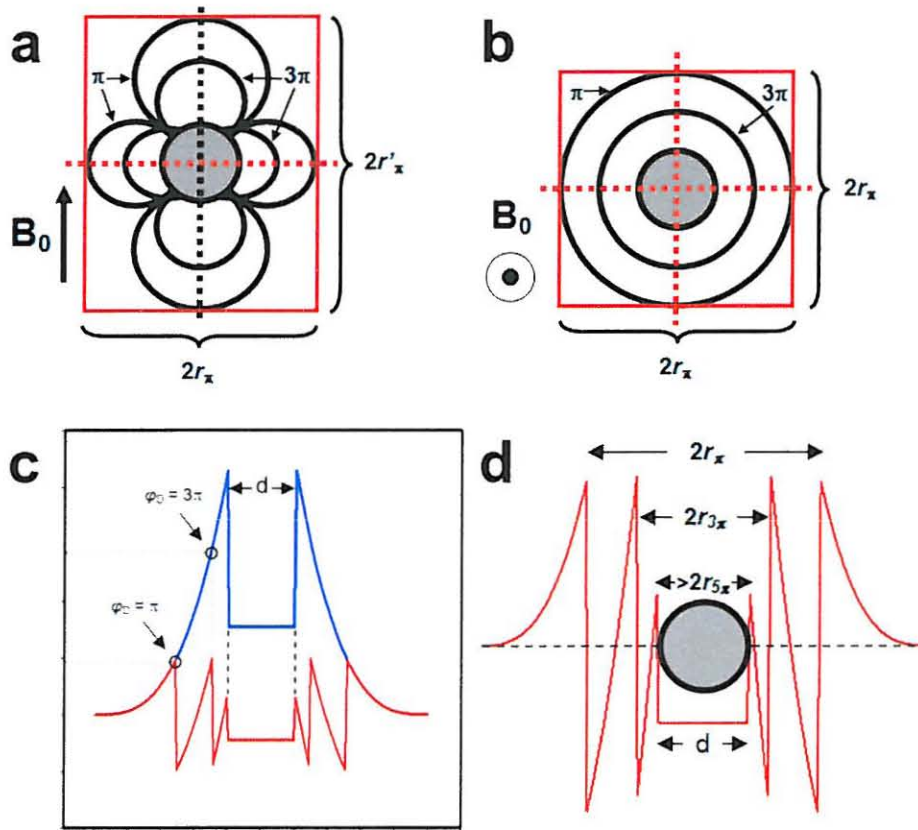
Figure 4.1: Image Parameter Measurement – The phase image parameters r_π and r'_π can be measured using bounding rectangles or phase profiles. A) Bounding rectangle drawn around schematic of a spherical dipole pattern in coronal orientation. The widths and heights of the rectangle (solid red) are respectively $2r_\pi$ and $2r'_\pi$. The black lines represent the phase wraps (shown are π and 3π wraps). The main field B_0 is parallel to the axis of the dipole. B) Bounding rectangle drawn around the dipole in axial orientation showing π and 3π phase wraps. The plane shown is a cross section of the equatorial plane of panel A, thus the dimensions are equal to $2r_\pi$. The main field is shown projecting out of the plane of the page. C) Phase profiles drawn along the dipole equator (dotted red lines in panel A and B) appear modulo 2π (red trace). These wrapped profiles can be used to measure r_π, or can in principle be unwrapped (blue trace) and used to i) estimate, d, the diameter of the iron source or ii) an arbitrary phase value (eg, 3π). The parameter r'_π can similarly be related to the phase profile taken along the vertical black dotted line in panel A. D) A magnified view of the wrapped profile in panel C superimposed with a circle representing a spherical iron source. Peak to peak widths of phase wrappings are proportional to r_π and $r_{3\pi}$. Note that the distance between the most medial peaks is equal the diameter of the source d. However, since these peaks do not represent a full phase wrapping, $d > 2r_{5\pi}$, and d is bounded as: $r_{5\pi} < d < r_{3\pi}$.

r'_π are related by Eq. 5 below. Thus, r'_π analogs of Eqs. 2 – 4 can be expressed as Eqs. 6 – 8:

$$r'_\pi = 2^{1/3} r_\pi \tag{5}$$

$$m_{Fe} = \left(\frac{2\pi^2 \rho}{\gamma \Delta X B_0 T_E} \right) r'^3_\pi \tag{6}$$

$$a = \left(\frac{3\pi}{2\gamma \Delta X B_o T_E} \right)^{1/3} r'_\pi \tag{7}$$

$$\frac{r'_{\pi_2}}{r'_{\pi_1}} = \left(\frac{B_{0_2} T_{E_2}}{B_{0_1} T_{E_1}} \right)^{1/3} \tag{8}$$

Both r_π and r'_π can simultaneously be measured from the dimensions of the rectangle bounding the dipole phase pattern as shown in Fig 4.1A. Because r'_π is larger than r_π (Eq. 5) it has the advantage of a larger dynamic range compared with r_π.

Fig 4.1B shows an axial cross section of the phase-wrapped dipole pattern corresponding to the equatorial plane of Fig 4.1A. The prominent lines in Fig 4.1A and B correspond to phase wraps (π and 3π wraps are shown) which appear as concentric circles in the axial orientation for a spherical source. Thus, r_π can alternately be determined from axial bounding rectangles (Fig 4.1B). In addition, the horizontal profile (along dashed red line of Fig 4.1A and shown in Fig 4.1 C and D) is equivalent to an axial profile along any diameter (eg, along dashed red lines of Fig 4.1B), and the concentric rings of Fig 4.1B correspond with the phase wraps of the wrapped profile in Fig 4.1D.

Careful examination of Fig 4.1B and D reveal that ideally, phase profiles and axial phase patterns can be used to determine the diameter of a susceptibility source (Fig 4.1C and D): the last full phase wrap is an upper bound to the source diameter, and the last profile peak (not necessarily a phase wrap) corresponds the source diameter d itself. In practice, signal loss in noisy dipole centers and pixelation may obscure higher order phase wraps and diameter peaks. Nevertheless, the sequence of *phase wrap diameters* $2r_\pi$, $2r_{3\pi}$, $2r_{5\pi}$, etc. that are discernable provide increasingly better approximations to d, with the innermost discernable *phase peak diameter* (which is not necessarily a phase wrap) d^*, being the best upper bound source diameter estimate. It follows from equation 4 of McAuley et al., (McAuley et al., 2010a) that $r_{n\pi} = n^{(-1/3)}r_\pi$. This implies that higher order phase wrap diameters need not be measured directly. If higher order phase wraps or peaks are present, related phase wrap diameters can be calculated based on the most robust wrap parameter, r_π. This allows the calculation of a lower bound to the best source diameter estimates based on a hypothetically defined "next phase wrap diameter" (Fig 4.1D). The consequence of the above discussion is that bounded source diameters can be estimated or defined allowing classification of sources based on diameter thresholds unobscured by the blooming effect. In addition, while Eqs. 3 and 7 require a knowledge of $\Delta\chi$ to relate source diameter to the image parameters r_π and r'_π, in principle diameter can be determined by phase geometry alone.

The rationale used to validate the quantification method in actual BMB in postmortem tissue was similar to our previous work (McAuley et al., 2010a). Eq. 6 predicts a proportional relationship between the r'_π parameter and sample iron mass. Therefore, a plot of these experimentally measured variables was used to verify the

prediction and validate the method. Assuming similar values of iron sample density and susceptibility, such a plot can potentially be used as a standard curve to predict iron content in similar samples. In addition, we used phase peak diameter measurements to estimate true BMB source diameter and iron concentration.

Postmortem Human BMB Sample Preparation

Postmortem human brain tissue was donated from the Alzheimer's Disease Research Center Brain Bank at the University of California, Los Angeles. The research protocol was approved by the Institutional Review Board of Loma Linda University Medical Center. On average, five 1 cm coronal slices representing frontal, temporal/parietal and occipital lobar areas were obtained from three cases histopathologically diagnosed as comorbid for advanced AD (Braak and Braak V-VI) and CAA (Vonsattel stage 3). The tissue slabs were embedded in 2% agarose and imaged on a 3T MRI clinical scanner (Trio/Tim, Seimens Medical Solutions, Erlangen, Germany) using a SWI protocol similar to (Schrag et al., 2010). These *preparation images* were then used to identify BMB. Approximately 40 small tissue slices were dissected from the slabs, each containing at least one BMB. To alleviate air-tissue interface susceptibility artifacts, tissue slices were embedded in 2% agarose in plastic scintillation tubes.

Magnetic Resonance Imaging

Besides the 3T SWI preparation image sequence used in sample preparation (see above), we used two 11.7T SWI sequences in this study (referred to in text as *data images*): a 3D SWI coronal sequence, and a 2D axial sequence. The 2D sequence was

used because comparative 3D axial scans had significant signal inhomogeneities and background phase apparently due to inadequate magnetic shimming. To acquire data images, sample tubes were scanned in an 11.7T small vertical-bore MR scanner (Bruker Biospin, Billerica MA) using the following parameters : 1): 3D coronal sequence: TR/TE: 100/7 ms, NEX: 1, FOV: 2.2 cm, and 32 slices of thickness 688 μm. 2) a 2D SWI axial sequence: TR/TE: 154.4-617/7 ms, NEX: 4, and 20-40 slices of thickness 688 μm. For both 3D and 2D scans: flip angle: 20°, matrix: 256 x 256, in-plane resolution: 85.9 μm x 85.9 μm.

Image and Data Processing

Raw coronal and axial phase images were high-pass filtered with 16x32 and 32x32 frequency domain filters, respectively (Wang et al., 2000) using SPIN software (MRI Institute, Detroit, MI). Magnitude images were multiplied four times by a phase mask created from the high-pass filtered (HP) images (Haacke et al., 2004) to produce phase-enhanced magnitude images. The image parameters r_π and r'_π were obtained from the coronal HP images using the height and width of the rectangle bounding the dipole phase pattern of each sample. In addition, the ratio of the sides of rectangles bounding dipole patterns in the axial images were used to help assess the spherical symmetry of the samples. Bounding rectangles are shown in the schematics of Fig 4.1A and B, and for real data samples in Fig 4.3I and J. Using the ImageJ software package (ImageJ, NIH), the rectangle was drawn, its height and width were determined, and r_π (r'_π) is calculated as ½ of width (height) of the rectangle.

Iron Content Determination

Tissue slices were removed from agarose and BMB were located in the slices with the aid of SWI data images. Small blocks of tissue surrounding the BMB were dissected from the slices using a diamond knife (Fig 4.2). To increase the fraction of BMB iron verses background iron, the surrounding tissue in each block was trimmed away as deemed necessary or practical. Control blocks (not containing BMB) were also dissected from similar tissue (e.g., cortical grey matter) as blocks containing BMB. Samples were wet ashed similar to Maynard et al., (Maynard et al., 2002): blocks (2 – 21 mg) were dissolved in 250 μl of 70% HNO_3 for 12 to 48 hours, heated at 80°C for 20 min, and allowed to cool to room temperature. 250 μl of 10M of H_2O_2 were added, and after 30 min, samples we heated samples at 70°C for 15 min and allowed to cool. Iron concentrations of control and BMB blocks were measured in triplicate by graphite furnace atomic absorption spectrometry (SpectrAA 220Z, Varian, Victoria, Australia). BMB iron content was then determined using Eq. 9:

$$(m_{Fe})_{BMB} = (m_{Tissue})_{BMB} \left([Fe]_{BMB} - [Fe]_{CONTROL}\right) \qquad [9]$$

where $(m_{Fe})_{BMB}$ is the iron content (i.e., iron mass) of the BMB, $(m_{Tissue})_{BMB}$ is the mass of the BMB tissue block, and $[Fe]_{BMB}$ and $[Fe]_{CONTROL}$, are the iron concentrations of the BMB and control tissue blocks respectively.

BMB Diameter and Iron Concentration Calculation

Bounding rectangles were drawn around the innermost hyperintense ring in axial dipole patterns from 13 samples (Fig 4.3K and L). The average of the dimensions of the rectangle was taken as the diameter of the lesion. Though the average ratio of the rectangle dimensions was 0.96±0.03 (mean±SEM), the dimensions typically differed by a

few pixels (a 0 pixel difference in 4 samples, 1 pixel in 5 samples, 2 pixels in 3 samples, and 3 pixels in 1 sample), and rectangles were easier to objectively place around the rings than circles. In cases of uncertainty regarding the location or measurement of the innermost ring (8 of 13 samples), a ring with the larger diameter was chosen instead of a putative ring with a smaller diameter. The phase diameters $2r_{3\pi}$, $2r_{5\pi}$, and $2r_{7\pi}$ were calculated using the corresponding r_π for each sample according to the formulas: $r_{n\pi} = n^{-1/3} r_\pi$ for n = 3, 5, and 7. Sample iron mass (as determined above) was divided by $(\pi/6)$ d^3 to obtain iron concentrations. Units of $\mu g/cm^3$ were converted to $\mu g/g$ wet tissue weight assuming a tissue density equal to water.
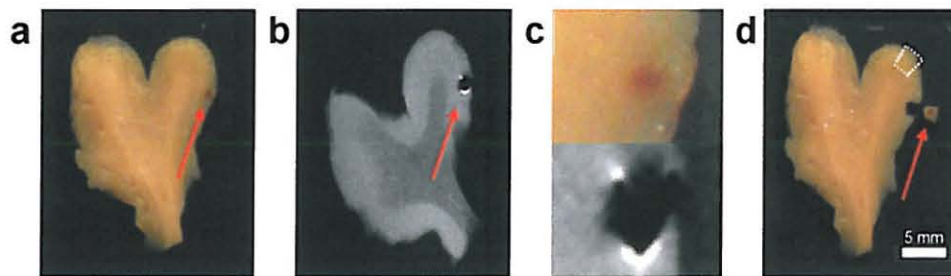
Figure 4.2: BMB in Postmortem Brain – A) Tissue slices were embedded in agarose and scanned at high field MRI. Arrows point to a cortical BMB and B) a T1 weighted image reveals the presence of the BMB (11.7T, TR/TE: 630.8/17.9, NEX: 4, FOV: 22 mm, MAT: 256x256, Thk: 0.3mm). C) Close-up view of the tissue BMB (top of panel) and the corresponding MR image correlate (bottom of panel). D) Small pieces of tissue containing (red arrow) or free of BMB (cut from dotted region) were dissected and assayed for iron content using atomic absorption spectroscopy.

Sample Inclusion/Exclusion

Over 40 putative BMB were originally identified in 40 11.7T SWI data image scans. For practical reasons, a smaller subset consisting of 26 of the most promising putative BMB were chosen and afterward underwent image and tissue processing. Selection was based primarily on the quality of the dipole appearance (eg, symmetry, distinct edges) seen in magnitude SWI scans.

After image and tissue processing, seven samples were excluded from iron content analysis: one sample was damaged during dissection, two samples displayed inadequate background phase removal, one sample dipole was due to an air bubble, one sample dipole was highly distorted, and two samples displayed faint and indistinct dipoles. Six additional samples were excluded from BMB diameter and iron concentration analysis based on axial images: axial images were not available (one sample), inadequate background phase removal (three samples), and indistinct dipole phase patterns (two samples). In total, 19 samples were used for iron content determination, and 13 samples for BMB diameter and iron concentration estimates.

Statistical Analysis

The predicted proportional relationships between BMB iron mass and the image parameter r'_{π} was tested by linear regression analysis using SigmaPlot version 11 (Systat Software, Inc., Chicago, IL). Plots of these variables were constructed along with a best-fit least squares regression lines. Normality of BMB iron concentration was tested using a Shapiro-Wilk test. Statistical significance was considered at $p \leq 0.05$.

Results

Magnitude, raw phase, high-pass filtered phase and phase-enhanced magnitude coronal and axial images of two BMB samples are shown in Fig 4.3. Robust characteristic dipole patterns are seen in each image (McAuley et al., 2010a; Pintaske et al., 2006b). High-pass filtered images generally exhibited dipole patterns with clearly visible phase wraps surrounded by a largely homogenous background (Fig 4.3C, G, I, J). Measured iron mass, r'_π, r_π, r'_π to r_π ratio, as well as estimated diameter and iron concentration is shown for BMB samples in Table 4.1. The average r'_π to r_π ratio was 1.25±0.03 (mean±SEM) consistent with the theoretical value of $2^{1/3} = 1.26$ for a spherical source. This implies that the filtering did not significantly distort the aspect ratio of the dipole pattern. BMB iron mass vs. r'^3_π is plotted in Fig 4.4, and exhibits a strong linear relationship ($R^2 = 0.984$, $p < 0.001$) between variables with a slope of 1290 µg/cm³ ($p < 0.001$). The y-intercept of the plot is small but statistically significant (-0.309 µg, $p = 0.021$). This value is smaller than all the iron masses of the samples except one (Sample 15 in Table 4.1), and can be interpreted as an indicator of the sensitivity of the technique in the present context. The strong linear relationship is predicted by Eq. 6 and thus confirms the usefulness of our quantification method to measure iron content in BMB from human tissues. BMB iron content ranged from 0.065 to 13.1 µg (median 1.0). Upper bound BMB estimated diameters ranged from 0.82 to 1.5 mm (median 1.0 mm) (Fig 4.5). Lower bound BMB iron concentration values were normally distributed (W-Statistic = 0.932, $p = 0.363$) with a mean value of 1842 µg/g tissue. Ten of 13, and 12 of 13 samples fell within ± 1, or ± 2 standard deviations about the mean, respectively (Fig 4.6).

Table 4.1: Postmortem BMB Data - Iron mass was measured by atomic absorption spectrometry. r'_π and r_π are measured by bounding rectangles in coronal filtered phase images (Fig 4.3I). Diameter and concentration estimates are determined as described in text.

Sample	m_{Fe} (µg)	r'_π (mm)	r_π (mm)	r'_π / r_π	d (mm)	[Fe] (µg/g)
1	0.73 ± 0.05	0.86 ± 0.19	0.65 ± 0.12	1.33	--[a]	--[a]
2	0.98 ± 0.02	0.99 ± 0.06	0.77 ± 0.06	1.28	1.03 ± 0.07	1705 ± 358
3	1.54 ± 0.03	1.03 ± 0.06	0.86 ± 0.06	1.20	1.20 ± 0.10	1687 ± 438
4	0.90 ± 0.02	0.86 ± 0.06	0.73 ± 0.06	1.18	0.99 ± 0.07	1786 ± 391
5	0.86 ± 0.04	0.95 ± 0.06	0.65 ± 0.06	1.47	0.86 ± 0.09	2580 ± 811
6	1.04 ± 0.03	1.20 ± 0.06	0.86 ± 0.06	1.40	1.16 ± 0.09	1269 ± 295
7	2.01 ± 0.09	1.29 ± 0.06	0.99 ± 0.06	1.30	1.03 ± 0.10	3502 ± 1067
8	1.14 ± 0.07	1.07 ± 0.06	0.73 ± 0.06	1.47	--[a]	--[a]
9	0.43 ± 0.06	0.86 ± 0.06	0.60 ± 0.06	1.43	0.82 ± 0.07	1499 ± 453
10	0.55 ± 0.03	0.77 ± 0.06	0.60 ± 0.06	1.29	0.86 ± 0.09	1656 ± 521
11	0.75 ± 0.03	1.03 ± 0.06	0.90 ± 0.14	1.26	0.99 ± 0.09	1473 ± 404
12	8.15 ± 0.16	1.81 ± 0.06	1.50 ± 0.06	1.20	--[a]	--[a]
13	0.49 ± 0.03	0.86 ± 0.06	0.77 ± 0.06	1.11	1.16± 0.09	595 ± 141
14	13.1 ± 0.3	2.19 ± 0.06	2.02 ± 0.06	1.09	--[a]	--[a]
15	0.065 ± 0.01	0.52 ± 0.06	0.43 ± 0.18	1.20	--[a]	--[a]
16	1.02 ± 0.04	0.90 ± 0.06	0.86 ± 0.06	1.05	1.12 ± 0.10	1400 ± 394
17	2.50 ± 0.05	1.33 ± 0.06	1.12 ± 0.06	1.15	1.25 ± 0.12	2464 ± 693
18	3.79 ± 0.14	1.50 ± 0.06	1.42 ± 0.06	1.06	1.46 ± 0.10	2322 ± 501
19	1.39 ± 0.10	1.16 ± 0.06	0.90 ± 0.06	1.29	--[a]	--[a]

[a]Diameter and concentration values were not determined (see text).
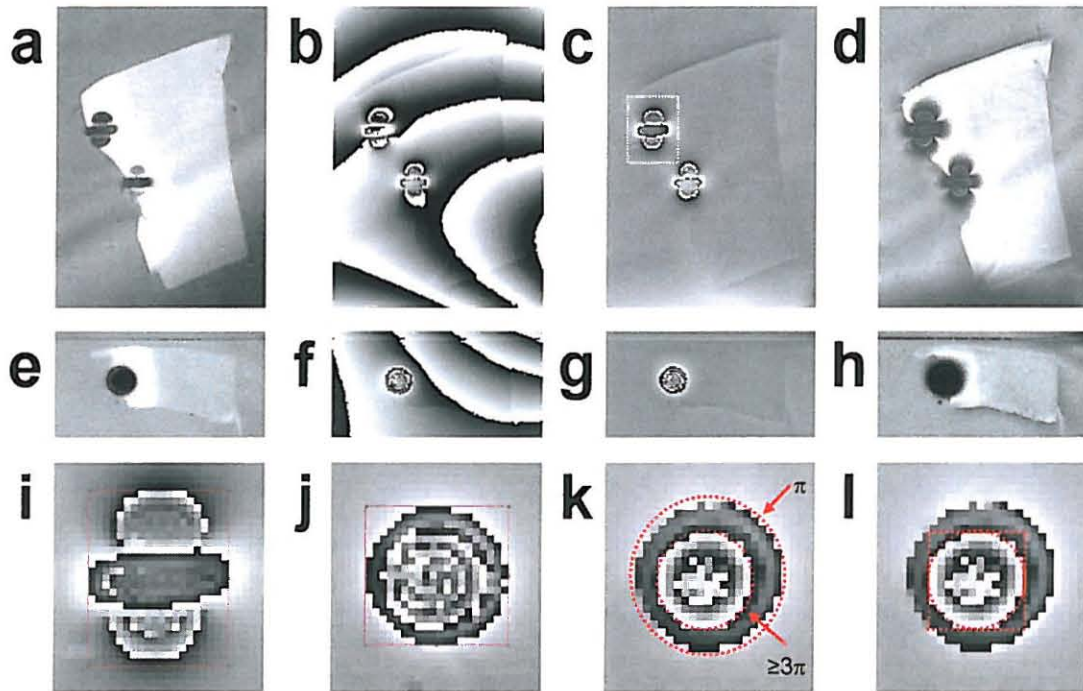
Figure 4.3: SWI of BMB in Postmortem CAA Brain – A & E) Magnitude, B & F) raw phase, C & G) high-pass filtered phase and D & H) phase-enhanced magnitude images of two cortical grey BMB, showing coronal (A - D) and axial (E - H) orientations respectively. The top lesion (dotted rectangle) in panel C is shown in the axial images (E – H). Characteristic dipole patterns were seen in each image. I & J) Bounding rectangles are shown surrounding magnifications (12x) of the top lesion in panel C (dotted rectangle) in coronal (I) and axial (J) orientations (J is a magnification of panel G). K) Magnification of the lower (unmarked) lesion in panel C showing the π phase wrap and an interior hyperintense ring of radius $\geq r_{3\pi}$ (respectively highlighted by red dotted lines). L) The same image as panel K showing a bounding rectangle used to estimate the diameter, d^*, of the inner ring (dotted red lines). The actual lesion diameter d, can be estimated by d^*, and in practice d^* is on average an upperbound to d (see text).

Postmortem Human BMB Data: m_{Fe} vs. $r_\pi'^3$

$$m_{Fe} = 1290\, r_\pi'^3 - 0.309$$
$$R^2 = 0.984$$
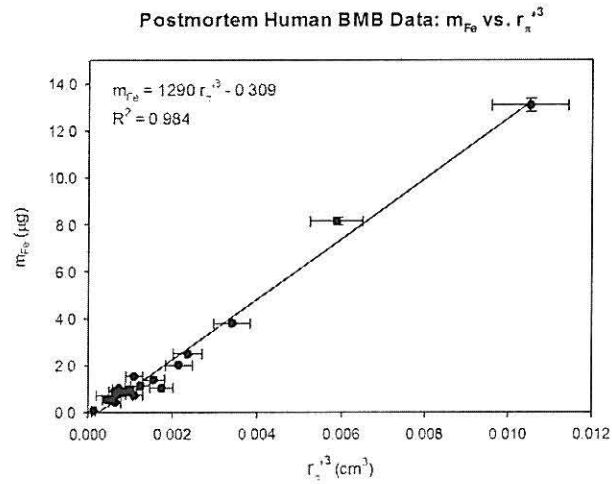
Figure 4.4: BMB Iron Content vs. Image Parameters - Iron mass m_{Fe} is plotted against r_π^3 for N=19 BMB. The graph displays a strong linear relationship ($R^2 = 0.984$, p <0.001) with slope equal to 1290 $\mu g/cm^3$. The small but statistically significant intercept of -0.309 μg (p = 0.021) can be interpreted as an indicator of the sensitivity of the technique. The strong linear relationship is predicted by Eq. 6 and thus confirms the usefulness of this quantification method to measure iron content in actual BMB in human tissue.

119
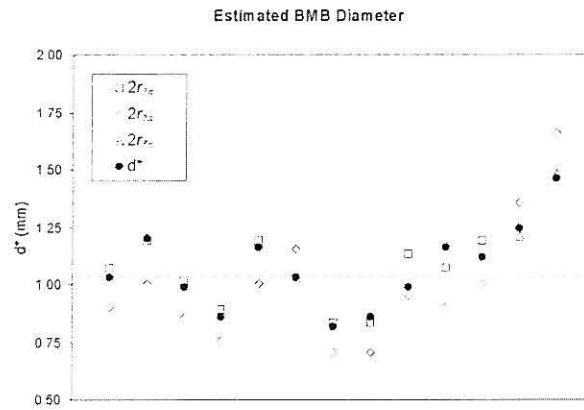
Figure 4.5: Estimated BMB Lesion Diameter Values – Estimated BMB lesion diameters d^*, are shown bounded by phase diameter estimates ($2r_\pi$, $2r_{3\pi}$, and/or $2r_{5\pi}$) for N=13 samples. The lesion diameter estimates are based on dipole phase patterns in axial phase images (Fig 4.3K and L). Phase diameters are calculated from corresponding r_π values. The dotted horizontal line represents the median diameter estimate of 1.0mm.

BMB Iron Concentration
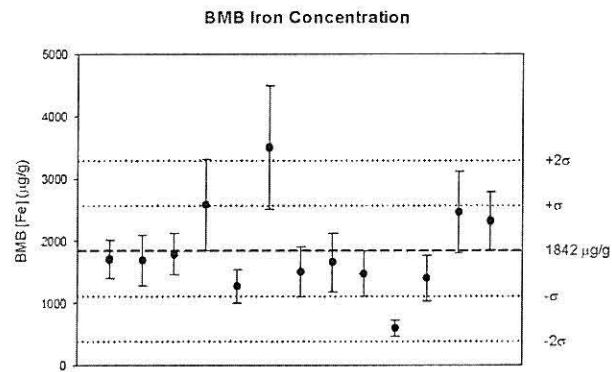
Figure 4.6: BMB Iron Concentration Estimates – A scatter plot showing estimated BMB iron concentrations (N=13). The estimates are normally distributed (W-Statistic = 0.932, p = 0.363). Ten of 13 samples fall within ± 1 standard deviation, and 12 of 13 fall within ± 2 standard deviations about a mean value of 1842 μg/g wet tissue weight.

Discussion

The present study demonstrates that measurements from phase images can be related to iron content in real BMB in postmortem tissue. As discussed below, Fig 4.4 serves as a potential standard curve for human BMB, where r'_π values from filtered phase images can be related to BMB iron mass. The strong linear correlation is predicted by Eq. 6 and validates our quantification method, where the spherical dipole model provides satisfactory results for our BMB samples. In addition, we report estimates of BMB iron mass and concentration based on direct tissue iron measurements and phase image diameter estimates. We used atomic absorption spectrometry (the gold standard for tissue metal concentration measurements) to determine lesion iron content that ranged from 0.065 to 13.1 μg with a median value of 1.0 μg, a range consistent with previous expectations (McAuley et al., 2010a). Lesion diameters were estimated using features of axial dipole phase patterns. The lesion iron concentration was found to be normally distributed with a mean value of 1842±202 μg/g (mean±SEM). Seventy-seven percent and 92% of the BMB sample iron concentrations fell within ± one and two standard deviations about the mean respectively. A normal distribution allows for a simple assessment of disparity between BMB concentrations in different brain regions or diseases. Because higher order phase peaks and wraps were typically obscured in noisy and pixilated dipole centers, these BMB diameters and iron concentrations are on average best regarded as upper and lower bounded estimates, respectively.

BMB are associated with a growing number of disease states and present a source of potentially cytotoxic iron to the brain in proportion to the extent of blood extravasation. Therefore the quantified iron content of BMB is a potential valuable

biomarker to monitor disease progression, treatment efficacy and risk factor assessments. In recent reports: the presence of a single lobar bleed, or more than one lobar bleed fulfill in part the Boston criteria for the diagnosis of possible and probable CAA respectively (van Rooden et al., 2009; Knudsen et al., 2001); two or more baseline BMB is associated with progression from MCI to outright dementia (Kirsch et al., 2009); and BMB $\geq$ 5 was associated with higher risk of ICH than benefit of anti-thrombotic agents (Soo et al., 2008). Such studies are examples where results and clinical interpretations are based on BMB number. However, measurement of iron content as a *continuous* variable goes beyond an assessment of pathologic severity based on presence/absence or a *discrete* number of bleeds. Our method of localized BMB (iron) quantification allows the characterization of severity at the level of a single bleed, groups of bleeds, brain region or whole brain. For example, indices of iron load or disease burden could be defined as "the sum of the iron content for all lobar BMB". Such characterizations could provide advantages over diagnostic criteria, prognostic standards or therapeutic recommendations based on discrete numeric thresholds.

In efforts to improve interrater agreement in BMB detection and capture standardized auxiliary information several investigators have developed systematic BMB rating scales for reliable measures of presence, number, anatomical location, certain/uncertain status, and/or size (Cordonnier et al., 2009; Gregoire et al., 2009). The results of the present study suggest that quantified iron content could enhance the usefulness of such discreet data. We found a wide range of iron content (0.065 – 13.1 µg) for BMB with estimated diameters ranging from 0.82 to 1.5 mm. In addition, BMB with a diameter of 3.2 mm (unbloomed) and iron concentration of 2000 µg/g would

contain ~ 35 μg of iron. Therefore, since our mean iron concentration of 1842 μg/g is probably a lower bound value, in BMB that typically meet rating scale inclusion criteria, iron content may range over two orders of magnitude. This suggests that mere counts may not necessarily be i) a good indicator of bleeding severity (eg, 5 BMB of 1 μg each versus 1 BMB with 15 μg of iron), or ii) a sensitive means for patient and study group comparisons (eg, "number of BMB in the parietal cortex" versus "total iron load of parietal cortex") compared to iron content *per se*.

It is well known that BMB hypointensity size seen in magnitude GRE T2* images are typically larger than the actual tissue lesion. This so called blooming effect varies with field strength, scan parameters and magnetic susceptibility of the source (Pintaske et al., 2006b). Schrag et al., recently reported an average hypointensity magnification factor of 1.57 based on 3T images of 13 lesions in postmortem CAA/AD brains (Schrag et al., 2010). Although a recent *Microbleed Study Group* review recommends the presence of T_2* blooming in BMB identification criteria, it also discourages the use of size characterizations due primarily to the blooming effect (Greenberg et al., 2009). Interestingly, the BOMBS scale (Cordonnier et al., 2009), but not the MARS scale (Gregoire et al., 2009), classify bleeds according to size, because the authors of the latter scale consider size descriptions "may unnecessarily complicate the rating without adding extra useful information" (Gregoire et al., 2009). Results from the present and our recent study (McAuley et al., 2010a) demonstrate that BMB diameter estimation unobscured by the blooming effect is possible in phase images. The Eqs. 4 & 8 further reveal that these determinations can in principle be effectively compared across various field strengths and echo times. Thus, the benefits of size criteria should be revisited. Indeed, for definitions

of iron load indices to be usefully compared between studies or clinical situations, BMB minimum and maximum size limits are necessary. Source dimension quantification in principle allows an objective definition of such inclusion limits.

It had been recognized that automated BMB detection may further improve interrater agreement (Gregoire et al., 2009) as well increase clinical practicality. Mills et al., recently exploited the distinct dipole pattern in coronal phase images to automatically identify and count superparamagnetic iron oxide agents (Mills et al., 2008) in phantoms and rat heart tissue. Results from the present and our recent study underscore that the scale of such dipole templates can be related to iron content (McAuley et al., 2010a). Therefore, using appropriately scaled dipole templates (e.g., varying r'_π and r_π parameters) BMB could potentially be, not only counted but simultaneously their iron content could be quantified. Moreover, BMB could also be classified by size using r_π based diameter estimates or definitions. As described above, estimates could be made from diameters of circles or rectangles best fit to inner phase peak rings in axial filtered phase images (Fig 4.3K and L). The corresponding phase diameters (as defined above) calculated from corresponding r_π values could provide upper and lower bound values to the diameter estimates. Alternately, diameter could be defined based purely on r_π values and used for classification. For example, lesion diameter can be defined as $r_{5\pi}$ based on pertinent knowledge of source properties. Finally, iron or disease load indices could then be calculated from count, location and severity (i.e., iron content) data, and clinically or biologically relevant threshold criteria could flag for further investigation, provide diagnostic information or therapeutic recommendations.

There are several limitations to the present study. First of all, while phase images have several advantages over magnitude images for iron quantification (Haacke et al., 2005; McAuley et al., 2010a) there are some limitations. Phase contrast depends on source geometry and orientation with respect to the main magnetic field, and field perturbations extend beyond sources of susceptibility and alter contrast of surrounding tissue (Shmueli et al., 2009; Schäfer et al., 2009). These effects ultimately arise from fundamental physical properties of the magnetic field (eg, solenoidality) and cannot be fully eliminated. However, unlike quantification of iron in distributed tissue regions (eg, red nucleus), our localized method is significantly less impacted by such effects and actually exploits them: the r_π and r'_π image parameters are related to magnetic field intensity on the directionally dependent dipole pattern outside the localized susceptibility source. Advantage is conferred by 1) providing additional dynamic range in pixilated images allowing resolution of very small sources that could not otherwise be resolved. This range can be increased by increasing echo time provided that the concomitant loss in SNR is not too large. 2) Since parameter measurements occur away from the actual lesion, the shape of the source is less important. In the far-field case, the assumption of a spherically symmetric source greatly simplifies quantification and clinical practicality.

Secondly, our approach assumes background phase has been reduced to negligible levels and this is attempted using high-pass filtering (McAuley et al., 2010a; Wang et al., 2000). Background phase removal is a fundamental problem in phase imaging and several approaches have been attempted (Wang et al., 2000; Neelavalli et al., 2009; Duyn et al., 2007; Cheng et al., 2007). For homodyne filtering, the choice of filter size is often chosen empirically (Szumowski et al., 2010; McAuley et al., 2010a), and the assumed

best practice has been to choose the smallest possible filter size that adequately removes the background (McAuley et al., 2010a). For horizontal images we employed a 16x32 filter. The 2D axial scans however, required a 32x32 filter to yield non-distorted dipoles. The significance of these differing filter sizes, as well as the effects of filtering and filter size in localized dipole sources in general and on accurate comparison of r_π and r'_π values between data sets in particular, are areas where future research is needed.

Third, we have assumed that BMB iron sources are effectively spheres. In most BMB, the actual geometry can likely be ignored because of far field effects. Indeed, this may be reflected in the definition of BMB as "round' hypointense GRE T_2* (magnitude) image features by a recently proposed BMB rating scale (Gregoire et al., 2009). However, other recommendations allow for "ovoid" hypointensities (Greenberg et al., 2009) and it is expected that the spherical geometry assumption may not be globally applicable. However, based on at least three observations, non-spherical effects do not seem to be important in the present study: 1) The average height to width ratio of the π-wrap bounding rectangle in the axial images was 0.99±0.02 (mean±SEM) suggesting circularity in the equatorial plane. 2) The r'_π/r_π ratio for the coronal dipole patterns was consistent with the theoretical value for a spherical source (described above). 3) The plot of m_{Fe} vs. $r'_\pi{}^3$ was strongly linear (Fig 4.4) as predicted by Eq. 6 which is based on the assumption of spherical geometry.

Fourth, our method is a linear model based on the assumptions of uniform iron density and susceptibility. The strong linear correlation between iron mass and $r'_\pi{}^3$ in the present study seems to imply that these BMB iron properties have a relatively small variance. However, because our BMB represent a small number of cases and a specific

127

disease population, future investigation of BMB iron properties in normal and diseased cohorts are necessary before our results can be safely generalized to other tissue states and compared with other studies (McAuley et al., 2010a). For this reason, as well as possible inconsistencies in comparison of r'_π values due to differences in background phase processing (e.g., differing filter sizes) discussed above, the plot of m_{Fe} vs. r'^3_π (Fig 4.4) can only be regarded as a tentative standardization curve of iron content in the postmortem human brain.

Fifth, because sample inclusion before data processing and sample exclusion after processing was based on dipole quality, our results may be biased toward best-case scenarios. However, our study analyzed BMB in postmortem tissue slices and in almost all cases, lesions were visible on the surface of the tissue. BMB dipoles in intact brain will not be influenced by issues and artifacts associated with lesion bisection and cut-tissue interfaces. Therefore, dipoles of comparable iron content could likely be better formed than those excluded in our study. In addition, faint excluded dipoles were associated with iron values at or below the sensitivity threshold of the method (~ 0.3 μg, based on the significant intercept of Fig 4.4), and thus do not actually contribute to a bias. Finally, background phase distortion is less of an issue in clinical scanners when compared to the experimental hardware used in the present study. In any case, how often malformed and ambiguous phase image features occur and to what extent the method is affected must be informed by further research. Moreover, automated image processing software could still possibly discern essential features from dipole patterns that appear indistinct to the human eye.

Finally, the present research was conducted in postmortem tissue with relatively small fields of view (e.g., 2.2 cm) and at very high field 11.7T. Eq. 8 implies in principle that equivalent r_π and r'_π values are achievable even with the clinically state of the art 3.0T magnets. For example, at 3.0T an echo time of 27 ms is required to get dipoles with the same r_π values as this current study (Eq. 8), well within current use in BMB detection (Greenberg et al., 2009; Gregoire et al., 2010). However, practical issues concerning adequate SNR and sufficiently short scan times have yet to be addressed with acquisitions using FOVs that are an order of magnitude larger in typical clinical scans compared with the current study.

In summary, this research demonstrates that real BMB iron content can be accurately related to prominent phase image features under the simple assumption that BMB iron sources are spherically shaped. Our m_{Fe} vs. r'^3_π plot can tentatively be regarded as a standard curve, allowing BMB iron content estimates from similarly processed phase images of tissue states comparable to our AD/CAA autopsy cases. In addition, phase image features were used to estimate upper bounds of BMB iron source diameters and lower bounds of iron concentrations. Our method potentially allows the definition of iron load or disease burden indices from the level of a single bleed to the whole brain (eg "the sum of the iron content of all lobar BMB"), as well as the classification of BMB by size unobscured by the blooming effect. A "count, classify and quantify" method can potentially be fully or semi-automated, and the results can in principle be compared across field strengths and echo times. Such information potentially could enhance prognostic and diagnostic criteria in the context of cerebral

vessel disease and associated late onset dementias, as well as inform treatment decisions regarding the use of thrombolytic or thrombotic agents.

References

Akter M, Hirai T, Hiai Y, Kitajima M, Komi M, Murakami R, Fukuoka H, Sasao A, Toya R, Haacke EM, Takahashi M, Hirano T, Kai Y, Morioka M, Hamasaki K, Kuratsu J-I, Yamashita Y. Detection of hemorrhagic hypointense foci in the brain on susceptibility-weighted imaging clinical and phantom studies. Academic Radiology 2007 14(9):1011-1019.

Atlas SW, Mark AS, Grossman RI, Gomori JM. Intracranial hemorrhage: gradient-echo MR imaging at 1.5 T. Comparison with spin-echo imaging and clinical applications. Radiology 1988 168(3):803-807.

Bizzi A, Brooks RA, Brunetti A, Hill JM, Alger JR, Miletich RS, Francavilla TL, Di Chiro G. Role of iron and ferritin in MR imaging of the brain: a study in primates at different field strengths. Radiology 1990 177(1):59-65.

Cheng Y-CN, Hsieh C-Y, Neelavalli J, Liu Q, Dawood MS, Haacke EM. A complex sum method of quantifying susceptibilities in cylindrical objects: the first step toward quantitative diagnosis of small objects in MRI. Magn Reson Imaging 2007 25(8):1171—1180.

Cordonnier C, Al-Shahi Salman R, Wardlaw J. Spontaneous brain microbleeds: systematic review, subgroup analyses and standards for study design and reporting. Brain: A Journal of Neurology 2007 130(Pt 8):1988-2003.

Cordonnier C, Potter GM, Jackson CA, Doubal F, Keir S, Sudlow CLM, Wardlaw JM, Al-Shahi Salman R. improving interrater agreement about brain microbleeds: development of the Brain Observer MicroBleed Scale (BOMBS). Stroke; a Journal of Cerebral Circulation 2009 40(1):94-99.

Cordonnier C, van der Flier WM, Sluimer JD, Leys D, Barkhof F, Scheltens P. Prevalence and severity of microbleeds in a memory clinic setting. Neurology 2006 66(9):1356-1360.

Dixon WT, Blezek DJ, Lowery LA, Meyer DE, Kulkarni AM, Bales BC, Petko DL, Foo TK. Estimating amounts of iron oxide from gradient echo images. Magnetic Resonance in Medicine 2009;61(5):1132-1136.

Duyn JH, Gelderen Pv, Li T-Q, Zwart JAd, Koretsky AP, Fukunaga M. High-field MRI of brain cortical substructure based on signal phase. Proc Natl Acad Sci U S A 2007 104(28):11796—11801.

Fazekas F, Roob G, Kleinert G, Kapeller P, Schmidt R, Hartung HP. Histopathologic analysis of foci of signal loss on gradient-echo T2*-weighted MR images in patients with spontaneous intracerebral hemorrhage: evidence of microangiopathy-related microbleeds. AJNR Am J Neuroradiol 1999 20(4):637—642.

Gaasch JA, Lockman PR, Geldenhuys WJ, Allen DD, Van der Schyf CJ. Brain iron toxicity: differential responses of astrocytes, neurons, and endothelial cells. Neurochemical Research 2007 32(7):1196-1208.

Greenberg SM, Eng JA, Ning M, Smith EE, Rosand J. Hemorrhage burden predicts recurrent intracerebral hemorrhage after lobar hemorrhage. Stroke 2004 35(6):1415-1420.

Greenberg SM, Vernooij MW, Cordonnier C, Viswanathan A, Al-Shahi Salman R, Warach S, Launer LJ, Van Buchem MA, Breteler MM. Cerebral microbleeds: a guide to detection and interpretation. Lancet Neurology 2009 8(2):165-174.

Gregoire SM, Chaudhary UJ, Brown MM, Yousry TA, Kallis C, Jäger HR, Werring DJ. The Microbleed Anatomical Rating Scale (MARS): reliability of a tool to map brain microbleeds. Neurology 2009 73(21):1759-1766.

Gregoire SM, Werring DJ, Chaudhary UJ, Thornton JS, Brown MM, Yousry TA, Jäger HR. Choice of echo time on GRE T2*-weighted MRI influences the classification of brain microbleeds. Clinical Radiology 2010 65(5):391-394.

Haacke EM, Ayaz M, Khan A, Manova ES, Krishnamurthy B, Gollapalli L, Ciulla C, Kim I, Petersen F, Kirsch W. Establishing a baseline phase behavior in magnetic resonance imaging to determine normal vs. abnormal iron content in the brain. J Magn Reson Imaging 2007 26(2):256—264.

Haacke EM, Brown RW, Thompson MR, Venkatesan R. Magnetic Resonance Imaging, Physical Principles and Sequence Design: Wiley-Liss; 1999.

Haacke EM, Cheng NYC, House MJ, Liu Q, Neelavalli J, Ogg RJ, Khan A, Ayaz M, Kirsch W, Obenaus A. Imaging iron stores in the brain using magnetic resonance imaging. Magn Reson Imaging 2005 23(1):1—25.

Haacke EM, Xu Y, Cheng Y-CN, Reichenbach JrR. Susceptibility weighted imaging (SWI). Magn Reson Med 2004 52(3):612—618.

Igase M, Tabara Y, Igase K, Nagai T, Ochi N, Kido T, Nakura J, Sadamoto K, Kohara K, Miki T. Asymptomatic cerebral microbleeds seen in healthy subjects have a strong association with asymptomatic lacunar infarction. Circulation Journal 2009 73(3):530-533.

Kirsch W, McAuley G, Holshouser B, Petersen F, Ayaz M, Vinters HV, Dickson C, Haacke EM, Britt Iii W, Larsen J, Kim I, Mueller C, Schrag M, Kido D. Serial Susceptibility Weighted MRI Measures Brain Iron and Microbleeds in Dementia. Journal of Alzheimer's Disease 2009 17(3):599-609.

Knudsen KA, Rosand J, Karluk D, Greenberg SM. Clinical diagnosis of cerebral amyloid angiopathy: validation of the Boston criteria. Neurology 2001 56(4):537-539.

Lee S-H, Ryu W-S, Roh J-K. Cerebral microbleeds are a risk factor for warfarin-related intracerebral hemorrhage. Neurology 2009 72(2):171-176.

Maynard CJ, Cappai R, Volitakis I, Cherny RA, White AR, Beyreuther K, Masters CL, Bush AI, Li Q-X. Overexpression of Alzheimer's disease amyloid-beta opposes the age-dependent elevations of brain copper and iron. The Journal of Biological Chemistry 2002 277(47):44670-44676.

McAuley G, Schrag M, Sipos P, Sun S-W, Obenaus A, Neelavalli J, Haacke EM, Holshouser B, Madácsi R, Kirsch W. Quantification of punctate iron sources using magnetic resonance phase. Magnetic Resonance in Medicine 2010 63(1):106-115.

Mills PH, Wu Y-JL, Ho C, Ahrens ET. Sensitive and automated detection of iron-oxide-labeled cells using phase image cross-correlation analysis. Magnetic Resonance Imaging 2008 26(5):618-628.

Neelavalli J, Cheng Y-CN, Jiang J, Haacke EM. Removing background phase variations in susceptibility-weighted imaging using a fast, forward-field calculation. Journal of Magnetic Resonance Imaging: JMRI 2009 29(4):937-948.

Neema M, Arora A, Healy BC, Guss ZD, Brass SD, Duan Y, Buckle GJ, Glanz BI, Stazzone L, Khoury SJ, Weiner HL, Guttmann CRG, Bakshi R. Deep gray matter involvement on brain MRI scans is associated with clinical progression in multiple sclerosis. Journal of Neuroimaging 2009 19(1):3-8.

Pintaske J, Müller-Bierl B, Schick F. Geometry and extension of signal voids in MR images induced by aggregations of magnetically labelled cells. Phys Med Biol 2006b 51(18):4707—4718.

Reichenbach JR, Venkatesan R, Schillinger DJ, Kido DK, Haacke EM. Small vessels in the human brain: MR venography with deoxyhemoglobin as an intrinsic contrast agent. Radiology 1997a 204(1):272-277.

Robson P, Hall L. Identifying particles in industrial systems using MRI susceptibility artefacts. AIChE Journal 2005 51(6):1633-1640.

Schäfer A, Wharton S, Gowland P, Bowtell R. Using magnetic field simulation to study susceptibility-related phase contrast in gradient echo MRI. NeuroImage 2009 48(1):126-137.

Schrag M, McAuley G, Pomakian J, Jiffry A, Tung S, Mueller C, Vinters H, Haacke E, Holshouser B, Kido D, Kirsch W. Correlation of hypointensities in susceptibility-weighted images to tissue histology in dementia patients with cerebral amyloid angiopathy: a postmortem MRI study. Acta Neuropathologica 2010 119(3):291-302.

133

Shmueli K, de Zwart JA, van Gelderen P, Li T-Q, Dodd SJ, Duyn JH. Magnetic susceptibility mapping of brain tissue in vivo using MRI phase data. Magnetic Resonance in Medicine 2009 62(6):1510-1522.

Soo YOY, Yang SR, Lam WWM, Wong A, Fan YH, Leung HHW, Chan AYY, Leung C, Leung TWH, Wong LKS. Risk vs benefit of anti-thrombotic therapy in ischaemic stroke patients with cerebral microbleeds. Journal of Neurology 2008 255(11):1679-1686.

Sveinbjornsdottir S, Sigurdsson S, Aspelund T, Kjartansson O, Eiriksdottir G, Valtysdottir B, Lopez OL, van Buchem MA, Jonsson PV, Gudnason V, Launer LJ. Cerebral microbleeds in the population based AGES-Reykjavik study: prevalence and location. Journal of Neurology, Neurosurgery, and Psychiatry 2008 79(9):1002-1006.

Szumowski J, Bas E, Gaarder K, Schwarz E, Erdogmus D, Hayflick S. Measurement of brain iron distribution in Hallevorden-Spatz syndrome. Journal of Magnetic Resonance Imaging: JMRI 2010 31(2):482-489.

Tanaka A., Ueno Y., Nakayama Y., Takano K., Takebayashi S., 1999. Small chronic hemorrhages and ischemic lesions in association with spontaneous intracerebral hematomas. Stroke. 30, 1637-1642.

Tong KA, Ashwal S, Holshouser BA, Shutter LA, Herigault G, Haacke EM, Kido DK. Hemorrhagic shearing lesions in children and adolescents with posttraumatic diffuse axonal injury: improved detection and initial results. Radiology 2003 227(2):332—339.

van Rooden S, van der Grond J, van den Boom R, Haan J, Linn J, Greenberg SM, van Buchem MA. Descriptive analysis of the Boston criteria applied to a Dutch-type cerebral amyloid angiopathy population. Stroke 2009 40(9):3022-3027.

Vernooij MW, Haag MDM, van der Lugt A, Hofman A, Krestin GP, Stricker BH, Breteler MMB. Use of Antithrombotic Drugs and the Presence of Cerebral Microbleeds: The Rotterdam Scan Study. Arch Neurol 2009 66(6):714-720.

Vymazal J, Klempír J, Jech R, Zidovská J, Syka M, Ruzicka E, Roth J. MR relaxometry in Huntington's disease: Correlation between imaging, genetic and clinical parameters. Journal of the Neurological Sciences 2007 263(1-2):20-25.

Wang Y, Yu Y, Li D, Bae KT, Brown JJ, Lin W, Haacke EM. Artery and vein separation using susceptibility-dependent phase in contrast-enhanced MRA. J Magn Reson Imaging 2000 12(5):661—670.

Xu X, Wang Q, Zhang M. Age, gender, and hemispheric differences in iron deposition in the human brain: an in vivo MRI study. NeuroImage 2008 40(1):35-42.

Yakushiji Y, Nishiyama M, Yakushiji S, Hirotsu T, Uchino A, Nakajima J, Eriguchi M, Nanri Y, Hara M, Horikawa E, Kuroda Y. Brain microbleeds and global cognitive function in adults without neurological disorder. Stroke 2008 39(12):3323-3328.

Zhang W, Sun S-G, Jiang Y-H, Qiao X, Sun X, Wu Y. Determination of brain iron content in patients with Parkinson's disease using magnetic susceptibility imaging. Neuroscience Bulletin 2009 25(6):353-360.

CHAPTER FIVE

IN VIVO IRON QUANTIFICATION IN COLLAGENASE-INDUCED

MICROBLEEDS IN RAT BRAIN

Grant McAuley[1], Matthew Schrag[1], Samuel Barnes[2,4], Andre Obenaus[2,3,5], April Dickson[1], and Wolff Kirsch[1,*]

Neurosurgery Center for Research, Training and Education[1], Biophysics and Bioengineering, School of Science and Technology[2], Non-Invasive Imaging Laboratory, Radiobiology Program[3], Loma Linda University, Loma Linda, CA, USA

Magnetic Resonance Institute for Biomedical Research[4], Detroit, Michigan, USA

Radiology[5], Loma Linda University Medical Center, Loma Linda, CA, USA

*Send correspondence to:
Wolff M. Kirsch
Neurosurgery Center for Research, Training and Education
Loma Linda University,
11175 Campus Street, CPA11113
Loma Linda, CA, 92354
E-mail: wkirsch@llu.edu
Tel: 909-558-7070
Fax: 909-558-0472

Abstract

Brain microbleeds (BMB) are associated with chronic and acute cerebrovascular disease. Because BMB present to the brain a source of potentially cytotoxic iron proportional to extravasated blood, BMB iron content is a potentially valuable biomarker both to assess tissue risk and small cerebral vessel health. We recently reported methods to quantify localized iron sources using phase images that were tested in phantoms and BMB in postmortem tissue. In the present study we applied our method to small hemorrhagic lesions induced in the living rat brain by bacterial collagenase. The expected correlation between measurements of geometric features in phase images and lesion iron content was tested by linear regression and observed in the experimental data. Iron content estimation following BMB in an in vivo rodent model could shed light on the role and temporal evolution of iron-mediated tissue damage and the efficacy of potential treatments in cerebrovascular diseases associated with BMB.

Introduction

Brain microbleeds (BMB) are associated with ischemic and hemorrhagic stroke, cerebral amyloid angiopathy (CAA), neurotrauma, Alzheimer's disease (AD), vascular dementia, cognitive decline, hypertension and age (Cordonnier et al., 2007; Greenberg et al., 2009; Menon et al., 2009; Kimberly et al., 2009; Igase et al., 2009; Jeon et al., 2009; Fazekas et al., 1999; Vernooij et al., 2008; Knudsen et al., 2001; Tong et al., 2003; Tong et al., 2004; Seo et al., 2007; Yakushihi et al., 2008; Kirsch et al., 2010; Stalls et al., 2009; Sveinbjornsdottir et al., 2008). The presence of BMB in ischemic stroke, intracerebral hemorrhage (ICH) and CAA is associated with future hemorrhage (Soo et al., 2008; Jeon et al., 2007; Greenberg et al., 2004; Greenberg et al., 2009). Whether BMB presence increases risk of bleeding with use of thrombolytic and antithrombotic agents is an important and controversial open question (Greenberg et al., 2009; Soo et al., 2008; Vernooji et al., 2009; Lee et al., 2009). Thus, BMB are associated with both chronic and acute illness of no small consequence in of our aging population.

BMB are visible in gradient recalled echo (GRE) T_2* magnetic resonance (MR) imaging as focal regions of signal loss and have been histopathologically related to hemosiderin, the iron-protein complex associated with pathologic iron storage following hemorrhage (Bizzi et al., 1990) and ferritin breakdown (Schenk and Zimmerman, 2004). Hemosiderin is visible in MR images due to it paramagnetic iron content and serves as a marker for BMB (Atlas et al., 1988; Viswanathan & Chabriat 2006). Thus, BMB represent a source of pathologic iron to the brain that is potentially cytotoxic (eg, free radical production through the Fenton reaction), and oxidative damage, iron accumulation and/or iron dysregulation have been implicated in neurodegenerative and cerebrovascular

diseases (Vymazal et al., 2007; Gaasch et al., 2007; Andersen, 2004; Neema et al., 2009; Perez et al., 2008; Smith et al., 1997; Smith et al., 2010). In addition, since iron is deposited at the site of a BMB in proportion to the amount of extravasated blood, iron content in BMB can be considered a marker for the severity of underlying vessel disease (Greenberg et al., 2009). Therefore the quantified iron content in BMB is potentially informative regarding disease progression and the efficacy of treatment (Schenck & Zimmerman 2004, Haacke et al., 2005, Greenberg et al., 2009).

A few studies have compared radiologic BMB to postmortem tissue correlates and have noted evidence of associated tissue damage (Fazekas et al., 1999, Tanaka et al., 1999, Schrag et al., 2010). However, in vivo animal studies would allow investigation of temporal relationships regarding tissue damage evolution following BMB and possible interventions. In particular, studies where BMB iron content levels could be correlated with tissue damage severity and evolution could potentially shed light on the role of iron in the disease process.

We recently proposed a family of techniques to quantify localized iron sources using phase images. The methods have been investigated in MR phantom, postmortem rat and postmortem human systems. In the former cases, iron sources consisted of a hemosiderin mimic (McAuley et al., 2010a, Chapter 3), and in the later case, actual BMB were analyzed (McAuley et al., 2010b). In the present study, we apply similar methods toward iron quantification in the living rat brain using a collagenase induced BMB model.

Methods

Experimental Plan

Critical to the validation of the quantification technique in the living rat brain is the correlation between BMB iron measured by the atomic absorption spectrometer (AAS) and the phase image parameter values that reflect the amount iron "visible" to the MR scanner. Since the AAS machine will measure the total iron in the tissue, perfect correlations can only occur if the imaging is done when all the iron extravasated following the BMB is visible. However, during the time course of the breakdown of blood products, liberation of free iron, hemosiderin formation, etc., the amount of iron visible in the phase images will vary. If one assumes that all the iron, once deposited, is never resorbed or transported but remains indefinitely at the original deposit location, then choosing a very late imaging time points (on the order of months) would be desirable. However, asymptotic release rates, and reports that BMB deposits are not static but dynamic, as well as practical concerns of time and cost require a shorter time point. Based on data regarding the time course of blood product breakdown and iron deposition published in the literature as well as preliminary data, we have chosen a time point of POD 28. Since hematoidin, a marker of free iron release due to hemeoxygenase activity, peaks around POD 10 (Manfred et al., 2004), and hemosiderin deposition peaks around POD 10-14 (Manfred et al., 2004, Bradley, 1993), it can be assumed that total iron as measured by AAS will likely correlate with phase images measurements obtained around POD 28 and further improvements at later time points would be marginal. To insure the best synchrony between the AAS and phase image measurements, the rats were immediately sacrificed after the POD 28 in vivo scan (see below).

Animal Procedures

Our animal protocol was approved by the Loma Linda University Institutional Animal Care and Use Committee. Ten male Sprague-Dawley rats (450-500g) were placed under anesthesia (isoflurane) and positioned in a stereotactic frame (Knopf Instruments, Tujunga, CA). A mid line incision was made on the top of the head and the scalp held back. A small burr hole (~1mm) was drilled into the skull 0.5mm anterior and 3.1±0.2 mm lateral from bregma. A single dose of type VII bacterial collagenase in saline (Sigma-Aldrich, St. Louis, MO) was injected 6.1 mm below the skull surface using a Hamilton syringe (Reno, NV) placed in a microsyringe pump (Model 310 Plus Series, KD Scientific, Holliston, MA). These stereotactic coordinates target the caudate/putamen (CP) of the rat brain. The collagenase doses (0.11U/200 nl saline, 0.14U/200 nl, 0.15U/200 nl, 0.16U/200 nl, 0.17U/200 nl, 0.18U/200 nl, 0.2U/200 nl, 0.22U/200 nl, 0.24U/200 nl saline) were injected over 5 min. An established ICH rat model typically delivers 0.2U of collagenase in 1 µl of saline (Titova et al., 2007; MacLellan et al., 2008). The smaller doses and volumes used in this study reflect an attempt to induce smaller and more localized hemorrhagic legions. To minimize, bleeding of injectate up the needle tract, the needle was held in place for 20 minutes following the injections and then slowly withdrawn at approximately 0.5mm/min. The burr hole was filled with bone wax, the scalp sutured shut, and the rats will be allowed to recover. Following MR scanning (see below) animals were sacrificed by transcardial perfusion with 4% buffered paraformaldehyde (PFA). Brains were extracted from the skull and fixed in 4% PFA.

MR Imaging

Living rats were scanned POD 28±2 in a 4.7T small animal MR scanner (Bruker Biospin, Billerica MA) using two SWI sequences with the following parameters: 1) 3D coronal SWI: TR/TE: 46.5/25 ms (two rats: TR/TE: 39/20 ms), flip angle: 17°, matrix: 256 x 256, NEX: 3, FOV: 3.0 cm, in-plane resolution: 117 μm x 117 μm, and 32 slices of thickness 0.938 mm. 2) 2D axial SWI: TR/TE: 558.3/25 ms (two rats: TR/TE: 1248.8/20 ms), flip angle: 20°, matrix: 256 x 256, NEX: 6, FOV: 3.0 cm, in-plane resolution: 117 μm x 117 μm, slices: 10, 12 or 32 of thickness 0.8 mm.

Lesion Dissection

Coronal cuts were first made in the fixed rat brains anterior and posterior to the needle tract (cortical scar was visible at the top of the brain). Subsequent cuts were made as necessary to reveal the anterior/posterior lesion boundaries and trim away excess tissue. Sections of tissue surrounding the lesion (ipsilateral CP) and control sections (contralateral CP) were dissected out of the coronal slices using a diamond knife and plastic and titanium forceps (Fig 5.1) and weighed on a precision balance.

Iron Content Determination

Samples were wet ashed similar to (Maynard et al., 2002): blocks (20 – 70 mg) were dissolved in 250 μl of 70% HNO_3 overnight, heated at 80°C for 20 min, and allowed to cool to room temperature. 250 μl of 10M of H_2O_2 were added, and after 30 min, samples we heated samples at 70°C for 15 min and allowed to cool. Iron concentrations were measured in triplicate by graphite furnace atomic absorption

spectrometry (SpectrAA 220Z, Varian, Victoria, Australia). Under the assumption that the contra- and ipsilateral CP have identical iron concentrations, lesion iron content was calculated using the formula: $m_{(Fe)L} = f_{(Fe)I}m_I - f_{(Fe)C}m_I$, where $m_{(Fe)L}$ is the mass of iron in the lesion, $f_{(Fe)I}$ ($f_{(Fe)C}$) is the w/w Fe concentration of the ipsilateral (contralateral) tissue block, and m_I is the mass of ipsilateral tissue.
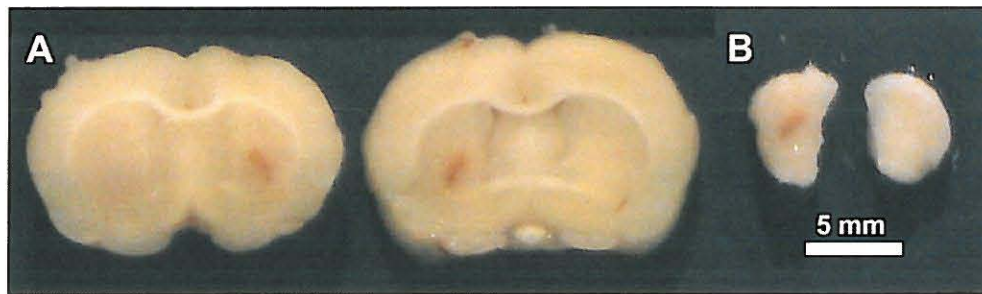
Figure 5.1: Collagenase-Induced BMB – A) Two successive coronal sections of a rat brain with a collagenase-induced bleed in the right CP. Dissected tissue surrounding the bleed (left) taken from the right CP, and a control tissue sample taken from the left CP.

Image Processing

Raw phase images were high-pass filtered using a 16x32 frequency domain filter (Wang et al., 2000) using SPIN software (SPIN software, MRI Institute, Detroit, MI). Magnitude images were multiplied four times by the product of the negative and positive phase mask of reference (Haacke et al., 2004). The image parameter r'_π was obtained from phase dipole patterns using bounding rectangles similar to (McAuley et al., 2010b). However, to eliminate subjectivity where the location of the phase wrap was ambiguous (~ 3 cases), gray-scale images were converted to binary images using ImageJ software before bounding rectangles were drawn (see Fig 5.2).

Statistical Analysis

The predicted proportional relationship between BMB iron mass and r'_π was tested by linear regression analysis using SigmaPlot version 11 (Systat Software, Inc., Chicago, IL). A plot of m_{Fe} vs. r'_π was constructed along with a best-fit least squares regression lines. Statistical significance was considered at $p < 0.05$.
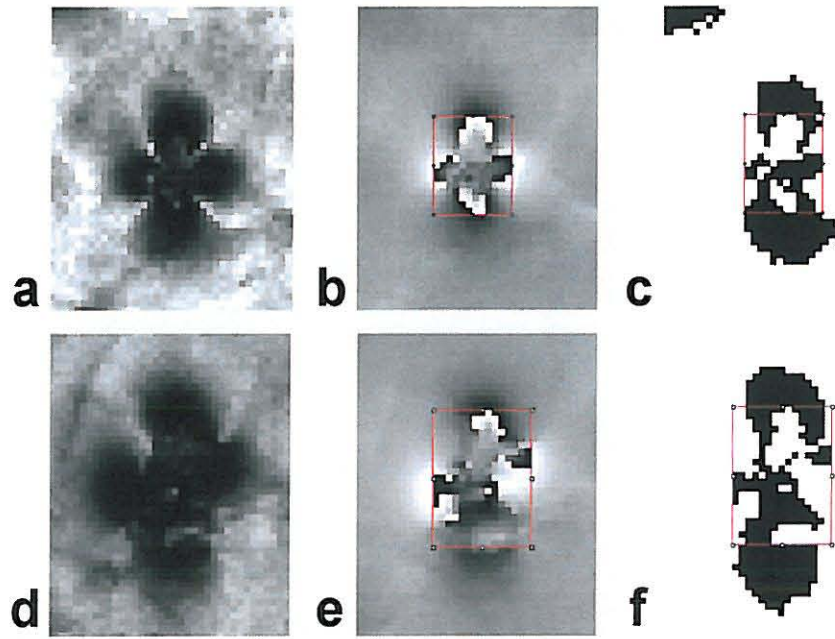
Figure 5.2: Bounding Rectangles in Binary Images – To eliminate subjectivity in drawing bounding rectangles, HP image were converted to binary images before rectangles were drawn. A and D) phase enhanced magnitude images, B and E) HP images, C and F) binary conversions of panels B and E. The top row (panels A, B, and C) show a well formed dipole and the bottom row (panels D, E, and F) a less distinct dipole. Note that in panel B the dipole phase wraps are well defined, whereas the bottom vertical phase wrap in panel E is indistinct. Distinct black/white interfaces in the binary images of panels C and F were used to define the phase wraps and draw the bounding rectangles. The rectangles defined in binary images (C and F) are shown superimposed on the HP images in B and E.

Results

Right circling behavior, left forelimb paresis, and loss of left whisker reflex was observed in varying degrees in rats following recovery from and a few days after surgery, consistent with the lesioning of the targeted caudate/putamen (CP). This was confirmed by MR images which showed lesions present in the CP (Fig 5.3). One animal was euthanized POD 2 due to possible pulmonary embolism and 9 rats were scanned. Dipole patterns were observed in SWI phase, filtered phase, phase mask, phase-enhanced magnitude, and to a lesser extend, magnitude images (Fig 5.3). However, the dipole patterns were generally not as distinct or symmetric compared to our other localized quantification studies (McAuley et al., 2010a, 2010b, Chapter 3). One rat was excluded because the lesion dipole pattern was distorted by background phase and image data from 8 animals were analyzed. Iron mass and image parameter data for these animals are shown in Table 5.1. The median iron mass of the induced BMB for theses animals was found to be 1.40 μg.

Fig 5.4 shows a plot of BMB lesion iron mass vs. $r'_\pi{}^3$. A statistically significant linear relationship is displayed ($R^2 = 0.758$, $p = 0.005$) as expected from the theory underlying the quantification method (McAuley et al., 2010b). The slope is 385 μg/cm^3 ($p = 0.005$) and the intercept while predicted to be zero (McAuley et al., 2010b) is statistically different from zero (0.821 μg, $p = 0.006$). This non-zero intercept can be interpreted as the sensitivity of the method under the current experimental conditions.

Table 5.1: Collagenase-Induced BMB Image Data – Data is shown for collagenase-induced lesions in the CP of the rat brain. Iron mass data was measured using atomic absorption spectrometry. r'_π data was obtained from bounding rectangle dimensions of HP phase images converted to binary image format as discussed in text.

Subject	m_{Fe} (μg)	r'_π (cm)	r'^3_π (cm)
1	1.187	0.1099	0.00133
2	2.194	0.1611	0.00418
3	0.758	0.0938	0.00082
4	1.329	0.0879	0.00068
5	1.465	0.1172	0.00161
6	1.185	0.1172	0.00161
7	1.743	0.1055	0.00117
8	2.409	0.1641	0.00442
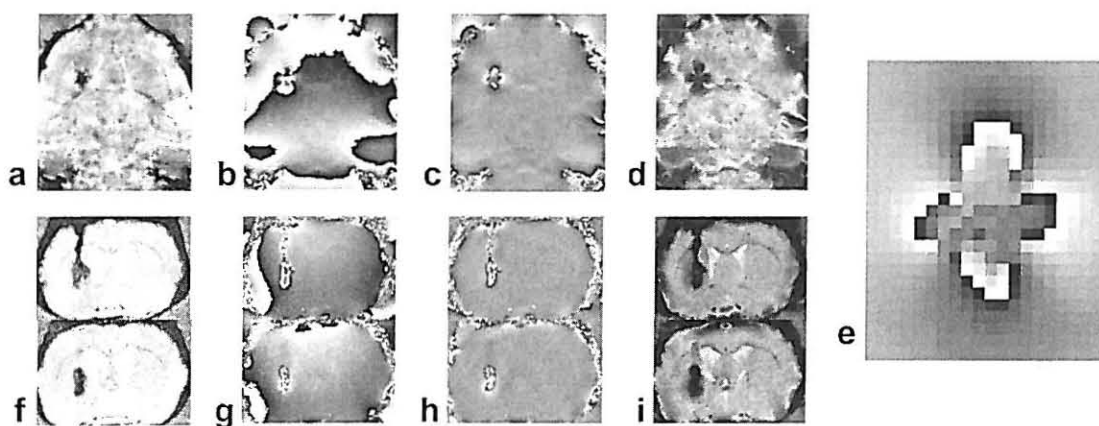
Figure 5.3: In vivo SWI Scan of Collagenase Induced BMB: - In vivo A, F) magnitude, B, G) raw phase, C, H) high pass-filtered, D, I phase-enhanced magnitude SWI images in coronal (A - D) and axial orientations (F - I) of a BMB induced in the caudate/putamen of the living rat brain (subject 1, Table 5.1) (two successive slices are shown for axial images). E) Magnification of the dipole pattern in panel C.

Collagenase Induced BMB Data: m_{Fe} vs. r'^3_-

$$m_{Fe} = 385\ r'^3_- + 0.821$$
$$R^2 = 0.758$$
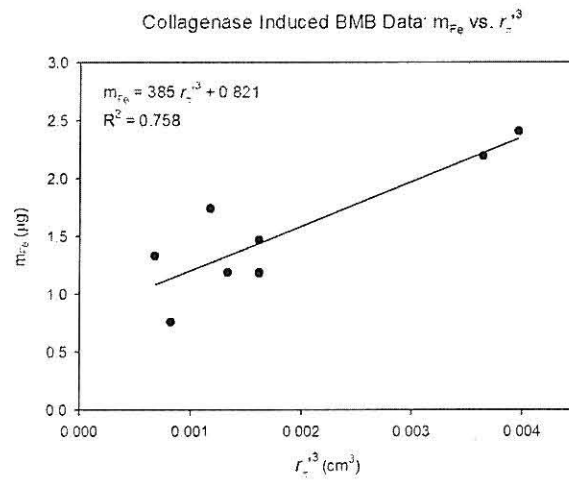
Figure 5.4: Induced BMB Data: m$_{Fe}$ vs. r'^3_π - The iron mass (m_{Fe}) from 8 collagenase-induced BMB is plotted against r'^3_π. The linear relationship ($R^2 = 0.758$, $p = 0.005$) is expected from the mathematical theory underlying the quantification method. The slope is 385 $\mu g/cm^3$ ($p = 0.005$) and the intercept while predicted to be zero is statistically different from zero (0.821 μg, $p = 0.006$).

Discussion

In the present work, we have introduced a simple collagenase-induced BMB model in the living rat brain and used it to test our localized iron quantification technique. The BMB are on the order of a few millimeters in size and contain 0.8 to 2.4 µg of iron. Thus, the size and iron content of the BMB are relevant to human BMB (McAuley et al., 2010b). Dipole patterns, while not as robust as in other studies, are nevertheless present and 8 out of 9 experimentally induced bleeds were measured for the r'_π parameter (McAuley et al., 2010b). A plot of lesion iron mass against r'^3_π produced a linear graph as expected by the theory underlying the quantification technique. This can be thought of as a standard curve whereby other BMB so induced can be assayed for iron content in the rat brain. Examination of Table 5.1 and Fig 5.4 reveals that point pairs 5 and 6, 3 and 4, and 1 and 7, differ in iron mass by ~0.3, 0.5 and 0.6 µg respectively, although their corresponding r'^3_π values differ little or are equal. Thus, the non-zero intercept of ~0.8 µg from the plot of Fig 5.4 provides a reasonable estimate to the sensitivity of the method in the current experiment.

The dipole patterns due to the collagenase induced BMB are not as distinct as seen in the phantoms, ex vivo ferric oxyhydroxide rat brain injections, and human postmortem tissue BMB of our previous studies, and the linear correlations between variables are also not a strong (McAuley et al., 2010a, 2010b, Chapter 3). Because of the complexities associated with clotting, erythrocyte/hemoglobin/heme breakdown, free iron release, iron uptake into ferritin, formation of hemosiderin, etc., these results may not be surprising when compared to our oxyhydroxide model systems (McAuley et al., 2010a, Chapter 3). However, results from our study of BMB in postmortem AD/CAA brain

151

showed substantially better iron content/image parameter correlations and more robust dipoles than we report here (McAuley et al., Chapter 3). These discrepant results are most likely explained by more spatially diffuse lesions in the present study. Indeed, the dipole patterns were less distinct even though lesion iron content was on average larger (all but one lesion > 1 μg, but only 53% > 1 μg in the human study), consistent with less localized iron deposits and magnetic susceptibility source.

There are several factors that could plausibly contribute to more diffuse lesions. If it is assumed that exstravasted iron becomes spatially concentrated over time, then differences compared to postmortem data could be explained by lesion age. A longitudinal study design that extends beyond our POD 28 time point could shed light on how lesion iron accumulation and magnetic properties vary over time. Alternately, a contribution due to differences in rat versus human cerebral vessel density, iron transport mechanisms and physiology is possible. In several rat brains significant MR signal is associated with needle tract locations that extend beyond the localized lesion (e.g., see Fig 5.3). While unlikely to be significant, it is possible that some dipole pattern measurements thus correspond to less than the total iron measured in the CP by the AAS, leading to poorer correlations. However, the primary cause of diffuse lesions is most likely that the injected collagenase is simply causing bleeding over a larger spatial scale then is characteristic of real BMB. Although, the non-spherical shape of the iron deposits seen in our data does not necessarily results in non-robust dipoles (McAuley et al., Chapter 3), it is likely that the more diffuse lesion iron distribution does thus contribute here.

There are two widely used experimental rodent models of intracerebral hemorrhage (ICH) involving injections of autologous blood or bacterial collagenase (Bullock et al., 1984, Rosenburg et al., 1990, MacLellan et al., 2008). While each model has advantages and disadvantages for ICH studies (Belayev et al., 2007; MacLellan et al., 2008), the main goal our surgical procedure was simply to produce localized iron deposits to test our quantification method. The collagenase procedure was advantageous when compared to blood injection since the blood draw step and associated blood coagulation was eliminated. On the other hand, collagenase is thought to result in blood dissecting through the brain parenchyma (MacLellan et al., 2008) which could be counter productive in localized BMB formation. Collagenase ICH rat models typically deliver 0.2U of enzyme in 1 µl of saline (Titova et al., 2007; MacLellan et al., 2008). The smaller collagenase doses and saline volumes used in this study reflect an attempt to induce smaller and more localized hemorrhagic legions that better model BMB. However, it appears that the injected collagenase is causing bleeding over a larger spatial scale then is characteristic of real BMB leading to more diffuse lesions when compared to our postmortem BMB study.

Limitations of our localized phase method have been discussed elsewhere (McAuley et al., 2010a, 2010b, Chapter 3), and here, we have focused on limitations particular to the present collagenase model that lead to less localized lesions. In spite of these limitations, our results have nevertheless demonstrated the potential of our localized quantification technique in the rat brain, and enhanced or alternate models promise to bring more robust dipole patterns and superior results.

153

Improvements could potentially be made to the experimental procedure. To reduce needle trauma and it resulting effects a glass micro needle could be used. Such needles have outer diameters that are an order of magnitude smaller than the 26 gauge needle used in the present experiment (McCluskey et al., 2008). A smaller bore needle tract could lead to less dissection of collagenase and thus more concentrated iron deposits and distinct dipoles. In addition, the use a syringe that allows accurate injection of smaller volumes of injectate could also lead to more concentrated iron deposits. Beside improvements to the current collagenase model, alternate BMB models may offer superior results. One promising approach is the use of ultrashort laser pulses to induce hemorrhages in targeted microvessels (Nishimura et al., 2006).

In conclusion, we have shown that a localized phase image method can potentially be used to estimate localized iron content on the order of micrograms in the living rodent brain using a simple modifications of established collagenase ICH model. Improvements to the experimental technique or the use of alternate bleeding models are expected to produce better results and increase the usefulness of the technique. This potentially will allow investigation of the temporal progression of bleeding lesions and the role of iron-mediated tissue damage and the efficacy of therapeutic interventions in small cerebral vessel disease associated with BMB.

Acknowledgments

References

Andersen, J.K., 2004. Iron dysregulation and Parkinson's disease. Journal of Alzheimer's Disease: JAD 6, S47-52.

Atlas SW, Mark AS, Grossman RI, Gomori JM. Intracranial hemorrhage: gradient-echo MR imaging at 1.5 T. Comparison with spin-echo imaging and clinical applications. Radiology 1988 168(3):803-807.

Bizzi A, Brooks RA, Brunetti A, Hill JM, Alger JR, Miletich RS, Francavilla TL, Di Chiro G. Role of iron and ferritin in MR imaging of the brain: a study in primates at different field strengths. Radiology 1990 177(1):59-65.

Bradley WG., 1993. MR appearance of hemorrhage in the brain. Radiology 189, 15-26.

Bullock, R., Mendelow, A.D., Teasdale, G.M., Graham, D.I., 1984. Intracranial haemorrhage induced at arterial pressure in the rat. Part 1: Description of technique, ICP changes and neuropathological findings. Neurological Research 6, 184-188.

Cordonnier C, Al-Shahi Salman R, Wardlaw J. Spontaneous brain microbleeds: systematic review, subgroup analyses and standards for study design and reporting. Brain: A Journal of Neurology 2007 130(Pt 8):1988-2003.

Fazekas F, Roob G, Kleinert G, Kapeller P, Schmidt R, Hartung HP. Histopathologic analysis of foci of signal loss on gradient-echo T2*-weighted MR images in patients with spontaneous intracerebral hemorrhage: evidence of microangiopathy-related microbleeds. AJNR Am J Neuroradiol 1999 20(4):637—642-637—642.

Gaasch JA, Lockman PR, Geldenhuys WJ, Allen DD, Van der Schyf CJ. Brain iron toxicity: differential responses of astrocytes, neurons, and endothelial cells. Neurochemical Research 2007 32(7):1196-1208.

Greenberg SM, Eng JA, Ning M, Smith EE, Rosand J. Hemorrhage burden predicts recurrent intracerebral hemorrhage after lobar hemorrhage. Stroke 2004 35(6):1415-1420.

Greenberg SM, Vernooij MW, Cordonnier C, Viswanathan A, Al-Shahi Salman R, Warach S, Launer LJ, Van Buchem MA, Breteler MM. Cerebral microbleeds: a guide to detection and interpretation. Lancet Neurology 2009 8(2):165-174.

Igase M, Tabara Y, Igase K, Nagai T, Ochi N, Kido T, Nakura J, Sadamoto K, Kohara K, Miki T. Asymptomatic cerebral microbleeds seen in healthy subjects have a strong association with asymptomatic lacunar infarction. Circulation Journal 2009 73(3):530-533.

Jeon, S.B., Kwon, S.U., Cho, A.H., Yun, S.C., Kim, J.S., Kang, D.W., 2009. Rapid appearance of new cerebral microbleeds after acute ischemic stroke. Neurology 73, 1638-1644.

Kimberly W.T., Gilson A., Rost N.S., Rosand J., Viswanathan A., Smith E.E., Greenberg S.M., 2009. Silent ischemic infarcts are associated with hemorrhage burden in cerebral amyloid angiopathy. Neurology 72(14):1230-1235.

Kirsch W, McAuley G, Holshouser B, Petersen F, Ayaz M, Vinters HV, Dickson C, Haacke EM, Britt Iii W, Larsen J, Kim I, Mueller C, Schrag M, Kido D. Serial Susceptibility Weighted MRI Measures Brain Iron and Microbleeds in Dementia. Journal of Alzheimer's Disease 2009 17(3):599-609.

Knudsen KA, Rosand J, Karluk D, Greenberg SM. Clinical diagnosis of cerebral amyloid angiopathy: validation of the Boston criteria. Neurology 2001 56(4):537-539.

Lee S-H, Ryu W-S, Roh J-K. Cerebral microbleeds are a risk factor for warfarin-related intracerebral hemorrhage. Neurology 2009 72(2):171-176.

MacLellan, C.L., Silasi, G., Poon, C.C., Edmundson, C.L., Buist, R., Peeling, J., Colbourne, F., 2008. Intracerebral hemorrhage models in rat: comparing collagenase to blood infusion. Journal of cerebral blood flow and metabolism : official journal of the International Society of Cerebral Blood Flow and Metabolism 28, 516-525.

Manfred O, Till W, Christoph M, Hans-Jürgen F., 2004. Time Course of Cortical Hemorrhages after Closed Traumatic Brain Injury: Statistical Analysis of Posttraumatic Histomorphological Alterations. Journal of Neurotrauma 20, 87-103.

Maynard CJ, Cappai R, Volitakis I, Cherny RA, White AR, Beyreuther K, Masters CL, Bush AI, Li Q-X. Overexpression of Alzheimer's disease amyloid-beta opposes the age-dependent elevations of brain copper and iron. The Journal of Biological Chemistry 2002 277(47):44670-44676.

McAuley G, Schrag M, Sipos P, Sun S-W, Obenaus A, Neelavalli J, Haacke EM, Holshouser B, Madácsi R, Kirsch W. Quantification of punctate iron sources using magnetic resonance phase. Magnetic Resonance in Medicine 2010a 63(1):106-115.

McAuley G, Schrag M, Barnes S, Obenaus A, Dickson A, Holshouser B, Kirsch W. Iron quantification of microbleeds in postmortem brain. Accepted pending minor revisions in Magnetic Resonance in Medicine 2010b.

Menon, R.S., Kidwell, C.S., 2009. Neuroimaging demonstration of evolving small vessel ischemic injury in cerebral amyloid angiopathy. Stroke; a Journal of Cerebral Circulation 40, e675-677.

Neema M, Arora A, Healy BC, Guss ZD, Brass SD, Duan Y, Buckle GJ, Glanz BI, Stazzone L, Khoury SJ, Weiner HL, Guttmann CRG, Bakshi R. Deep gray matter involvement on brain MRI scans is associated with clinical progression in multiple sclerosis. Journal of Neuroimaging 2009 19(1):3-8.

Nishimura, N., Schaffer, C.B., Friedman, B., Tsai, P.S., Lyden, P.D., Kleinfeld, D., 2006. Targeted insult to subsurface cortical blood vessels using ultrashort laser pulses: three models of stroke. Nature Methods 3, 99-108.

Perez C.A., Tong Y., Guo M., 2008. Iron Chelators as Potential Therapeutic Agents for Parkinson's Disease. Curr Bioact Compd 4, 150-158.

Rosenberg, G.A., Mun-Bryce, S., Wesley, M., Kornfeld, M., 1990. Collagenase-induced intracerebral hemorrhage in rats. Stroke; a Journal of Cerebral Circulation 21, 801-807.

Schenck, J.F., Zimmerman, E.A., 2004. High-field magnetic resonance imaging of brain iron: birth of a biomarker? NMR in Biomedicine 17, 433-445.

Schrag M, McAuley G, Pomakian J, Jiffry A, Tung S, Mueller C, Vinters H, Haacke E, Holshouser B, Kido D, Kirsch W. Correlation of hypointensities in susceptibility-weighted images to tissue histology in dementia patients with cerebral amyloid angiopathy: a postmortem MRI study. Acta Neuropathologica 2010 119(3):291-302.

Smith M.A., Harris P.L., Sayre L.M., Perry G., 1997. Iron accumulation in Alzheimer disease is a source of redox-generated free radicals. Proc Natl Acad Sci USA. 94, 9866-8.

Smith MA, Zhu X, Tabaton M., Liu G., McKeel D.W., Cohen M.L., Wang X., Siedlak S.L., Hayashi T., Nakamura M., Nunomura A., Perry G., 2010. Increased Iron and Free Radical Generation in Preclinical Alzheimer Disease and Mild Cognitive Impairment. J Alzheimers Dis. 19, 363-372.

Soo YOY, Yang SR, Lam WWM, Wong A, Fan YH, Leung HHW, Chan AYY, Leung C, Leung TWH, Wong LKS. Risk vs benefit of anti-thrombotic therapy in ischaemic stroke patients with cerebral microbleeds. Journal of Neurology 2008 255(11):1679-1686.

Staals, J., van Oostenbrugge, R.J., Knottnerus, I.L.H., Rouhl, R.P.W., Henskens, L.H.G., Lodder, J., 2009. Brain microbleeds relate to higher ambulatory blood pressure levels in first-ever lacunar stroke patients. Stroke; a Journal of Cerebral Circulation 40, 3264-3268.

Sveinbjornsdottir S, Sigurdsson S, Aspelund T, Kjartansson O, Eiriksdottir G, Valtysdottir B, Lopez OL, van Buchem MA, Jonsson PV, Gudnason V, Launer LJ. Cerebral microbleeds in the population based AGES-Reykjavik study:

prevalence and location. Journal of Neurology, Neurosurgery, and Psychiatry 2008 79(9):1002-1006.

Szumowski J, Bas E, Gaarder K, Schwarz E, Erdogmus D, Hayflick S. Measurement of brain iron distribution in Hallevorden-Spatz syndrome. Journal of Magnetic Resonance Imaging: JMRI 2010 31(2):482-489.

Tanaka A., Ueno Y., Nakayama Y., Takano K., Takebayashi S., 1999. Small chronic hemorrhages and ischemic lesions in association with spontaneous intracerebral hematomas. Stroke. 30, 1637-1642.

Titova E, Ostrowski RP, Sowers LC, Zhang JH, Tang J., 2007. Effects of apocynin and ethanol on intracerebral haemorrhage-induced brain injury in rats. Clin Exp Pharmacol Physiol Sep 34(9):845-50.

Tong KA, Ashwal S, Holshouser BA, Shutter LA, Herigault G, Haacke EM, Kido DK. Hemorrhagic shearing lesions in children and adolescents with posttraumatic diffuse axonal injury: improved detection and initial results. Radiology 2003 227(2):332—339.

Tong, K.A., Ashwal, S., Holshouser, B.A., Nickerson, J.P., Wall, C.J., Shutter, L.A., Osterdock, R.J., Haacke, E.M., Kido, D., 2004. Diffuse axonal injury in children: clinical correlation with hemorrhagic lesions. Ann Neurol 56, 36—50.

Vernooij, M.W., van der Lugt, A., Ikram, M.A., Wielopolski, P.A., Niessen, W.J., Hofman, A., Krestin, G.P., Breteler, M.M.B., 2008. Prevalence and risk factors of cerebral microbleeds: the Rotterdam Scan Study. Neurology 70, 1208-1214.

Vernooij MW, Haag MDM, van der Lugt A, Hofman A, Krestin GP, Stricker BH, Breteler MMB. Use of Antithrombotic Drugs and the Presence of Cerebral Microbleeds: The Rotterdam Scan Study. Arch Neurol 2009 66(6):714-720.

Viswanathan, A., Chabriat, H., 2006. Cerebral microhemorrhage. Stroke; a Journal of Cerebral Circulation 37, 550-555.

Vymazal J, Klempír J, Jech R, Zidovská J, Syka M, Ruzicka E, Roth J. MR relaxometry in Huntington's disease: Correlation between imaging, genetic and clinical parameters. Journal of the Neurological Sciences 2007 263(1-2):20-25.

Wang Y, Yu Y, Li D, Bae KT, Brown JJ, Lin W, Haacke EM. Artery and vein separation using susceptibility-dependent phase in contrast-enhanced MRA. J Magn Reson Imaging 2000 12(5):661—670.

Yakushiji Y, Nishiyama M, Yakushiji S, Hirotsu T, Uchino A, Nakajima J, Eriguchi M, Nanri Y, Hara M, Horikawa E, Kuroda Y. Brain microbleeds and global cognitive function in adults without neurological disorder. Stroke 2008 39(12):3323-3328.

CHAPTER SIX

DISCUSSION

Summary of Main Results

The purpose of this research project was to develop techniques to quantify the iron content and size of localized brain iron sources using magnetic resonance phase images. The desire to non-invasively quantify iron content and diameter of BMB provides a strong motivation for such research. Each of the four experiments detailed in the preceding chapters provides important contributions toward this goal.

The main results of the phantom studies (Chapter 2) were the expected proportional relationships between the iron mass and radius of the samples and the cube of the r_π parameter. This result is predicted by the theory expounded in Chapter 2 and therefore validates the method. In particular, it shows that iron quantification of the localized source can be carried out in two ways: using the equations underlying the curves (Chapter 2, Eqs. 5 and 7) with appropriate knowledge of the equation parameters, or using the curves themselves as standard curves (Chapter 2, Fig 2.4A and B). A key to the success is the application of high pass filtering that attempts to separate the true dipole signal representing the iron susceptibility source from background phase artifacts. In addition, the sample iron mass and diameter fell in ranges relevant to real BMB, and the method was able to resolve iron mass differences at a level also relevant to BMB. These 'proof of concept' results demonstrated that quantification of iron content and

diameter of localized sources relevant to BMB is feasible at least under idealized conditions.

The postmortem rat Ch-Fe injection experiments (Chapter 3) sought to investigate iron quantification of non-spherical sources in real tissue. This work represents a step away from the ideal phantom world to presumably a more realistic context. In the phantom experiments, the Ch-Fe samples were assumed and carefully and successfully prepared (Chapter 2, Fig 2.2) to be spherical. Ch-Fe injections resulted in non-spherical sources (Chapter 3, Fig 3.4). A sophisticated mathematical theory was presented based on confocal ellipsoidal coordinates and ellipsoidal dipole analogs to extend and generalize the localized quantification method based on one phase image parameter (r_π) to three parameters (a_π, b_π, and c_π). In addition to horizontally oriented coronal images, information gained from axially oriented images is required by the method. The cylindrical symmetry induced in the main field ($\mathbf{B_0}$) direction further required the use of a numerical method to calculate an undetermined ellipsoidal radius (a_π, or b_π depending on the orientation of the ellipsoid with respect to B_0) (Chapter 3, Fig 3.3). While experimental data appears consistent with theoretical expectations (Chapter 3, Fig 3.7A), unverified assumptions of the method, inconsistencies in theory and simulations (at least in Case 2) do not allow verification of the method as it currently stands. Investigation into these issues is ongoing and thus the triaxial method described in this chapter is considered a work in progress. However, an unexpected but very important result from Chapter 3 was the strong linear relationships in simulation and experimental data after application of essentially spherical methods (Chapter 3, Fig 3.5B – D, Fig 3.7B – D). The implications of this are very important when considering possibly non-spherical

BMB. Although elegant and promising in certain contexts, the triaxial ellipsoidal method is complex and relies on certain assumptions that may significantly limit useful application to real BMB (discussed below). Therefore, a simple spherical method is much more appealing. The use of α'_π was considered to be the best choice for a spherical method because of its increased dynamic range compared to h_π and v_π.

In the postmortem human BMB experiments of Chapter 4, localized quantification in phase images of real BMB in AD/CAA brain was investigated. Similar to the previous experiments, the plot of iron mass against r'^3_π showed an expected linear relationship (Chapter 4, Fig 4.4) predicted by theory. The strong relationship was important for at least three reasons. First of all, it suggested that a spherical assumption may be adequate in analyzing images of real BMB. Secondly, it showed that the linear assumption (i.e., constant iron source density and magnetic susceptibility) may also be sufficient, at least for the limited number of autopsy cases in the study. Thirdly, the plot (Chapter 4, Fig 4.4) can be regarded as standard curve for iron content estimation that can be at least tentatively applied to a similar disease population. Thus, it is the first possible application of the method to real BMB data. For the first time in the literature BMB iron content (i.e., mass) has been reported at least for "fractional BMB"[2], as well as non-invasive estimates of iron concentration and true lesion diameter (i.e., unobscured by the blooming effect). The iron mass was measured by atomic absorption spectrometry, which is considered a gold standard for measurement of metal content. Diameters were estimated based on a novel method using the diameter of the inner-most hyperintense

---

[2] Because the majority were visible on cut tissue surfaces, we may refer to our lesions as "fractional BMB". Therefore, technically iron content in analogous intact lesions is likely higher on average, and our reported values can be considered order of magnitude lower bound estmates of typical BMB. This minor detail was not appreciated at the time when the paper of Chapter 4 was submitted and does not alter significant results.

ring in axial images as the best estimate for the lesion diameter. In addition, the phase

diameters were defined (e.g., $r_{3\pi}$, $r_{5\pi}$, etc.) based on the phase wraps observed in the

images. The phase diameters can be used as bounds to the best diameter estimates, or can

provide an objective *definition* of lesion "diameter". Importantly, these diameter and

concentration estimates do not depend on a knowledge of source density or susceptibility.

However, signal to noise ratio and pixelization will ultimately limit the resolution of the

estimates.

Finally, the collagenase induced BMB experiments (Chapter 5) sought to apply

localized iron quantification to an in vivo animal model. A plot of iron mass against r'^3_π

confirmed significant linear relationships between variables (Chapter 5, Fig 5.3).

However, compared to the other experiments the relationship was weaker. In addition,

although lesion iron content was on average greater than in the human study, dipole

patterns in phase image at 4.7T were not as distinct as the other studies. Nevertheless, it

is the first report of a collagenase -induced BMB animal model, and the first investigation

of localized iron quantification using dipole properties of phase images in the rat brain.

Despite the limitations, our results show that phase image methods can potentially be

applied for localized in vivo quantification in the living rodent brain.

In addition to individual contributions, the completed four experiments

complement each other. For example, comparing Table 2.1 of Chapter 2 and Table 4.1 of

Chapter 4, it can be seen that the Ch-Fe sample diameters and radii are not just

theoretically relevant to real BMB as discussed in Chapter 2, but are indeed relevant. In

addition, the slopes of the phantom and human iron mass curves (Chapter 2, Fig 2.4A and

Chapter 4 Fig 4.4, respectively) can be compared using Eqs. 4 and 5 of Chapter 4 to

convert between r_π and r'_π. The phantom slope is 2810 µg/cm^3 whereas the corrected human slope is of the same order of magnitude and becomes 3612 µg/cm^3. This implies that the mass susceptibility of the BMB ($\Delta\chi/\rho$) is smaller than that of the Ch-Fe. Therefore, the concentration of the Ch-Fe solution used to make the phantoms can potentially be diluted to match this mass susceptibility.

Significant of Results

Taken together these four experiments represent a body of knowledge pertinent to localized iron quantification in general and to BMB in specific. While more work remains to be done, this research lays a foundation for non-invasively measuring localized iron content, iron source diameter, and source iron concentration. Because the dipole patterns are easy to identify in the presence of noise, our methods can potentially be automated (Mills et al., 2009) (discussed below). Therefore, in combination, one can potentially identify a MR image feature based on a dipole pattern(s), count the number of such features in the image, estimate the effective diameter or volume of the source, classify each identified feature using the size information, classify each feature based on position in the image or in relation to other features, quantify the amount of iron in each source, and finally calculate a pertinent index based on this data (eg, the total amount of iron in all BMB greater than 1 mm in diameter but less than 5 mm in diameter located in the temporal lobes"). In short, an automated "count, classify, and quantify" scheme is possible.

163

Clinical Relevance

BMB are associated with ischemic and hemorrhagic stroke, cerebral amyloid angiopathy (CAA), neurotrauma, Alzheimer's disease (AD), vascular dementia, cognitive decline, hypertension and age (Cordonnier et al., 2007, Greenberg et al., 2009, Menon et al., 2009, Kimberly et al., 2009, Igase et al., 2009, Jeon et al., 2009, Fazekas et al., 1999, Vernooij et al., 2008, Knudsen et al., 2001, Tong et al., 2003, Tong et al., 2004, Seo et al., 2007, Yakushihi et al., 2008, Kirsch et al., 2010, Stalls et al., 2009, Sveinbjornsdottir et al., 2008). The presence of BMB in ischemic stroke, intracerebral hemorrhage and CAA is associated with future hemorrhage (Soo et al., 2008, Jeon et al., 2007, Greenberg et al., 2004, Greenberg et al., 2009). Whether there is an increased risk of bleeding associated with thrombolytic and antithrombotic agents when BMB are present is an important open question (Greenberg et al., 2009, Soo et al., 2008, Vernooji et al., 2009, Lee et al., 2009). Thus, BMB are seen to be associated with both chronic and emergency illness of significant social and economic impact, especially in light of our aging population.

Because BMB present a source of potentially cytotoxic iron to the brain proportional to extravasated blood, the quantified iron content of BMB is potentially a valuable biomarker (Schenck & Zimmerman 2004, Haacke et al., 2005, Greenberg et al., 2009). As discussed in Chapter 4, recent reports in the literature have used BMB number as the basis for clinical interpretation. However, measurement of iron content as a *continuous* variable goes beyond an assessment of pathologic severity based on presence, absence or count of a *discrete* number of bleeds, and potentially allows the characterization of severity at the level of a single bleed, groups of bleeds, brain region or

164

whole brain. For example, indices of *iron load* or *disease burden* could be defined as e.g. "the sum of the iron content for all lobar BMB". The extent of the added value and clinical usefulness of such characterizations in relation to diagnostic criteria, prognostic standards or therapeutic recommendations merits further study.

Several investigators have developed systematic BMB rating scales for reliable measures of presence, number, anatomical location, certain/uncertain status, and/or size (Cordonnier 2009, Gregoire 2009). Results of the present study suggest that quantified iron content could add value to such discreet data sets. For example, total iron load as opposed to number of "certain BMB in the parietal cortex" could be compared between subjects of a study.

It is well known that BMB hypointensities seen in magnitude GRE T2* images typically appear larger than the actual tissue lesion. This so called blooming effect varies with field strength, scan parameters and magnetic susceptibility of the source (Pintaske et al., 2006b, Bos et al., 2003). Schrag et al., recently reported an average hypointensity magnification factor of 1.57 based on 3T images of 13 lesions in postmortem CAA/AD brain (Schrag et al., 2010). Although a recent *Microbleed Study Group* review recommends the presence of T2* blooming in BMB identification criteria, it also discourages the use of size due primarily to the blooming effect (Greenburg et al., 2009). The BOMBS rating scale (Cordonnier et al., 2009), but not the MARS rating scale (Gregoire et al., 2009), classifies BMB according to size. The MARS scale authors' remark that size descriptions "may unnecessarily complicate the rating without adding extra useful information" (Gregoire et al., 2009). However, results from Chapter 2 and particularly Chapter 4 demonstrate that BMB diameter can potentially be measured,

estimated or defined in phase images unobscured by the blooming effect (McAuley et al., 2010a, 2010b). Further, Eqs. 4 & 8 from Chapter 4 reveal that these determinations can in principle be compared across field strengths and echo times. With this new found ability, the benefits of size criteria should be revisited. Indeed, for definitions of iron load indices to be usefully compared between studies or clinical situations, BMB minimum and maximum size limits are necessary. Source dimension quantification in principle allows an objective definition of such inclusion limits.

Relevance to Basic Science

Another possible area of application of the proposed quantification methods is in animal models of microvascular disease. For example, therapeutic agents could potentially be tested by monitoring BMB iron load following treatment, or the temporal evolution of iron mediated tissue damage could be followed. Chapter 5 shows that bleeding lesion dipole patterns are visible and quantifiable in the rodent brain following iron deposition on the order of 1 μg (Chapter 5, Table 5.1). Application of the proposed methods to other animal models of bleeding (Winkler 2001, Nishimura et al., 2006) would also be of interest. In addition, magnetically labeled cell tracking methods could potentially benefit from the quantification methods of the present research (McAuley et al., 2010a). Diameter estimates may shed light on cell division status, removal of blooming could provide more precise information on cell cluster location relative to anatomic structures, and localized iron content may shed light on labeled cell number.

166

Relevance to Industry

The methods described in this dissertation could also find application in industrial applications. While we have focused on iron quantification, the methods are generally applicable to other sources of susceptibility. Investigation into MR based identification, distribution, and discrimination of objects and materials have been reported (Robson and Hall et al., 2005) and may benefit from the present work. For example, the ellipsoidal frame work of Chapter 3 covers several shapes including spheres, disks, rods and general ellipsoids and may find use in applications where the orientation and/or shape of scanned objects is known.

Relation to Literature

As the title of this dissertation suggests the essence of this research concerns quantification of localized iron sources using MR phase images. We exploit the dipole pattern in the phase image analysis. Eq. 1 of Chapter 2 implies that the dipole phase is proportional to the perturbation in the local magnetic field. In simple terms, these means looking at the phase is essentially looking at the magnetic field. The local field is altered by an iron source because of the magnetic field induced in it by the main field magnet of the MRI system. The extent to which a field can be induced in a material is quantified by its magnetic susceptibility.

The relationship between susceptibility and phase has been exploited in several studies. Oxygen dependent susceptibility differences were used to separate arteries and veins (Wang et al., 2000). Unwrapped phase maps have been used to obtain iron susceptibility measurements in gerbil cardiac tissue however, the calculation was

167

complicated by constant phase term (hyperfine contact shift) (Wang et al., 2005). The high pass filtering used in the present study beneficially removes constant phase terms and the resulting complications of data analysis. Cheng et al., used a more complicated summation of the complex MR signal (i.e., with respective real and imaginary magnitude and phase components) that uses most surrounding pixel information to quantify the susceptibility of cylindrical phantoms (Cheng et al., 2007). Several other authors have studied MR dipole properties (Pintaske et al., 2006a, Bos et al., 2003, Kim et al., 1993, Pintaske, et al., 2006b) including application to phase images (Robson and Hall, 2005, Dixon et al., 2009, Mills et al., 2008). The former two are now discussed in more detail.

While there are no reports (to the best of my knowledge) to quantify localized iron sources in brain *per se*, there are a few reports that studied localized susceptibility effects (including due to iron) outside of the brain exploiting dipole patterns in phase images. Some of the concepts described in these studies that are relevant and influential to the present study were understood independently by the dissertation author. However, citation and credit is appropriately given to these studies because they appear first in the literature.

The mathematical theory of the method discussed in the phantom study (Chapter 2) is based on well know physics and the r_π image parameter. While the concept of r_π was understood independently (but several years later) by the dissertation author, the r_π parameter was first reported in the literature by Robson and Hall in 2005 (Robson and Hall, 2005). It was measured from dipole patterns in phase images due to cylinders of varying magnetic susceptibility (cylinders filled with air or a manganese chloride solution) and used to compare experimental and theoretically predicted magnetic

168

moments. Since magnetic moments are proportional to products of geometric parameters (eg, radius of spheres) and susceptibility, determining magnetic moments in known localized geometry (such as spheres) is essentially localized quantification. Thus, in a fundamental way, the theory for localized quantification and determining source diameter from phase image underlying this project was in essence described by Robson and Hall (Robson and Hall, 2005). However, their predicted magnetic moments based on experimentally measured r_π value did not reliably match theoretical calculations for larger magnetic moments, and they reported that "Thus, although it is possible to measure the dipole moment of an object using MRI, such measurements do not give a reliable value; …". This could possibly be explained by inadequate background phase removal due to the empty scanner subtraction technique they employed. However, sample magnetic moments in the phantom study are much smaller than theirs, so direct comparison with our study may not be fully straight forward. In any case, the results of Chapter 2 are reliable over the full range of iron masses reported and thus represent a *successful* demonstration of the feasibility of quantification of localized iron content and source diameter using phase image parameters such as r_π. In addition, by assuming a constant density and magnetic susceptibility, and using spherical geometry, the present research formulates the quantification method slightly differently than the Robson and Hall study. Under these conditions, a simple linear model is constructed that relates iron mass to r_π^3. In practice, the iron sources can be regarded as having similar physical and magnetic properties, and small variations of these properties are somewhat "averaged out" when the slope of the line assumed to relate them is determined. A main advantage of the linear model is its simplicity.

169

Dixon et al., attempted to predict the known iron mass of in three injections of iron oxide into muscle in two postmortem rat legs (Dixon et al., 2009). The localized sources, which were apparently not spherical, were analyzed using phase images. Dipole patterns from an assumed point source were fit using a least squares method to the actual phase distribution surrounding the non-spherical iron oxide injections. The results comparing known and experimental estimates (three samples) were not consistent, possibly because the method used to remove background phase was not adequate, or that the point source dipole pattern did not adequately represent the true geometry of the source. In the present research, dipole feature measurements in phase images were shown to be consistently linearly related to iron mass for 22 iron oxy-hydroxide samples (Chapter 2 phantom and Chapter 3 postmortem rat brain Ch-Fe injections), and 27 actual bleeding lesions (Chapter 4, in postmortem human, and Chapter 5, in living rat brain).

In the present experiments, we used high-pass homodyne filtering to remove background phase effects. These effects can confound the dipole signal so that phase and phase parameters (e.g., r_π) are not measuring the dipole signal alone, leading to inaccurate results. The use of high pass filtering could in part explain our success compared to (Robson and Hall, 2005) and (Dixon et al., 2009). In addition, in the phantom paper we discuss the need of adequate background removal, and complete removal is stated as an assumption in the theory of our method. The phantom paper also provides a somewhat thorough mathematical, physical, and image processing description of an r_π method applied to a localized spherical source. Finally, in Chapter 3 we expand the phase image parameter approach by introducing extensions to the r_π parameter for use with ellipsoidal geometries (a'_π, b^*_π, a_π, b_π, and c_π), and in Chapters 4 and 5 we use the

r'_π parameter in quantification. Thus, the present research elaborates and expands upon, as well as successfully uses, the concepts published by Robson and Hall and Dixon et al.

Novel Contributions

Novel contributions of the research presented in this dissertation are now briefly summarized and listed: 1) The present research successfully demonstrated the feasibility of quantification of A) iron content, and B) effective diameter of localized iron sources. 2) High-pass filtering of phase images was incorporated into a localized method to remove confounding background phase. 3) While a work in progress, in the triaxial method of Chapter 3, A) the spherical method was extended to non-spherical sources, using B) multiple phase image orientations, C) an ellipsoidal mathematical formulation, D) numerical methods, E) a'_π, $b*_\pi$, a_π, b_π, and c_π measurements, to relate image parameters to iron content. 4) The parameter r'_π was used in a spherical method providing better dynamic range in a pixilated environment compared to r_π. 5) Results from Chapter 4 suggest that our method with a simple spherical assumption may be effectively applied to postmortem human BMB. 6) We report lower bound iron content of BMB from AD/CAA postmortem brain based on AAS measurements. 7) We introduce an alternate method to estimate localized source diameter based on geometry alone and without requiring knowledge of source susceptibility or density, or the use of a standard curve. 8) We report upper bound estimates of diameter in real BMB and lower bound real BMB iron concentration estimates. 9) We present a tentative standard curve for image parameter based iron content estimation in real AD/CAA postmortem BMB. 10) We introduce a collagenase-induced BMB rat model, and 11) demonstrate the

171

feasibility of our method for localized iron content estimation in the rodent brain. 11) We introduce a rectangle based method to measure phase image parameters (e.g., r_π, d^*). 12) We introduce the use of the Ch-Fe material as a mimic of hemosiderin. 13) We report a technique to make very nice spherical samples of known iron content in MR phantoms.

Potential Automation

It had been recognized that automated BMB detection may further improve interrater agreement (Gregoire et al., 2009). In addition, while researchers may have time to identify BMB over several days (Ahaz et al., 2010) clinicians do not have this luxury. Moreover, the image and data processing time involved in our methods is time intensive. Therefore, for such techniques to be widely applicable in a clinical setting, full or semi-automation is probably necessary.

Mills et al., recently exploited the distinct dipole pattern in MR phase images to automatically identify and count SPIO agents (Mills et al., 2008). Our results suggest that the scale of such dipole templates can be related to the iron content of the dipole source. In other words, because the vertical distance from the dipole template center to the π-wrapping interfaces is equal to r'_π, matching a template dipole to a source dipole pattern effectively determines its iron content. Diameter information can similarly be determined in axial phase images. Therefore, using appropriately scaled dipole templates (eg, varying r'_π and r_π parameters) BMB could potentially be not only identified and counted as reported in (Mills et al., 2008), but simultaneously their iron content and diameter could be estimated. This is the basis for the "count, classify, and quantify" method proposed above.

172

Limitations

There are several limitations in this project and to our quantification methods.

Limitations to Phase Images

While possessing several advantages over magnitude images for iron quantification (Haacke et al., 2005, McAuley et al., 2010a) phase image approaches also have limitations. Phase contrast depends on source geometry and orientation with respect to the main magnetic field. In addition, field perturbations extend beyond sources of susceptibility resulting in the altered contrast of surrounding tissue (Shmueli et al., 2009, Schäfer et al., 2009). These effects of non-locality and directionally -dependent contrast ultimately arise from the fundamental physical nature of the magnetic field (e.g., solenoidality) and cannot be fully eliminated. However, our method actually uses these properties to quantify iron in local sources. Image parameters are related to magnetic field intensity on the directionally dependent dipole pattern outside the localized source. Advantage is conferred by providing additional dynamic range in pixilated images. This allows resolution of very small sources that would not be otherwise resolved. This range can be increased by increasing echo time provided that the concomitant loss in SNR is not too large.

Assumed linearity

Our method is a linear model based on the assumptions of uniform iron density and susceptibility. In the postmortem human experiment of the present study (Chapter 4), the very good linear correlation between iron mass and r'_π seems to imply that these

BMB have a relatively small variance. However, because our BMB represent a small number of cases and a specific disease population, it is not possible to draw conclusions about BMB in general. Therefore, at best the plot of Chapter 4, Fig 4.4 can only be regarded as a tentative standard curve. Values of BMB iron density and susceptibility in normal and diseased cohorts have not been reported in the literature. Such work will be necessary before our results can be safely generalized and compared with other studies. More fundamentally, whether iron densities and susceptibilities vary with a narrow distribution and generally allow the application of the linear model remains to be determined.

Background Phase

Our approach assumes background phase has been reduced to negligible levels. Background phase removal is a fundamental problem in phase imaging and several approaches have been used, including: estimating phase from modeled susceptibility sources (Neelavalli et al., 2009), numerical smooth and fit techniques (Duyn et al., 2007) (Duyn et al., 2007), simple subtraction (Cheng et al., 2007), and homodyne high pass filtering (Wang et al., 2000). Since phase dipole patterns are the result of aliasing, all but the latter method necessitate an additional phase unwrapping step before background removal, and this was a major reason we originally chose the filtering approach in our phantoms. In all our experiments (Chapters 2 – 5) the expected linear relationships were observed, and as discussed above, the use of the HP filtering is assumed to be a significant element to in the success of our method when compared to other studies involving localized susceptibility sources. However, filtering size was determined

empirically and differed between, e.g., the phantom experiments (32x32) and postmortem human (16x32 filter).

Several important questions surrounding filtering associated with localized susceptibility sources merit further study. For example, to what extent do differing filter sizes affect the consistency of iron quantification results within and between studies? What is the most effective way to optimally and objectively choose a filter size? Are alternate methods of background removal superior to filtering? These, and other related questions, must be addressed by future research before our localized methods can be widely applied with confidence.

Practical Limitations

The present research was conducted in using very small fields of view (2.2 – 3 cm) and mostly at very high field 11.7T. Eqs. 4, 5, and 8 of Chapter 4 imply in principle that equivalent r_π and r'_π values are achievable even with the clinical state of the art 3.0T magnets. For example, at 3.0T an echo time of 27 ms is required to produce dipoles with the same r'_π values as in the postmortem human study of Chapter 4 (Eq. 8), a value well within current use in BMB detection (Gregoire et al., 2010, Greenburg et al., 2009). However, practical issues concerning questions of adequate SNR and sufficiently short scan times have yet to be addressed with acquisitions using FOVs that are an order of magnitude larger than in the current study.

Idealization Bias

In our postmortem human (Chapter 4) and in vivo rat brain (Chapter 5) studies, BMB were excluded from analysis because associated phase dipole patterns were deemed too faint, distorted or altered by background phase to give reliable results. Therefore, our results may be biased toward best-case scenarios. In practice, whether in a clinical or experimental context, malformed and ambiguous phase image features are likely to present. How often these cases occur and to what extent the overall utility of the method is affected must be informed by further research. However, it is likely that an automated computer pattern recognition approach could prove more effective than human judgment in ambigous cases. At least such approaches could be designed to include objective criteria that could be consistently applied across data sets. For example, subtle pixel intensity gradients could be employed to determine π-wrapping points when no distinct phase jump appears to be present, or scaled dipole templates could be correlated with actual dipole pattern pixels similar to the method reported by Mills et al., (Mills et al., 2008) to determine dipole phase pattern parameters. Curve-fitting algorithms could be applied to hyperintense phase rings to give best fit estimates of the source diameter. Finally, it is possible that certain distorted dipole patterns are actually superpositions of two or more susceptibility sources. Methods that seek to analyze irregularly shaped images by composition/decomposition in constituent parts (e.g., individual dipoles of varying sizes) might be helpful in such cases.

Future Work

There are several aspects of this research dissertation that appear very promising. However, many results represent initial steps and more work will be needed before the extent of the usefulness of the localized quantification methods is clearly seen. The *Limitations* section suggests that more work is required before the method can reliably be applied in experimental animal systems and in clinical settings – most of which are technical. An important technical question in the clinical setting is whether phase image parameters can be measured at sufficient resolution using clinical scanner hardware. Such research is ongoing. However, even if technical obstacles are successfully overcome, such as adequate SNR and reasonably short clinical scan times, the extent to which quantification and classification of BMB iron content adds value in clinical settings remains to be demonstrated. For example, is knowing the total iron extravasated due to several BMB in a brain region more informative and clinically relevant than simply knowing the number of BMB in the region? Such questions will eventually require clinical research experiments.

Conclusion

In conclusion, the current research project proposes a family of methods that use phase image features to quantify iron content and effective diameter in localized brain iron sources. The techniques have been tested in phantom, postmortem and living rat brain, and postmortem human tissue systems, using both modeled and actual BMB. Several novel contributions have been described in each of the four experimental systems. Notable results in the application of our method include non-invasive estimates

of BMB (upper bound) true diameter and (lower bound) iron concentration, and a tentative standard curve allowing BMB iron content estimates in postmortem AD/CAA brain based on phase image parameters. Our methods potentially allows the definition of iron load or disease burden indices from the level of a single bleed, to the whole brain (e.g. "the sum of the iron content of all lobar BMB"), as well as the classification of BMB by size unobscured by the blooming effect. A "count, classify and quantify" method can potentially be fully or semi-automated, and results can in principle be compared across field strengths and echo times. Such information potentially could enhance prognostic and diagnostic criteria in the context of cerebral vessel disease associated late onset dementias, as well as inform treatment decisions e.g. regarding the use of thrombolytic or thrombotic agents. However, technical feasibility and the tangible value of information derived from these techniques to clinical or research settings remains to be determined. Important future steps include testing and validation of the methods on clinical scanners and under clinically practical scan time constraints, research into the physical and magnetic properties of BMB iron, and investigation of robust filtering and background phase removal techniques.

REFERENCES

Ayaz M, Boikov AS, Haacke EM, Kido DK, Kirsch WM., 2010. Imaging cerebral microbleeds using susceptibility weighted imaging: one step toward detecting vascular dementia. J Magn Reson Imaging 31, 142-148.

Akter, M., Hirai, T., Hiai, Y., Kitajima, M., Komi, M., Murakami, R., Fukuoka, H., Sasao, A., Toya, R., Haacke, E.M., Takahashi, M., Hirano, T., Kai, Y., Morioka, M., Hamasaki, K., Kuratsu, J.-I., Yamashita, Y., 2007. Detection of hemorrhagic hypointense foci in the brain on susceptibility-weighted imaging clinical and phantom studies. Academic Radiology 14, 1011-1019.

Andersen, J.K., 2004. Iron dysregulation and Parkinson's disease. Journal of Alzheimer's Disease: JAD 6, S47-52.

Andrä, W., Nowak, H., 2007. Magnetism in Medicine: A Handbook. Wiley-VCH.

Association, A., 2007. Alzheimers Disease Facts and Figures 2007.

Atlas, S.W., Mark, A.S., Grossman, R.I., Gomori, J.M., 1988. Intracranial hemorrhage: gradient-echo MR imaging at 1.5 T. Comparison with spin-echo imaging and clinical applications. Radiology 168, 803-807.

Ayaz, M., Boikov, A.S., Haacke, E.M., Kido, D.K., Kirsch, W.M., Imaging cerebral microbleeds using susceptibility weighted imaging: one step toward detecting vascular dementia. Journal of Magnetic Resonance Imaging: JMRI 31, 142-148.

Bartzokis, G., Aravagiri, M., Oldendorf, W.H., Mintz, J., Marder, S.R., 1993. Field dependent transverse relaxation rate increase may be a specific measure of tissue iron stores. Magnetic Resonance in Medicine: Official Journal of the Society of Magnetic Resonance in Medicine / Society of Magnetic Resonance in Medicine 29, 459-464.

Bartzokis, G., Lu, P.H., Tishler, T.A., Fong, S.M., Oluwadara, B., Finn, J.P., Huang, D., Bordelon, Y., Mintz, J., 2007. Myelin breakdown and iron changes in Huntington's disease: pathogenesis and treatment implications. Neurochem Res 32, 1655—1664.

Bennett, D.A., Schneider, J.A., Arvanitakis, Z., Kelly, J.F., Aggarwal, N.T., Shah, R.C., Wilson, R.S., 2006. Neuropathology of older persons without cognitive impairment from two community-based studies. Neurology 66, 1837-1844.

Bishop, G.M., Robinson, S.R., 2002. The amyloid hypothesis: let sleeping dogmas lie? Neurobiology of Aging 23, 1101-1105.

Bizzi, A., Brooks, R.A., Brunetti, A., Hill, J.M., Alger, J.R., Miletich, R.S., Francavilla, T.L., Di Chiro, G., 1990. Role of iron and ferritin in MR imaging of the brain: a study in primates at different field strengths. Radiology 177, 59-65.

Bos, C., Viergever, M.A., Bakker, C.J.G., 2003. On the artifact of a subvoxel susceptibility deviation in spoiled gradient-echo imaging. Magnetic Resonance in Medicine: Official Journal of the Society of Magnetic Resonance in Medicine / Society of Magnetic Resonance in Medicine 50, 400-404.

Bullock, R., Mendelow, A.D., Teasdale, G.M., Graham, D.I., 1984. Intracranial haemorrhage induced at arterial pressure in the rat. Part 1: Description of technique, ICP changes and neuropathological findings. Neurological Research 6, 184-188.

Bush, A.I., 2003. The metallobiology of Alzheimer's disease. Trends Neurosci 26, 207—214.

Bradley WG., 1993. MR appearance of hemorrhage in the brain. Radiology 189, 15-26.

Cheng, Y.-C.N., Hsieh, C.-Y., Neelavalli, J., Liu, Q., Dawood, M.S., Haacke, E.M., 2007. A complex sum method of quantifying susceptibilities in cylindrical objects: the first step toward quantitative diagnosis of small objects in MRI. Magn Reson Imaging 25, 1171—1180.

Cordonnier, C., van der Flier, W.M., Sluimer, J.D., Leys, D., Barkhof, F., Scheltens, P., 2006. Prevalence and severity of microbleeds in a memory clinic setting. Neurology 66, 1356-1360.

Cordonnier, C., Salman, R.A.-S., Wardlaw, J., 2007a. Spontaneous brain microbleeds: systematic review, subgroup analyses and standards for study design and reporting. Brain 130, 1988—2003.

Cordonnier, C., Potter, G.M., Jackson, C.A., Doubal, F., Keir, S., Sudlow, C.L.M., Wardlaw, J.M., Al-Shahi Salman, R., 2009. improving interrater agreement about brain microbleeds: development of the Brain Observer MicroBleed Scale (BOMBS). Stroke; a Journal of Cerebral Circulation 40, 94-99.

de Rochefort, L., Liu, T., Kressler, B., Liu, J., Spincemaille, P., Lebon, V., Wu, J., Wang, Y., Quantitative susceptibility map reconstruction from MR phase data using bayesian regularization: validation and application to brain imaging. Magnetic Resonance in Medicine: Official Journal of the Society of Magnetic Resonance in Medicine / Society of Magnetic Resonance in Medicine 63, 194-206.

Dixon, W.T., Blezek, D.J., Lowery, L.A., Meyer, D.E., Kulkarni, A.M., Bales, B.C., Petko, D.L., Foo, T.K., 2009. Estimating amounts of iron oxide from gradient echo images. Magnetic Resonance in Medicine: Official Journal of the Society of Magnetic Resonance in Medicine / Society of Magnetic Resonance in Medicine 61, 1132-1136.

Duyn, J.H., Gelderen, P.v., Li, T.-Q., Zwart, J.A.d., Koretsky, A.P., Fukunaga, M., 2007. High-field MRI of brain cortical substructure based on signal phase. Proc Natl Acad Sci U S A 104, 11796—11801.

Fazekas, F., Roob, G., Kleinert, G., Kapeller, P., Schmidt, R., Hartung, H.P., 1999. Histopathologic analysis of foci of signal loss on gradient-echo T2*-weighted MR images in patients with spontaneous intracerebral hemorrhage: evidence of microangiopathy-related microbleeds. AJNR Am J Neuroradiol 20, 637—642.

Gaasch JA, Lockman PR, Geldenhuys WJ, Allen DD, Van der Schyf CJ. Brain iron toxicity: differential responses of astrocytes, neurons, and endothelial cells. Neurochemical Research 2007 32(7):1196-1208.

Gelman, N., Gorell, J.M., Barker, P.B., Savage, R.M., Spickler, E.M., Windham, J.P., Knight, R.A., 1999. MR Imaging of Human Brain at 3.0 T: Preliminary Report on Transverse Relaxation Rates and Relation to Estimated Iron Content. Radiology 210, 759-767.

Greenberg, S.M., Eng, J.A., Ning, M., Smith, E.E., Rosand, J., 2004. Hemorrhage burden predicts recurrent intracerebral hemorrhage after lobar hemorrhage. Stroke; a Journal of Cerebral Circulation 35, 1415-1420.

Greenberg, S.M., Vernooij, M.W., Cordonnier, C., Viswanathan, A., Al-Shahi Salman, R., Warach, S., Launer, L.J., Van Buchem, M.A., Breteler, M.M., 2009. Cerebral microbleeds: a guide to detection and interpretation. Lancet Neurology 8, 165-174.

Gregoire, S.M., Brown, M.M., Kallis, C., Jäger, H.R., Yousry, T.A., Werring, D.J., MRI detection of new microbleeds in patients with ischemic stroke: five-year cohort follow-up study. Stroke; a Journal of Cerebral Circulation 41, 184-186.

Gregoire, S.M., Chaudhary, U.J., Brown, M.M., Yousry, T.A., Kallis, C., Jäger, H.R., Werring, D.J., 2009. The Microbleed Anatomical Rating Scale (MARS): reliability of a tool to map brain microbleeds. Neurology 73, 1759-1766.

Haacke, E.M., Brown, R.W., Thompson, M.R., Venkatesan, R., 1999. Magnetic Resonance Imaging, Physical Principles and Sequence Design. Wiley-Liss.

Haacke, E.M., Xu, Y., Cheng, Y.-C.N., Reichenbach, J.r.R., 2004. Susceptibility weighted imaging (SWI). Magn Reson Med 52, 612—618.

Haacke, E.M., Cheng, N.Y.C., House, M.J., Liu, Q., Neelavalli, J., Ogg, R.J., Khan, A., Ayaz, M., Kirsch, W., Obenaus, A., 2005. Imaging iron stores in the brain using magnetic resonance imaging. Magn Reson Imaging 23, 1—25.

Haacke, E.M., Ayaz, M., Khan, A., Manova, E.S., Krishnamurthy, B., Gollapalli, L., Ciulla, C., Kim, I., Petersen, F., Kirsch, W., 2007a. Establishing a baseline phase behavior in magnetic resonance imaging to determine normal vs. abnormal iron content in the brain. J Magn Reson Imaging 26, 256—264.

Haacke, E.M., DelProposto, Z.S., Chaturvedi, S., Sehgal, V., Tenzer, M., Neelavalli, J., Kido, D., 2007. Imaging cerebral amyloid angiopathy with susceptibility-weighted imaging. AJNR Am J Neuroradiol 28, 316—317-316—317.

Hardy, J.A., Higgins, G.A., 1992. Alzheimer's disease: the amyloid cascade hypothesis. Science (New York, N.Y.) 256, 184-185.

Helmer, O., Emerson, C., 1934. The iron content of whole blood in normal individuals. J Biol Chem 104, 157-161.

Hirtz, D., Thurman, D.J., Gwinn-Hardy, K., Mohamed, M., Chaudhuri, A.R., Zalutsky, R., 2007. How common are the "common" neurologic disorders? Neurology 68, 326-337.

House, M.J., Pierre, T.G.S., Kowdley, K.V., Montine, T., Connor, J., Beard, J., Berger, J., Siddaiah, N., Shankland, E., Jin, L.-W., 2007. Correlation of proton transverse relaxation rates (R2) with iron concentrations in postmortem brain tissue from alzheimer's disease patients. Magn Reson Med 57, 172—180.

Igase, M., Tabara, Y., Igase, K., Nagai, T., Ochi, N., Kido, T., Nakura, J., Sadamoto, K., Kohara, K., Miki, T., 2009. Asymptomatic cerebral microbleeds seen in healthy subjects have a strong association with asymptomatic lacunar infarction. Circulation Journal: Official Journal of the Japanese Circulation Society 73, 530-533.

Ishimori, Y., Monma, M., Kohno, Y., 2009. Artifact reduction of susceptibility-weighted imaging using a short-echo phase mask. Acta Radiologica (Stockholm, Sweden: 1987) 50, 1027-1034.

Jellinger, K.A., 2006. Alzheimer 100—highlights in the history of Alzheimer research. J Neural Transm 113, 1603—1623-1603—1623.

Jellinger, K.A., Attems, J., 2006. Prevalence and impact of cerebrovascular pathology in Alzheimer's disease and parkinsonism. Acta Neurol Scand 114, 38—46-38—46.

Jellinger, K.A., Lauda, F., Attems, J., 2007. Sporadic cerebral amyloid angiopathy is not a frequent cause of spontaneous brain hemorrhage. Eur J Neurol 14, 923—928-923—928.

Jensen, J.H., Szulc, K., Hu, C., Ramani, A., Lu, H., Xuan, L., Falangola, M.F., Chandra, R., Knopp, E.A., Schenck, J., Zimmerman, E.A., Helpern, J.A., 2009. Magnetic field correlation as a measure of iron-generated magnetic field inhomogeneities in the brain. Magnetic Resonance in Medicine: Official Journal of the Society of Magnetic Resonance in Medicine / Society of Magnetic Resonance in Medicine 61, 481-485.

Jeon, S.-B., Kang, D.-W., Cho, A.H., Lee, E.-M., Choi, C.G., Kwon, S.U., Kim, J.S., 2007. Initial microbleeds at MR imaging can predict recurrent intracerebral hemorrhage. Journal of Neurology 254, 508-512.

Jeon, S.B., Kwon, S.U., Cho, A.H., Yun, S.C., Kim, J.S., Kang, D.W., 2009. Rapid appearance of new cerebral microbleeds after acute ischemic stroke. Neurology 73, 1638-1644.

Kidwell, C.S., Greenberg, S.M., 2009. Red meets white: do microbleeds link hemorrhagic and ischemic cerebrovascular disease? Neurology 73, 1614-1615.

Kim, J.K., Kucharczyk, W., Henkelman, R.M., 1993. Cavernous hemangiomas: dipolar susceptibility artifacts at MR imaging. Radiology 187, 735-741.

Kimberly W.T., Gilson A., Rost N.S., Rosand J., Viswanathan A., Smith E.E., Greenberg S.M., 2009. Silent ischemic infarcts are associated with hemorrhage burden in cerebral amyloid angiopathy. Neurology 72(14):1230-1235.

Kirsch, W., McAuley, G., Holshouser, B., Petersen, F., Ayaz, M., Vinters, H.V., Dickson, C., Haacke, E.M., Britt Iii, W., Larsen, J., Kim, I., Mueller, C., Schrag, M., Kido, D., 2009. Serial Susceptibility Weighted MRI Measures Brain Iron and Microbleeds in Dementia. Journal of Alzheimer's Disease 17, 599-609.

Knudsen, K.A., Rosand, J., Karluk, D., Greenberg, S.M., 2001. Clinical diagnosis of cerebral amyloid angiopathy: validation of the Boston criteria. Neurology 56, 537-539.

Lee, S.-H., Kim, S.-M., Kim, N., Yoon, B.-W., Roh, J.-K., 2007. Cortico-subcortical distribution of microbleeds is different between hypertension and cerebral amyloid angiopathy. Journal of the Neurological Sciences 258, 111-114.

Lee, S.-H., Ryu, W.-S., Roh, J.-K., 2009. Cerebral microbleeds are a risk factor for warfarin-related intracerebral hemorrhage. Neurology 72, 171-176.

Liu, T., Spincemaille, P., Rochefort, L.d., Kressler, B., Wang, Y., 2009. Calculation of susceptibility through multiple orientation sampling (COSMOS): A method for conditioning the inverse problem from measured magnetic field map to susceptibility source image in MRI. Magnetic Resonance in Medicine 61, 196-204.

Liu, W., Frank, J.A., 2009. Detection and quantification of magnetically labeled cells by cellular MRI. European Journal of Radiology 70, 258-264.

Manfred O, Till W, Christoph M, Hans-Jürgen F., 2004. Time Course of Cortical Hemorrhages after Closed Traumatic Brain Injury: Statistical Analysis of Posttraumatic Histomorphological Alterations. Journal of Neurotrauma 20, 87-103.

McAuley G, Schrag M, Sipos P, Sun S-W, Obenaus A, Neelavalli J, Haacke EM, Holshouser B, Madácsi R, Kirsch W. Quantification of punctate iron sources using magnetic resonance phase. Magnetic Resonance in Medicine 2010a 63(1):106-115.

McAuley G, Schrag M, Barnes S, Obenaus A, Dickson A, Holshouser B, Kirsch W. Iron quantification of microbleeds in postmortem brain. Accepted pending minor revisions in Magnetic Resonance in Medicine 2010b.

MacKay, A., Vavasour, I., Bjarnason, T., Kolind, S., Mädler, B., 2006. Insights into brain microstructure from the T2 distribution. Magn Reson Imaging 24, 515—525-515—525.

MacLellan, C.L., Silasi, G., Poon, C.C., Edmundson, C.L., Buist, R., Peeling, J., Colbourne, F., 2008. Intracerebral hemorrhage models in rat: comparing collagenase to blood infusion. Journal of cerebral blood flow and metabolism : official journal of the International Society of Cerebral Blood Flow and Metabolism 28, 516-525.

McClure, F.J., Kornberg, A., 1947. Blood Hemoglobin And Hematocrit Results On Rats Ingesting Sodium Fluoride. J Pharmacol Exp Ther 89, 77-80.

McCluskey, L., Campbell, S., Anthony, D., Allan, S.M., 2008. Inflammatory responses in the rat brain in response to different methods of intra-cerebral administration. Journal of neuroimmunology 194, 27-33.

McCrea, R.P.E., Harder, S.L., Martin, M., Buist, R., Nichol, H., 2008. A comparison of rapid-scanning X-ray fluorescence mapping and magnetic resonance imaging to localize brain iron distribution. European Journal of Radiology 68, S109-113-S109-113.

Menon, R.S., Kidwell, C.S., 2009. Neuroimaging demonstration of evolving small vessel ischemic injury in cerebral amyloid angiopathy. Stroke; a Journal of Cerebral Circulation 40, e675-677.

Mills, P.H., Wu, Y.-J.L., Ho, C., Ahrens, E.T., 2008. Sensitive and automated detection of iron-oxide-labeled cells using phase image cross-correlation analysis. Magnetic Resonance Imaging 26, 618-628.

Neelavalli, J., Cheng, Y.-C.N., Jiang, J., Haacke, E.M., 2009. Removing background phase variations in susceptibility-weighted imaging using a fast, forward-field calculation. Journal of Magnetic Resonance Imaging: JMRI 29, 937-948.

Neema, M., Arora, A., Healy, B.C., Guss, Z.D., Brass, S.D., Duan, Y., Buckle, G.J., Glanz, B.I., Stazzone, L., Khoury, S.J., Weiner, H.L., Guttmann, C.R.G., Bakshi, R., 2009. Deep gray matter involvement on brain MRI scans is associated with clinical progression in multiple sclerosis. Journal of Neuroimaging: Official Journal of the American Society of Neuroimaging 19, 3-8.

Nishimura, N., Schaffer, C.B., Friedman, B., Tsai, P.S., Lyden, P.D., Kleinfeld, D., 2006. Targeted insult to subsurface cortical blood vessels using ultrashort laser pulses: three models of stroke. Nature Methods 3, 99-108.

Ogg, R.J., Langston, J.W., Haacke, E.M., Steen, R.G., Taylor, J.S., 1999. The correlation between phase shifts in gradient-echo MR images and regional brain iron concentration. Magn Reson Imaging 17, 1141—1148.

Ordidge, R.J., Gorell, J.M., Deniau, J.C., Knight, R.A., Helpern, J.A., 1994. Assessment of relative brain iron concentrations using T2-weighted and T2*-weighted MRI at 3 Tesla. Magn Reson Med 32, 335—341.

Orken, D.N., Kenangil, G., Uysal, E., Forta, H., 2009. Cerebral microbleeds in ischemic stroke patients on warfarin treatment. Stroke; a Journal of Cerebral Circulation 40, 3638-3640.

Perez C.A., Tong Y., Guo M., 2008. Iron Chelators as Potential Therapeutic Agents for Parkinson's Disease. Curr Bioact Compd 4, 150-158.

Pfefferbaum, A., Adalsteinsson, E., Rohlfing, T., Sullivan, E.V., 2009. MRI estimates of brain iron concentration in normal aging: comparison of field-dependent (FDRI) and phase (SWI) methods. NeuroImage 47, 493-500.

Pintaske, J., Müller-Bierl, B., Schick, F., 2006a. Effect of spatial distribution of magnetic dipoles on Lamor frequency distribution and MR Signal decay—a numerical approach under static dephasing conditions. MAGMA 19, 46—53.

Pintaske, J., Müller-Bierl, B., Schick, F., 2006b. Geometry and extension of signal voids in MR images induced by aggregations of magnetically labelled cells. Phys Med Biol 51, 4707—4718.

Querfurth, H.W., LaFerla, F.M., Alzheimer's disease. The New England Journal of Medicine 362, 329-344.

Reichenbach, J.R., Venkatesan, R., Schillinger, D.J., Kido, D.K., Haacke, E.M., 1997a. Small vessels in the human brain: MR venography with deoxyhemoglobin as an intrinsic contrast agent. Radiology 204, 272-277.

Reichenbach, J.R., Venkatesan, R., Yablonskiy, D.A., Thompson, M.R., Lai, S., Haacke, E.M., 1997b. Theory and application of static field inhomogeneity effects in gradient-echo imaging. J Magn Reson Imaging 7, 266—279.

Robson, P., Hall, L., 2005. Identifying particles in industrial systems using MRI susceptibility artefacts. AIChE Journal 51, 1633-1640.

Rochefort, L.d., Brown, R., Prince, M.R., Wang, Y., 2008. Quantitative MR susceptibility mapping using piece-wise constant regularized inversion of the magnetic field. Magnetic Resonance in Medicine 60, 1003-1009.

Rosand, J., Muzikansky, A., Kumar, A., Wisco, J.J., Smith, E.E., Betensky, R.A., Greenberg, S.M., 2005. Spatial clustering of hemorrhages in probable cerebral amyloid angiopathy. Annals of Neurology 58, 459-462.

Rosenberg, G.A., Mun-Bryce, S., Wesley, M., Kornfeld, M., 1990. Collagenase-induced intracerebral hemorrhage in rats. Stroke; a Journal of Cerebral Circulation 21, 801-807.

Schäfer, A., Wharton, S., Gowland, P., Bowtell, R., 2009. Using magnetic field simulation to study susceptibility-related phase contrast in gradient echo MRI. NeuroImage 48, 126-137.

Schenck, J.F., Zimmerman, E.A., 2004. High-field magnetic resonance imaging of brain iron: birth of a biomarker? NMR in Biomedicine 17, 433-445.

Schneider, J.A., 2007. Brain microbleeds and cognitive function. Stroke; a Journal of Cerebral Circulation 38, 1730-1731.

Schrag M, McAuley G, Pomakian J, Jiffry A, Tung S, Mueller C, Vinters H, Haacke E, Holshouser B, Kido D, Kirsch W. Correlation of hypointensities in susceptibility-weighted images to tissue histology in dementia patients with cerebral amyloid angiopathy: a postmortem MRI study. Acta Neuropathologica 2010 119(3):291-302.

Shmueli, K., de Zwart, J.A., van Gelderen, P., Li, T.-Q., Dodd, S.J., Duyn, J.H., 2009. Magnetic susceptibility mapping of brain tissue in vivo using MRI phase data. Magnetic Resonance in Medicine: Official Journal of the Society of Magnetic Resonance in Medicine / Society of Magnetic Resonance in Medicine 62, 1510-1522.

Sipos, P., Berkesi, O., Tombácz, E., Pierre, T.G.S., Webb, J., 2003. Formation of spherical iron(III) oxyhydroxide nanoparticles sterically stabilized by chitosan in aqueous solutions. J Inorg Biochem 95, 55—63.

Smirnov, P., Gazeau, F., Beloeil, J.C., Doan, B.T., Wilhelm, C., Gillet, B., 2006. Single-cell detection by gradient echo 9.4 T MRI: a parametric study. Contrast Media & Molecular Imaging 1, 165-174.

Smith M.A., Harris P.L., Sayre L.M., Perry G., 1997. Iron accumulation in Alzheimer disease is a source of redox-generated free radicals. Proc Natl Acad Sci USA. 94, 9866-8.

Smith MA, Zhu X, Tabaton M., Liu G., McKeel D.W., Cohen M.L., Wang X., Siedlak S.L., Hayashi T., Nakamura M., Nunomura A., Perry G., 2010. Increased Iron and Free Radical Generation in Preclinical Alzheimer Disease and Mild Cognitive Impairment. J Alzheimers Dis. 19, 363-372.

Smith, E., Greenberg, S., 2009. Beta-amyloid, blood vessels, and brain function. Stroke, 2009 Jul;40(7):2601-6.

Soo, Y.O.Y., Yang, S.R., Lam, W.W.M., Wong, A., Fan, Y.H., Leung, H.H.W., Chan, A.Y.Y., Leung, C., Leung, T.W.H., Wong, L.K.S., 2008. Risk vs benefit of anti-thrombotic therapy in ischaemic stroke patients with cerebral microbleeds. Journal of Neurology 255, 1679-1686.

Staals, J., van Oostenbrugge, R.J., Knottnerus, I.L.H., Rouhl, R.P.W., Henskens, L.H.G., Lodder, J., 2009. Brain microbleeds relate to higher ambulatory blood pressure levels in first-ever lacunar stroke patients. Stroke; a Journal of Cerebral Circulation 40, 3264-3268.

Sten JC-E, 2006. Ellipsoidal harmonics and their application in electrostatics. Journal of Electrostatics 64, 647-654.

Sveinbjornsdottir, S., Sigurdsson, S., Aspelund, T., Kjartansson, O., Eiriksdottir, G., Valtysdottir, B., Lopez, O.L., van Buchem, M.A., Jonsson, P.V., Gudnason, V., Launer, L.J., 2008. Cerebral microbleeds in the population based AGES-Reykjavik study: prevalence and location. Journal of Neurology, Neurosurgery, and Psychiatry 79, 1002-1006.

Szumowski, J., Bas, E., Gaarder, K., Schwarz, E., Erdogmus, D., Hayflick, S., Measurement of brain iron distribution in Hallevorden-Spatz syndrome. Journal of Magnetic Resonance Imaging: JMRI 31, 482-489.

Tanaka A., Ueno Y., Nakayama Y., Takano K., Takebayashi S., 1999. Small chronic hemorrhages and ischemic lesions in association with spontaneous intracerebral hematomas. Stroke. 30, 1637-1642.

Tatsumi, S., Shinohara, M., Yamamoto, T., 2008. Direct comparison of histology of microbleeds with postmortem MR images: a case report. Cerebrovascular Diseases (Basel, Switzerland) 26, 142-146.

Tong, K.A., Ashwal, S., Holshouser, B.A., Shutter, L.A., Herigault, G., Haacke, E.M., Kido, D.K., 2003. Hemorrhagic shearing lesions in children and adolescents with posttraumatic diffuse axonal injury: improved detection and initial results. Radiology 227, 332—339.

Tong, K.A., Ashwal, S., Holshouser, B.A., Nickerson, J.P., Wall, C.J., Shutter, L.A., Osterdock, R.J., Haacke, E.M., Kido, D., 2004. Diffuse axonal injury in children: clinical correlation with hemorrhagic lesions. Ann Neurol 56, 36—50.

Titova E, Ostrowski RP, Sowers LC, Zhang JH, Tang J., 2007. Effects of apocynin and ethanol on intracerebral haemorrhage-induced brain injury in rats. Clin Exp Pharmacol Physiol Sep 34(9):845-50.

Varma, G., Pedersen, S.F., Taupitz, M., Botnar, R.M., Dahnke, H., Keevil, S.F., Schaeffter, T., 2009. Utilizing different methods for visualizing susceptibility from a single multi-gradient echo dataset. Magma (New York, N.Y.).

Vernooij, M.W., van der Lugt, A., Ikram, M.A., Wielopolski, P.A., Niessen, W.J., Hofman, A., Krestin, G.P., Breteler, M.M.B., 2008. Prevalence and risk factors of cerebral microbleeds: the Rotterdam Scan Study. Neurology 70, 1208-1214.

Vernooij, M.W., Haag, M.D.M., van der Lugt, A., Hofman, A., Krestin, G.P., Stricker, B.H., Breteler, M.M.B., 2009. Use of Antithrombotic Drugs and the Presence of Cerebral Microbleeds: The Rotterdam Scan Study. Arch Neurol 66, 714-720.

Vinters, H.V., Gilbert, J.J., 1983. Cerebral amyloid angiopathy: incidence and complications in the aging brain. II. The distribution of amyloid vascular changes. Stroke; a Journal of Cerebral Circulation 14, 924-928.

Viswanathan, A., Chabriat, H., 2006. Cerebral microhemorrhage. Stroke; a Journal of Cerebral Circulation 37, 550-555.

Vymazal, J., Klempír, J., Jech, R., Zidovská, J., Syka, M., Ruzicka, E., Roth, J., 2007. MR relaxometry in Huntington's disease: Correlation between imaging, genetic and clinical parameters. Journal of the Neurological Sciences 263, 20-25.

Wang, Y., Yu, Y., Li, D., Bae, K.T., Brown, J.J., Lin, W., Haacke, E.M., 2000. Artery and vein separation using susceptibility-dependent phase in contrast-enhanced MRA. J Magn Reson Imaging 12, 661—670.

Wang, Z.J., Li, S., Haselgrove, J.C., 1999. Magnetic resonance imaging measurement of volume magnetic susceptibility using a boundary condition. Journal of Magnetic Resonance (San Diego, Calif.: 1997) 140, 477-481.

Wang, Z.J., Lian, L., Chen, Q., Zhao, H., Asakura, T., Cohen, A.R., 2005. 1/T2 and Magnetic Susceptibility Measurements in a Gerbil Cardiac Iron Overload Model. Radiology 234, 749-755.

Werring, D.J., Frazer, D.W., Coward, L.J., Losseff, N.A., Watt, H., Cipolotti, L., Brown, M.M., Jäger, H.R., 2004. Cognitive dysfunction in patients with cerebral microbleeds on T2*-weighted gradient-echo MRI. Brain: A Journal of Neurology 127, 2265-2275.

Werring, D.J., 2007. Cerebral microbleeds: clinical and pathophysiological significance. Journal of Neuroimaging: Official Journal of the American Society of Neuroimaging 17, 193-203.

Winkler, D.T., Bondolfi, L., Herzig, M.C., Jann, L., Calhoun, M.E., Wiederhold, K.H., Tolnay, M., Staufenbiel, M., Jucker, M., 2001. Spontaneous hemorrhagic stroke in a mouse model of cerebral amyloid angiopathy. The Journal of neuroscience : the official journal of the Society for Neuroscience 21, 1619-1627.

Yablonskiy, D.A., Haacke, E.M., 1994. Theory of NMR signal behavior in magnetically inhomogeneous tissues: the static dephasing regime. Magn Reson Med 32, 749—763-749—763.

Yakushiji, Y., Nishiyama, M., Yakushiji, S., Hirotsu, T., Uchino, A., Nakajima, J., Eriguchi, M., Nanri, Y., Hara, M., Horikawa, E., Kuroda, Y., 2008. Brain microbleeds and global cognitive function in adults without neurological disorder. Stroke; a Journal of Cerebral Circulation 39, 3323-3328.

Yamada, N., Imakita, S., Sakuma, T., Takamiya, M., 1996. Intracranial calcification on gradient-echo phase image: depiction of diamagnetic susceptibility. Radiology 198, 171-178.

Zhang-Nunes, S.X., Maat-Schieman, M.L.C., Duinen, S.G.v., Roos, R.A.C., Frosch, M.P., Greenberg, S.M., 2006. The cerebral beta-amyloid angiopathies: hereditary and sporadic. Brain Pathol 16, 30—39-30—39.

Zhang, W., Sun, S.-G., Jiang, Y.-H., Qiao, X., Sun, X., Wu, Y., 2009. Determination of brain iron content in patients with Parkinson's disease using magnetic susceptibility imaging. Neuroscience Bulletin 25, 353-360.

Zhu, W.-z., Zhong, W.-d., Wang, W., Zhan, C.-j., Wang, C.-y., Qi, J.-p., Wang, J.-z., Lei, T., 2009. Quantitative MR Phase-corrected Imaging to Investigate Increased Brain Iron Deposition of Patients with Alzheimer Disease1. Radiology 253, 497-504.

Zlokovic, B.V., 2005. Neurovascular mechanisms of Alzheimer's neurodegeneration. Trends in Neurosciences 28, 202-208.